Surface Tension Modulated Instabilities in Thin Liquid Films

A thesis submitted
in partial fulfilment of the requirements
for the degree of

Doctor of Philosophy

by

Rajkumar Sarma

Department of Mechanical Engineering
Indian Institute of Technology Guwahati
Guwahati - 781039
November 2020

भारतीय प्रौद्योगिकी संस्थान गुवाहाटी
Indian Institute of Technology Guwahati
Guwahati - 781 039

CERTIFICATE

This is certified that the work contained in the thesis entitled "**Surface Tension Modulated Instabilities in Thin Liquid Films**" by **Rajkumar Sarma**, has been carried out under my supervision and that this work has not been submitted elsewhere for a degree.

Date:

Dr. Pranab Kumar Mondal
Assistant Professor
Department of Mechanical Engineering
Indian Institute of Technology Guwahati

Dedicated to my parents

ACKNOWLEDGEMENTS

The challenging journey of doctoral study can only be accomplished through a lot of support, encouragement and inspiration from the well-wishers. I take this opportunity to express my gratitude to all those personalities who have directly or indirectly contributed to reaching the destination. At the outset, I thank the Almighty for blessing me with the strength and patience required to pursue this journey. I consider myself fortunate enough to join the PhD programme just after my graduation, in an institution of international repute. I am deeply indebted to this institute for providing me with such an excellent environment for the inception of my research career.

I am immensely grateful to my supervisor Dr. Pranab K. Mondal for the continuous guidance and support he has provided throughout the course of this work. His valuable ideas, advice and motivations helped me in shaping up my research skills. Besides my supervisor, I would also like to thank my doctoral committee members, Prof. Niranjan Sahoo, Dr. Bhaskar kumar and Dr. R. Anandalakshmi for their suggestions and insightful comments that helped me in improving my understanding towards my research area.

My sincere gratitude goes to the mechanical engineering department for providing me with the necessary facilities to perform my research. In this regard, special mention is needed about the “Microfluidics and microscale transport processes lab” which used to be like my home during the PhD tenure.

I would deeply thank my fellow lab mates Abhijit Gogoi, Harshad Gaikwad, Sudip Shyam, Aritra Mukherjee, Prateechee Padma Behera, Anurag Mishra, Nitin Dhasmana, Abhay Shukla, L. Harsha, Arup Mohapatra and Sanjaya Meher for maintaining a healthy work environment. The wonderful discussions we had will cherish me forever. Special thanks also go to Dr. S. R. Gorthi for the personal and professional discussions on various topics. These acknowledgements would not complete without mentioning my friends Subrata, Tarun and Sukanta. Their presence has made my stay in the campus memorable.

Finally, I thank my parents and elder brother whose blessings have always kept me going. This journey would not have been possible to complete without their support and encouragement.

Rajkumar Sarma

Abstract

A gradient of surface tension caused by the inhomogeneities in temperature (thermocapillarity) or concentration (solutocapillarity) on the free surface of a pure liquid or liquid mixtures has the ability to induce motion in its bulk phase. Typically known as the Marangoni instability, this phenomenon is frequently encountered in the small-scale systems (e.g. a thin liquid film, droplet, vapour bubble, or a liquid bridge) where the surface effects dominate over the volumetric ones. The present thesis aims at understanding this instability phenomenon for thin films of Newtonian and viscoelastic liquids under the framework of linear stability analysis. The analysis pertaining to the Marangoni instability in Newtonian liquid is undertaken in the first part of the thesis. In the second part, the instability phenomenon is investigated for viscoelastic fluids. The dynamics of both the long-wave and short-wave perturbations are studied for the most classical system configuration of a thin liquid film confined between its free surface and a poorly conducting rigid substrate. Besides exploring the basic instability modes for both the Newtonian and viscoelastic fluids, the parameter regimes are also identified for which these instability modes become dominant in the system. A brief summary of the problems considered in this thesis is given below.

For most liquids, although the surface tension is a linear function of temperature, there exists a particular class of liquids where surface tension varies non-monotonically with temperature. The variation in such circumstances is often approximated by a quadratic relationship. The first problem aims at understanding the instability phenomenon for such a liquid film. The analysis reveals that on heating this fluid layer from below, both the monotonic and oscillatory instability can appear depending on the deformability of the free surface and the heat transfer rate from this surface.

The second part of this thesis explores the instability characteristics of viscoelastic films. The viscoelastic fluids are a class of non-Newtonian fluids that exhibits both viscous and elastic behavior. Phenomena like elastic recoiling, stress relaxation can take place during the deformation of such fluids, for which the current state of stress becomes a function of past history. An attempt is made in the second problem to analyze the purely thermocapillary driven instability in such a liquid film. This study reveals that, for heating the system from below, apart from the conventional short-wave disturbances, the long-

wave disturbances can also emerge in the fluid layer. However, the preferred mode of instability is decided by the deformability of the free surface, heat transfer rate from this surface and the elasticity level of the liquid.

It is important to note that viscoelastic fluids like polymer solutions, biofluids etc. are essentially a binary mixture of polymeric solute and Newtonian solvent. Both thermocapillary and solutocapillary effects can be at play in such fluids due to the cross diffusive effects. In the third problem, attention is therefore focused on developing a complete thermosolutal model to study the instability phenomenon in viscoelastic liquids. The analysis reveals that under the combined influences of thermo-solutocapillarity and the elasticity of the liquid, apart from the monotonic disturbances, two different oscillatory instabilities can emerge in the film. While one oscillatory mode results from the interaction between the thermocapillary and solutocapillary effect, the elastic behavior of the fluid is found to be responsible for the other one.

Finally, the possibility of this instability phenomenon for heating the polymeric liquid film from the free surface is analyzed. It is found that all the basic instability modes that appear in the fluid layer for heating from below can emerge for heating from the free surface as well. However, their characteristics and the parameter regime for which they get dominant in the system change appreciably from the case of heating the fluid layer from below.

The findings from this thesis improve our understanding of the Marangoni instability in both the Newtonian and viscoelastic fluids. Several novel instability modes are detected in the present work that forms a strong basis for the future course investigation in such fluids. Furthermore, each instability mode is supported by realistic experimental conditions, which in turn, will assist in observing the convective patterns in a physical set-up.

Contents

ACKNOWLEDGEMENTS ..... **vii**

List of Figures ..... **xvii**

List of Tables ..... **xxv**

Nomenclature ..... **xxvii**

1 Introduction **1**

1.1 Phenomenology of Surface Tension Driven Instabilities 2

1.2 Methods of Analysis 4

1.3 Overview of Literature 5

1.3.1 Marangoni instability in Newtonian liquids 5

1.3.2 Marangoni instability in Viscoelastic liquids 8

1.4 Objectives of the Research 9

1.5 Layout of the Thesis 10

2 Effect of Nonmonotonic Variation of Surface Tension with Temperature on the Marangoni Instability in a Newtonian Liquid Film **13**

2.1 Introduction 13

2.2 Mathematical Formulation of the Problem 14

2.2.1 Governing equations 15

2.2.2 Base state 16

2.2.3 Dimensionless equations 17

2.2.4 Dimensionless base state 17

2.3 Long-wave Stability Theory 18

2.3.1 Lubrication approximation 18

2.3.2 Amplitude equations 20

2.3.3 Linear stability analysis 21

2.4 Short-wave Stability Theory 26

2.4.1 Linear stability analysis 26

2.5 Summary 33

3 Long-wave Marangoni Instability in a Viscoelastic Liquid Film **35**

3.1 Introduction 35

3.2 Mathematical Formulation of the Problem 36

3.2.1 Governing equations 37

3.2.2 Non-dimensionalization 39
3.2.3 Base state 41
3.3 Linear Stability Analysis 41
3.3.1 Monotonic mode 44
3.3.2 Oscillatory mode 44
3.4 Long-wave Instability 46
3.4.1 Lubrication approximation 46
3.4.2 Amplitude equations 48
3.4.3 Dispersion relation 49
3.5 Short-wave Instability 53
3.6 Experimental Feasibility 59
3.7 Summary 60
4 Thermosolutal Marangoni Instability in a Viscoelastic Liquid Film 63
4.1 Introduction 63
4.2 Mathematical Model 64
4.2.1 Governing equations 66
4.2.2 Non-dimensionalization 67
4.3 Base State and Linear Stability Analysis 69
4.4 The Linear Stability Picture 73
4.4.1. Effect of elasticity and the free surface deformability 73
4.4.2. The role of thermocapillary and solutocapillary effects 78
4.4.3. The role of thermal and solutal diffusivities 81
4.4.4. The role of heat transfer rate at the free surface 83
4.5 An Approximate Model 84
4.5.1 Monotonic mode 87
4.5.2 Oscillatory mode 89
4.6 Phase Diagrams 91
4.7 Summary 94
5 Marangoni Instability in a Viscoelastic Liquid Film Heated from the Free Surface 97
5.1 Introduction 97
5.2 Mathematical Formulation 98
5.2.1 Governing equations and boundary conditions 98
5.2.2 Non-dimensionalization 101
5.3 Base State and Linear Stability Analysis 103
5.4 Results 105

5.4.1 Monotonic mode 106
5.4.2 Oscillatory mode 108
5.5 Phase Diagrams 114
5.6 Potential Experimental Settings 116
5.7 Summary 118
6 Conclusions and Scope for Further Work 121
6.1 Conclusions 121
6.1.1 Effect of non-monotonic variation of surface tension on the Marangoni instability in a Newtonian liquid film 122
6.1.2 Marangoni instability in viscoelastic liquids 123
6.2 Scope for Further Work 126
References 129
Appendix A 139
Appendix B 141
Appendix C 143
List of Publications 145

List of Figures

1.1 Schematic of the physical system. A fluid layer initially at rest produces motion under the sole influence of surface tension gradient at the free surface. ……2

1.2 Top view of the Bénard cells in a shallow liquid layer. ……3

1.3 Wine tears in a glass of wine. ……5

2.1 Schematic of the physical system under consideration with the imposed boundary conditions. The deformable interface is located at $z = h(x, y, t)$. A constant heat flux at the solid substrate yields a temperature gradient $-\vartheta$ at the $z = 0$ plane. …….. 14

2.2 Neutral stability curves for the long-wave monotonic (solid lines) and oscillatory (dashed lines) modes at $Pr = 1$, $Ga = 10$, $\Sigma = 10^3$. Panel (*a*) corresponds to $Bi = 0.05$, panel (*b*) corresponds to $Bi = 0.5$. The inset in panel (*a*) shows the zoomed-in view of the stability curve for the monotonic mode of instability. ……23

2.3 Neutral stability curves for the long-wave monotonic (solid and dash-dotted lines) and oscillatory modes (dotted and dashed lines) for different values of *Ga* at $Pr = 1$, $\Sigma = 10^3$ and $Bi = 0.1$. Lines marked by 1 and 2 correspond to $Ga = 1$ and $Ga = 10$ respectively. The inset shows the zoomed-in view of the stability curve at higher wave number. ……25

2.4 Neutral stability curves for the long-wave monotonic (solid and dash-dotted lines) and oscillatory modes (dotted and dashed lines) for different Σ at $Pr = 1$, $Ga = 10$ and $Bi = 0.1$. Lines marked by 1 and 2 correspond to $\Sigma = 10^3$ and $\Sigma = 10^4$ respectively. ……26

2.5 Variation of the (*a*) critical Marangoni number, and (*b*) the critical wave number with *Bi* at $Pr = 1$, $Ga = 10$, $\Sigma = 10^3$. The inset in panel (*a*) shows the zoomed-in view at small Biot number. ……29

2.6 Phase diagrams depicting the regimes of dominant instability mode in (*a*) *Bi* - Σ plane at $Pr = 1$, $Ga = 10$ (*b*) *Bi* – *Ga* plane at $Pr = 1$, $\Sigma = 10^3$. The oscillatory mode becomes dominant for parameter values that lie within the shaded region. Shaded region 1 corresponds to the results of the long-wave theory, while regime 2 refers to the results of the short-wave analysis. For parameter values that lie towards the left of the shaded domains 1 and 2, the long-wave monotonic mode gets dominant in the system, whereas for parameter values that lie on its right, the short-wave monotonic mode becomes dominant. ……30

2.7 (*a*) Variation of the critical Marangoni number and (*b*) the critical wave number with Galileo number at $Bi = 0.05$, $Pr = 1$, $\Sigma = 10^3$. ……..…….……30

2.8 Variation of (*a*) the critical Marangoni number and (*b*) the critical wave number with Σ at $Bi = 0.1$, $Pr = 1$, $Ga = 10$. ……..31

2.9 Neutral stability curves for an aqueous 1-butanol fluid layer of thickness 0.05 mm, $Bi = 0.025$, $Ga = 6$ and $\Sigma = 5\times10^3$. The solid line represents the monotonic mode, and dashed one corresponds to the oscillatory mode of instability. ……..32

3.1 Sketch defining the physical system under study. A thin viscoelastic liquid film, resting on a solid substrate of very low thermal conductivity and having a deformable free surface is subjected to heating from below. The dashed-dotted line corresponds to the undisturbed interface in the equilibrium state. ……36

3.2 Neutral stability curves for a Newtonian liquid layer confined between a horizontal substrate of low thermal conductivity and a non-deformable free surface. The results obtained from the present study (shown by solid lines) are compared with the results of Pearson [11] (shown by marker 'o') for two different *Bi* (0 and 5 respectively). To mimic the characteristics of a non-deformable free surface, here we consider $Ga = 10^2$ and $\Sigma = 10^6$. ……44

3.3 Variation of the monotonic (*Mon.*: dashed-dotted line) and oscillatory (*Osc.*: solid and dotted lines) instability threshold for a viscoelastic liquid layer for $Ga = 0.1$, $\Sigma = 10^3$, $Bi = 0.1$, $Pr = 10$ and various values of Deborah number, *De*. The domain of stability is situated below the lines. Note the variation in the critical instability modes for $De = 0.1$ and 1. For the long-wave oscillatory mode $Ma_c\big|_{\mathrm{De}=0.1} = 39.15$, $Ma_c\big|_{\mathrm{De}=1} = 39.6$; while for the short-wave oscillatory mode $Ma_c\big|_{\mathrm{De}=0.1} = 42$, $Ma_c\big|_{\mathrm{De}=1} = 2$. ……45

3.4 (*a*) Neutral stability curves for the long-wave monotonic (*Mon.*: solid lines) and oscillatory (*Osc.*: dashed lines) modes of instability at $(Ga, \Sigma) = (0.1, 10^3)$ and $De = 0.1$. The solid and dashed lines represent the result of the asymptotic analysis, while the dotted lines represent the numerical result. (*b*) Variation of the stability threshold for the long-wave oscillatory mode with *De* at $Bi = 0.1$ and $(Ga, \Sigma) = (0.1, 10^3)$ (inset shows the zoomed-in view of the neutral curves for *De* = 0 and 0.1 respectively). (*c*) Variation of the growth rate of neutral perturbations for *De* = 0 (dashed and dotted lines) and *De* = 1 (dashed-dot and solid lines) at $(Ga, \Sigma) = (0.1, 10^3)$. In panels (*a*) and (*c*) lines marked by 1 and 2 correspond to $Bi = 0.05$ and 0.1 respectively. ……..……..51

3.5 Variation of the stability threshold with Biot number for $(Ga, \Sigma) = (0.1, 10^3)$ and $Pr = 10$. Panels (*a*) and (*b*) display the neutral stability curves for monotonic (*Mon.*: dashed and dashed-dotted lines) and oscillatory (*Osc.*: solid and dotted lines) modes for $De = 0.1$ and 1 respectively. Panel (*c*) displays the variation of the frequency of neutral perturbations for $Bi = 0.05$ (solid lines) and $Bi = 0.1$ (dotted

and dashed-dotted lines). Lines marked by 1 and 2 in panel (c) correspond to $De = 1$ and 0.1 respectively. Domains of stability lie below the lines. ……..……..54

3.6 Variation of the critical Marangoni number (*a*) and (*c*), and critical wave number (*b*) with *Bi* at $(Ga, \Sigma) = (0.1, 10^3)$ and $Pr = 10$. Panel (*a*)-(*b*) and (*c*) represent the variations for $De = 0.1$ and 1 respectively. The solid line corresponds to the monotonic (*Mon.*) mode, dashed one to the long-wave oscillatory (LO) mode and the dashed-dotted line represents the variation for the short-wave oscillatory (SO) mode. For each long-wave instability mode, the results of the asymptotic analysis (represented by dotted lines) are juxtaposed with the corresponding numerical results in each panel. ……..……55

3.7 Variation of the stability margin for the monotonic (*Mon.*: dashed-dotted and dashed lines) and oscillatory (*Osc.*: dotted and solid lines) instability modes for different values of *De*, *Ga* and Σ at $Bi = 0.05$, $Pr = 10$. Panel (*a*) corresponds to *De* = 0.1, panel (*b*) corresponds to $De = 1$, panel (*c*) corresponds to $Ga = 0.1$. In panels (*a*) and (*b*), the lines marked by 1 and 2 correspond to $(Ga, \Sigma) = (0.1, 10^3)$ and $(Ga, \Sigma) = (10^2, 10^5)$ respectively. For panel (*c*), the dashed and dotted lines correspond to $\Sigma = 10^3$, while the dashed-dotted and solid lines correspond to $\Sigma = 10$. Here, the lines marked by 1 and 2 correspond to $De = 0.1$ and $De = 1$ respectively. …...……..…...…..56

3.8 Variation of the critical Marangoni number (*a*) and (*d*), the corresponding critical wave number (*b*) and (*e*), and the frequency of critical perturbations (*c*) and (*f*) with Deborah number at $Bi = 0.05$ and $Pr = 10$. Panels (*a*)-(*b*)-(*c*) and (*d*)-(*e*)-(*f*) represent the variations for $(Ga, \Sigma) = (0.1, 10^3)$ and $(Ga, \Sigma) = (10^2, 10^5)$ respectively. In each panel, the solid line corresponds to the monotonic (*Mon.*) mode, dashed one to the long-wave oscillatory (LO) mode and the dashed-dotted line represent the short-wave oscillatory (SO) mode respectively. ……58

3.9 The domains of monotonic and oscillatory instability modes. Panel (*a*) corresponds to $(Ga, \Sigma) = (0.1, 10^3)$; panel (*b*) corresponds to $(Ga, \Sigma) = (10^2, 10^5)$, $Pr = 10$. 59

4.1 Schematic illustration of the physical system under consideration. A thin viscoelastic film (composed of a polymeric solute in a Newtonian solvent) confined between its deformable free surface $z = h(x,t)$ and a horizontal substrate in the gravitational field **g**, is subjected to a vertical temperature gradient. This applied temperature gradient induces a concentration gradient in the film via the Soret effect. The surface tension gradient arising from inhomogeneities in temperature and concentration at the air-liquid interface induces Marangoni convection in the liquid layer. The dashed line corresponds to the undeformed interface at the quiescent base state. ……..…64

4.2 Comparison of the present numerical result with the results of Shklyaev *et al*. [110] (shown by marker "**o**") via the neutral stability curve at $Pr = 2$, $\chi = -0.2$, $Le = 10^{-3}$. Curves marked by 1 and 2 corresponds to $Bi = 0$ and $Bi = 0.1$ respectively. To

represent the characteristics of a Newtonian binary liquid with a non-deformable free surface, we consider $De = 0$ and $(Ga, \Sigma) \to \infty$. 72

4.3 Neutral stability curves for the monotonic instability mode. The solid line represents the stability threshold for a deformable free surface $(Ga, \Sigma) = (0.1, 10^3)$, whereas the dotted line demonstrates the stability margin for a non-deformable free surface $(Ga, \Sigma) \to \infty$. The dot (o) mark on each neutral curve represents the critical point of the curve. Inset depicts the effect of free surface deformability on the stability threshold in the long-wave regime. Other parameters: $Bi = 0.01$, $\chi = 0.5$, $Le = 10^{-3}$, $Pr = 10$. 73

4.4 (a,c) Neutral stability curves , and (b,d) the corresponding oscillation frequency ω for oscillatory-I instability mode for $\chi < 0 (= -0.5)$ and $\chi > 0 (= 0.5)$ respectively. For (a,b): lines marked by 1 and 2 corresponds to $De = 0$ and $De = 1$ respectively; for (c,d): lines marked by 1 and 2 corresponds to $De = 0.1$ and $De = 1$ respectively. In each panel, the solid and the dash-dotted lines depict the results for a deformable free surface $(Ga, \Sigma) = (0.1, 10^3)$; the adjacent dotted lines represents the results for a non-deformable free surface $(Ga, \Sigma) \to \infty$. The dot (o) mark on each neutral curve denotes the critical point (or the global minimum) of the curve. Other parameters: $Bi = 0.1$, $Le = 10^{-2}$, $Pr = 10$. 75

4.5 Variation of the (a) critical Marangoni number Ma_c, and the corresponding critical (b) wavenumber k_c, and (c) oscillation frequency ω_c with Deborah number De for the oscillatory-I instability mode for $\chi < 0$. The solid line depicts the variation for a deformable free surface $(Ga, \Sigma) = (0.1, 10^3)$; and the dotted one for a non-deformable surface $(Ga, \Sigma) \to \infty$. The arrow marks in panels (b,c) illustrate a switchover in the instability behavior with the increasing elasticity of the liquid. Other parameters: $Bi = 0.1$, $Le = 10^{-2}$, $\chi = -0.5$. 77

4.6 Neutral stability curves for the monotonic and oscillatory–I modes in the (a,c) positive, and (b) negative Soret number χ domains. The long-wave branch for the oscillatory-I mode emerges only when $\chi < 0$. The dot (o) mark on each neutral curve represents the critical point of the curve. Other parameters: $Bi = 0.01$, $De = 1$, $Le = 10^{-3}$, $(Ga, \Sigma) = (0.1, 10^3)$. 79

4.7 Variation of the (a) critical Marangoni number Ma_c, and the corresponding (b) critical wavenumber k_c with χ. In each panel, the solid, dash-dotted, and dashed lines represent the variations for a deformable free surface $(Ga, \Sigma) = (0.1, 10^3)$. The dotted lines adjacent to each instability mode represent the variations for a non-deformable free surface $(Ga, \Sigma) \to \infty$. Other parameters: $Bi = 0.01, Le = 10^{-3}$. 80

4.8 Effect of Lewis number Le on the monotonic and oscillatory instability threshold for (a,c) $\chi < 0 (= -0.5)$, and (b) $\chi > 0 (= 0.5)$. The dot (o) mark on each neutral curve represents the critical point of the curve. Panel (c) shows that for a deformable

free surface at higher value of *Le*, a different type of long-wave oscillatory instability (oscillatory-II) can emerge in the fluid layer. Other parameters: $Bi = 0.01$, $De = 1$, and $(Ga, \Sigma) = (0.1, 10^3)$. ……..……..81

4.9 Comparison of the oscillation frequency of neutral perturbations for oscillatory–II mode with oscillatory–I mode (shown in the inset). $\chi = 0.5$, $Bi = 0.01$, $De = 1$, $Le = 0.1$, $(Ga, \Sigma) = (0.1, 10^3)$. ……..……82

4.10 Variation of the critical Marangoni number with for the oscillatory–II mode at $Bi = 0.01$, $Le = 0.1$, $(Ga, \Sigma) = (0.1, 10^3)$. Note that no oscillatory–II instability emerges for $\chi \le 0$. ……..…83

4.11 Effect of Biot number *Bi* on the monotonic and oscillatory instability threshold for (*a*) $\chi < 0 (= -0.5)$, and (*b*,*c*,*d*) $\chi > 0 (= 0.5)$ for a film with deformable free surface $(Ga, \Sigma) = (0.1, 10^3)$. Other parameters: $De = 1$, $Le = 10^{-2}$. ……..……84

4.12 Comparison of results obtained from the approximate model (solid and dash-dotted lines) with the numerical results (dotted lines) for the monotonic instability mode via the neutral stability curve (*a*) deformable surface $(Ga, \Sigma) = (0.1, 10^3)$, (*b*) non-deformable surface $(Ga, \Sigma) \to \infty$. The dot (**o**) mark on each neutral curve represents the critical point of the curve. Other parameters: , $Bi = 0.01$ $Le = 0.1$. ……..……88

4.13 Comparison between results of the numerical computation (dotted lines) and the approximate model (solid and dash-dotted lines) for the oscillatory-I mode via neutral stability curve: (*a*) long-wave branch at $Le = 0.1$, $\chi = -0.5$ (*b*) short-wave branch at $Le = 10^{-3}$, $\chi = 0.5$. Other parameters: $Bi = 0.01, (Ga, \Sigma) = (0.1, 10^3)$. ……...90

4.14 Comparison of results obtained from the approximate model (solid and dash-dotted lines) with the numerical results (dotted lines) for the oscillatory-II mode via the neutral stability curve at $Bi = 0.01$, $De = 1$, $Le = 0.1$, $(Ga, \Sigma) = (0.1, 10^3)$. ..……91

4.15 Phase diagrams for (χ, De) at different *Le* enclosing the regimes of dominant instability mode: (*a*,*b*) deformable free surface $(Ga, \Sigma) = (0.1, 10^3)$, and (*c*,*d*) non-deformable free surface $(Ga, \Sigma) \to \infty$ at $Bi = 0.01$, $Pr = 10$. In panels (*a*-*d*), regime-1: monotonic instability, regime-2: long-wave oscillatory–I instability, reg ime-3: short-wave oscillatory–I instability, regime-4: oscillatory –II instability. At the points marked ***p*** and ***q*** in panels (*a*,*b*), the three adjacent instability modes can coexist. ……92

5.1 Schematic of the physical system under investigation. Marangoni instability is induced in a thin viscoelastic polymer film confined between its deformable free surface (located at $z = h(x,t)$), and a flat substrate (at the $z = 0$ plane) when subjected to heating from above. The polymeric solution is a binary mixture of

Newtonian solvent with polymeric solute. The incorporation of Soret effect signifies the combined thermo-solutal instability in the system. ……..98

5.2 Neutral stability curves for the monotonic instability mode at $\chi = -0.5$, $Bi = 0.1$, $Le = 10^{-2}$, $Pr = 10$. The solid line and the symbols ◊ depict the stability boundary for a system with a deformable free surface $(Ga, \Sigma) = (0.1, 10^3)$; the dotted line and the symbols ☆ show the stability threshold for a system possessing non-deformable free surface $(Ga, \Sigma) \to \infty$. The dot (o) mark on each neutral curve represents the critical point of the curve. ……. 106

5.3 Effect of on the stability threshold for the monotonic instability mode at , $Bi = 10^{-2}$ $Le = 10^{-2}$, $Pr = 10$. The solid and the dotted line demonstrates the stability boundary for a liquid layer with a deformable $(Ga, \Sigma) = (0.1, 10^3)$ and non-deformable $(Ga, \Sigma) \to \infty$ free surface, respectively. ……..…… 107

5.4 (*a*) Neutral stability curves and the corresponding (*b*) oscillation frequency ω for the oscillatory-I mode at $\chi = -0.5$, $Bi = 0.1$, $De = 1$, $Le = 10^{-2}$, $Pr = 10$. The dashed and solid line depicts the stability boundary for a deformable free surface, while their adjacent dotted line demonstrates the stability threshold for a non-deformable free surface (for the same *De*). The dot (o) mark on each neutral curve represents the critical point (the global minimum) of the curve. ……..……..108

5.5 Effect of fluid elasticity on the instability threshold for the oscillatory-I mode. The dashed and dotted line depicts the variation for a liquid layer with deformable $(Ga, \Sigma) = (0.1, 10^3)$ and non-deformable free surface $(Ga, \Sigma) \to \infty$ respectively. Ma_c refers to the global minimum of the neutral curve. Other parameters: $Bi = 0.1$, $Le = 10^{-2}$, $Pr = 10$. ……..……109

5.6 Variation of the (*a*) critical Marangoni number Ma_c and the (*b*) critical wave number k_c with χ for the oscillatory-I instability mode at $Bi = 10^{-2}$, $De = 1$, $Pr = 10$, $Le = 10^{-3}$. In panels (*a*,*b*), the dash-dotted line represents the results for a deformable free surface $(Ga, \Sigma) = (0.1, 10^3)$, while the dotted line depicts the results for a non-deformable free surface $(Ga, \Sigma) \to \infty$. ……110

5.7 (*a*) Neutral stability curves and the corresponding (*b*) oscillation frequency ω for the oscillatory-II mode at $\chi = -0.5$, $Bi = 0.1$, $De = 1$, $Le = 10^{-2}$, $Pr = 10$, $(Ga, \Sigma) = (0.1, 10^3)$. The dot (o) mark on each neutral curve in panel (*a*) represents the critical point of the curve. At higher values of *k*, the neutral curves for the oscillatory-II mode merge with the neutral curve for the monotonic mode. ……..……112

5.8 Variation of the critical Marangoni number with χ for the oscillatory-II mode (dotted line) at $Bi=10^{-2}$, $De=1$, $Le=10^{-2}$, $(Ga,\Sigma)=(0.1,10^3)$ and $Pr=10$. $Ma_c-\chi$ variations for the monotonic (solid line) and oscillatory-I (dashed-dotted line) modes are plotted here for reference. Inset shows the zoomed-in view for $\chi\to 0$. 113

5.9 Effect of free surface deformability on the (*a*) instability threshold and the (*b*) oscillation frequency of the neutral perturbations for the oscillatory-II mode at $Bi=0.1$, $De=1$, $\chi=-0.1$, $Le=10^{-2}$, $Pr=10$. 114

5.10 Phase diagrams summarising the boundaries between different dominant instability mode in the (De,χ) plane for different values of *Le*: (*a*,*b*) deformable free surface $(Ga,\Sigma)=(0.1,10^3)$, and (*c*,*d*) non-deformable free surface $(Ga,\Sigma)\to\infty$. Other parameters: $Bi=10^{-2}$, $Pr=10$. In panels (*a*-*d*), regime-1: monotonic instability, regime-2: long-wave oscillatory–I instability, regime-3: short-wave oscillatory–I instability, regime-4: oscillatory –II instability. 115

List of Tables

5.1 Physical properties of water-ethanol and polystyrene-benzene solution. ……..…116

Nomenclature

English symbols

c	Concentration
D	Mass diffusivity
g	Acceleration due to gravity
h	Instantaneous film thickness
H	Unperturbed film thickness
i	Imaginary unit
$\mathbf{k}$	Unit vector in the z-direction
k	Disturbance wavenumber
$\mathbf{n}$	Unit vector in the normal direct
p	Pressure
q	Heat transfer coefficient
$\mathbb{R}$	Real number
$\mathcal{S}$	Soret coefficient
t	Time
T	Temperature
u	Velocity component in the x-direction
$\mathbf{V}$	Velocity vector
w	Velocity component in the z-direction
x, y, z	Cartesian coordinates

Greek symbols

α	Thermal diffusivity
σ	Surface tension
κ	Thermal conductivity
λ	Disturbance growth rate
ϑ	Temperature gradient

ψ	Stream function
ω	Oscillation frequency
μ	Dynamics viscosity
ρ	Density
ν	Kinematic viscosity
Σ	Inverse capillary number
χ	Soret number
$\boldsymbol{\tau}$	Deviatoric stress tensor
ε	Ratio between liquid layer thickness and length
$\hat{\lambda}$	Relaxation time

Abbreviations

Bi	Biot number
De	Deborah number
Ga	Galileo number
Le	Inverse Lewis number
Ma	Marangoni number
Pr	Prandtl number
mon.	Monotonic
osc.	Oscillatory

Acronyms

LM	Long-wave monotonic
LO	Long-wave oscillatory
SM	Short-wave monotonic
SO	Short-wave oscillatory
BVP	Boundary value problem
EVP	Eigen value problem

Subscripts

c	Critical value

i	Imaginary
o	Initial/base value
r	Real
xx	Component acting on the *x*-plane in the *x*-direction
xz	Component acting on the *x*-plane in the *z*-direction
zx	Component acting on the *z*-plane in the x-direction
zz	Component acting on the *z*-plane in the *z*-direction

Superscripts

o	Base state

Chapter 1

Introduction

Since the development of analytical ability in humans, the curiosity about numerous natural phenomena has always preoccupied their minds. One such event is the hydrodynamic instability. Starting from the patterning of clouds in the sky to the large-scale convection in Earth's mantle, this is an inescapable physical phenomenon. From the pioneering works of Bénard, Helmholtz, Kelvin and Reynolds, these widespread events have attracted considerable attention over the years to explore their rich and interesting dynamics. Instability occurs whenever an externally imposed constraint disturbs the equilibrium between the stabilizing and destabilizing effects in a fluidic system. Notably, the destabilization may be caused by a large number of agents, *viz*. inertia, buoyancy, surface tension, centrifugation, Coriolis force etc. [1,2]. For small amplitude of the imposed constraints, the fluctuations are initially dampened by the dissipative effects like viscosity and thermal diffusivity inherent to the system. However, beyond a certain critical value of these constraints, the fluctuations get amplified by these destabilizing effects. This makes the system unstable, and the phenomenon of hydrodynamic instability comes into the picture.

The recent advent of microfluidics has motivated a lot of researchers to explore the instability picture in miniaturized systems, *viz.* thin-films, droplets etc. Thin-film flows are also central to the areas of geophysics, biophysics and engineering [3–9]. In such settings, the films are usually composed of pure liquids (e.g. water, oil), multicomponent mixture, and sometimes with rheologically complex fluids (e.g. polymeric solution, biofluids etc.). It is important to note that thin liquid films can become unstable even in the absence of inertia, *i.e.*, at an initial quiescent state. Surface forces can alone destabilize thin films, leading to the formation of regular or chaotic structures, periodic waves or more complex patterns. One such instability phenomenon is the surface tension driven Marangoni instability.

1.1 Phenomenology of Surface Tension Driven Instabilities

It is well known that a free liquid surface possesses localized properties, the most prominent one of which is the surface tension σ. Usually, its magnitude depends on the scalar fields like the temperature field, electrical field as well as on the concentration of solute/surfactant (for a multicomponent liquid mixture). A local variation in any of the above-mentioned quantities on the free surface can therefore generate a gradient of surface tension. It is evident that a liquid with higher surface tension pulls the surrounding liquid more strongly than that with relatively lower surface tension. Hence, the presence of surface tension gradient naturally causes the liquid to move away from the regions of low surface tension, as shown in Fig. 1. Now, since all real fluids possess viscosity, a bulk-fluid motion is eventually established in the entire fluid layer. Therefore, a liquid layer initially at a quiescent state finally produces an unstable movement under the sole influence of surface tension.

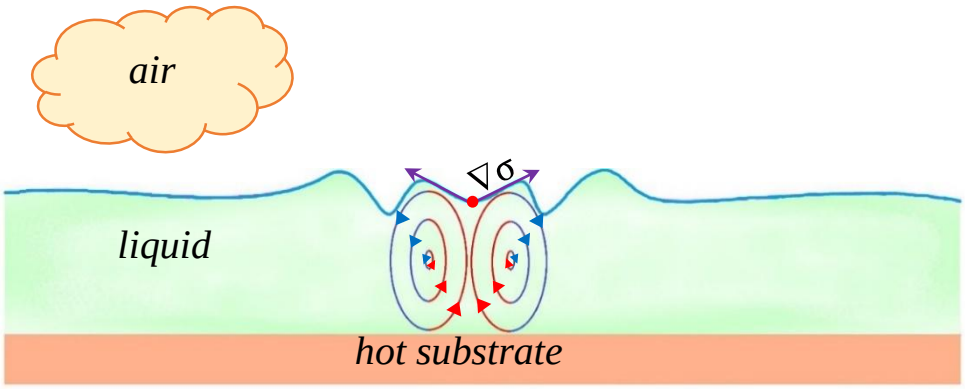

Figure 1.1: Schematic of the physical system. A fluid layer initially at rest produces motion under the sole influence of surface tension gradient at the free surface.

The emergence of instability in the system is indicated by the formation of beautiful steady patterns (famously observed by Bénard [10], shown in Fig. 2), or oscillatory (wave) structures. It is important to note that Marangoni instability occurs only in sufficiently thin films, for thickness $H \lesssim O(1)$ cm or less [11]. For $H > O(1)$ cm, the buoyancy-driven mechanism becomes dominant, inducing the Rayleigh-Bénard instability in the system. Situations where the buoyancy and surface tension both acts together, the resulting instability is called the Rayleigh-Bénard-Marangoni instability.

Figure 1.2: Top view of the Bénard cells in a shallow liquid layer [12].

Unlike the case of pure liquids, the Marangoni instability in a multicomponent liquid mixture can develop under the simultaneous influences of thermocapillary and solutocapillary effect. While the thermocapillary effects in such liquids usually originate from an externally applied temperature gradient, the solutocapillary effects herein may be caused by an externally imposed concentration gradients or due to the cross-diffusive effects [13,14]. One such important cross-diffusive effect in liquid mixtures is the Soret effect. Under an imposed temperature gradient, it leads to the spontaneous development of the solute concentration gradient in the bulk fluid. Therefore, Marangoni instability in a binary mixture can originate under the following two physical situations: (*i*) the temperature and the concentration gradients are caused by the independent sources (often called as double-diffusive convection) [15–17]; and (*ii*) the temperature gradient is externally imposed, while the concentration gradient is generated spontaneously by the Soret effect [18–22].

It is noteworthy that due to the involvement of surface effects, the Marangoni instability can develop even in the microgravity environment [23–26]. The onset of this instability phenomenon dramatically increases the interfacial heat and mass transfer rate through the mixing triggered by convection. This, in turn, influences the processes like liquid/liquid extraction, liquid/gas absorption or desorption, distillation etc. [27–34]. The emergence of Marangoni instability also dominates the dynamics in the phase change processes (e.g. evaporation in a heat exchanger) [35,36], the material processing operations (e.g. crystal growth process, welding) [37–39], the rupture of thin films, the

drying of paint films and the coating process [40,41] etc. An understanding of this instability mechanism therefore helps in optimizing these processes.

1.2 Methods of Analysis

The investigation of a hydrodynamic instability problem involves the prediction of conditions corresponding to its onset in the system, understanding the nature of instability, the physical mechanism behind their inception, the study of pattern dynamics and finally its transition to turbulence. Theoretical, numerical and experimental – all three approaches can be followed to analyze a particular instability phenomenon. However, the development of theoretical concepts is essential to describe and interpret the results of experimentation and numerical simulations.

Under the theoretical approach, the linear stability analysis has proven to be a powerful tool to analyze the hydrodynamic instability, at least for bifurcation around a quiescent base state. Comparison with experiments suggests that this technique can accurately predict the conditions (*i.e.*, the critical temperature difference across the film, the size of the convective structure and their oscillation frequency) at the onset of instability in the system for both the long-wave and short-wave modes of Marangoni instability. The linear stability analysis involves linearization of the nonlinear governing partial differential equations around a conductive base state. However, it should be noted that the results of the linear theory remain accurate only for small perturbations around the base state [1]. This emphasizes the need for numerical simulations and experimental investigations to analyze the system dynamics in the strongly nonlinear regime.

The present dissertation aims at analyzing the instability phenomenon for two rheologically distinct fluids under the framework of linear stability analysis. The stability analysis carried out in this thesis work involves detecting only the temporal instabilities. We are not concerned here whether the disturbances grow or decay in the spatial directions. Instead, we are interested in finding whether such disturbances grow or decay in time. Furthermore, we have analyzed here only the two-dimensional perturbations considering the Squire's theorem [1]. In the first part, the Marangoni instability in a Newtonian liquid film that demonstrates non-monotonic variation of surface tension with temperature is investigated. The various instability modes and the conditions leading to

their emergence in the film is explored herein. In the second part of the thesis, the instability characteristics of a viscoelastic liquid film are analyzed. A thorough investigation is carried out from both the pure and binary fluid perspective. It is shown that in the presence of cross-diffusive effects, such a liquid film exhibits an altogether different stability picture that cannot be described by the pure fluid model. The motivation behind addressing these problems is discussed in the forthcoming section.

1.3 Overview of Literature

1.3.1 Marangoni instability in Newtonian liquids

The ability of surface tension to induce motion in liquids was first conceived by the Italian physicist Carlo Marangoni in 1871. While analyzing the phenomenon "tears of wine", he found that the interfacial tension gradient resulting from composition gradient (caused by the evaporation of alcohol from a water-alcohol mixture) is the mechanism behind the formation of wine tears [42]. In his honor, the surface tension gradient driven flow in liquids is called today the Marangoni flow.

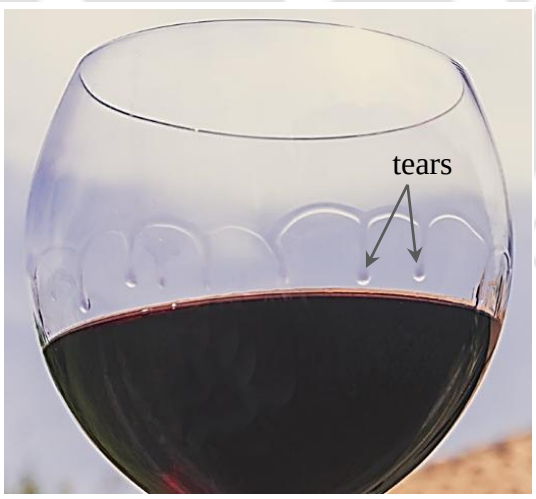

Figure 1.3: Wine tears in a glass of wine [43].

A few years later in 1900, the noted French physicist Henri Bénard [10] while conducting experiments in shallow liquid layers (nearly 0.5-1 mm deep) observed an interesting event. On heating the quiescent liquid film from below, beautiful hexagonal convective patterns appear on the free liquid surface above a particular temperature

gradient across the film. Till the 1950s, these convective patterns were misunderstood to be caused by buoyancy. Block, through a series of experiments in 1956 [44], and Pearson, in 1958 [11], theoretically established that, rather than buoyancy, the variation of surface tension with temperature is the reason behind the formation of these patterns. Performing small disturbance analysis, Pearson showed that there exists a dimensionless number (now called as the Marangoni number, and defined as the ratio between thermocapillary and diffusive time scales) that must attain a minimum critical value for the onset of convection in the film. For the case of a homogeneous liquid layer with non-deformable free surface and heated uniformly from below, he found that the critical Marangoni number is about 80. Pearson also reported that, for fluid layers of thickness up to 1 cm, the surface tension force is more dominant than buoyancy in producing such unstable motion. For liquids whose surface tension reduces with increasing temperature, the liquid layer becomes unstable only for heating from below; whereas for liquids whose surface tension increases with temperature, the heating must be from above.

Since these pioneering works, numerous theoretical, experimental and numerical investigations have been carried out over the years to elucidate the major features of this instability phenomenon [45–49]. The most classical system considered in these analyses comprises of a flat liquid film confined between its free surface and a rigid substrate. Such a system is analytically tractable, and thus provides a better insight into the stability picture. Interestingly, for this surface tension driven instability process, the nature of convective patterns depends on the characteristics of the bounding surface. Notably, the bounding substrate for the liquid layer can be of two different types: an ideally thermally conducting substrate (in which a fixed liquid temperature prevails at the film-substrate interface), and, a substrate having very low thermal conductivity (often called as "substrate insulated for temperature perturbations" wherein the normal component of heat flux remains fixed at the film-substrate interface). Similarly, the free surface bounding the system from above can also present two different characteristics *viz*., deformable and non-deformable. The deformability (non-deformability) of a free surface indicates that the gravity and surface tension forces are weak (strong) enough to keep the same surface practically deformable (flat) as and when any motion is induced in the system.

In his investigation, Pearson [11] considered both types of the bounding substrate.

For a liquid layer with non-deformable free surface he found that, in case of a perfectly conducting substrate, the stationary (or monotonic) disturbances emerge in the short-wave form ($k_c \approx O(1)$). In contrast, for an insulating substrate, the disturbances arise in the long-wave form ($k_c \to 0$). Later on, Scriven and Sternling [50] theoretically demonstrated that for the conducting case, long-wave monotonic disturbances appear only in a liquid layer with a deformable free surface. This was verified experimentally by Vanhook *et al*. [51]. They found that depending on the relative thickness and thermal conductivities of the liquid and gas layers, these disturbances either take the form of a localized depression (dry spot) or localized elevation (high spot). The onset of such disturbances can even lead to the rupture of the film.

The appearance of oscillatory instability in a Newtonian liquid film was first detected by Takashima [52,53]. In a liquid layer bounded between its deformable free surface and a perfectly conducting substrate, such disturbances appear only for heating from the free surface. On the other hand, in case of an insulating substrate, such disturbances can appear even for heating from the substrate [54–56]. These critical perturbations are materialized at $k_c \approx O\sqrt{Bi}$.

It is important to note that in the above-cited analyses, the surface tension of the fluid layer was considered to vary linearly with temperature. However, there exist a particular class of liquids that demonstrates a non-monotonic variation of σ with temperature, e.g. the ionic liquids, nematic liquid crystals, aqueous solutions of long-chain alcohol etc. σ exhibits here a well-defined minimum [57,58] or maximum [59] at specific temperatures, and usually modelled as quadratic functions of temperature. Notably, a liquid presenting a surface tension minimum is labelled as “self-rewetting” fluid by Abe [60]. When used as a coolant in the heat transfer devices (e.g. heat pipe), it has the ability to spontaneously re-wet the local dry patches or hot spots since the surface tension increases with temperature. For such a liquid film, Oron and Rosenau [61] showed that an arbitrary small initial perturbation saturated to a stable, steady-state with a perfectly continuous interface (*i.e.* thermocapillary stress prevents film rupture). Thus, such fluid enhances the performance of these devices. However, an investigation on the Marangoni instability phenomenon for liquids exhibiting a maximum of surface tension has not been carried out yet.

1.3.2 Marangoni instability in Viscoelastic liquids

Despite a remarkable advancement towards understanding the Marangoni convection in Newtonian fluids, relatively little attention has been devoted to the viscoelastic liquids. Such fluids, e.g. polymeric solutions, biofluids, paints, lubricants, etc. demonstrate complex rheological behavior. Due to the involvement of both the viscous and elastic character, these fluids exhibit time-dependent strain [62]. Phenomena like elastic recoiling, stress relaxation can take place during the deformation of viscoelastic fluids, for which the current state of stress becomes a function of the past history. Over the years, a wide variety of constitutive models have been developed to describe the rheology of viscoelastic fluids, to name a few are the Maxwell model [63], the Jeffreys' model [64], the Oldroyd model [65], and the Phan-Thien-Tanner model [66]. In these constitutive relationships, the elastic nature of the fluid is accounted by a parameter called the relaxation time, a higher magnitude of which signifies the pronounced elastic behavior of the liquid. It is worth to add here that the viscoelastic fluids are widely used now-a-days as the working media in numerous engineering applications, encompassing the microfluidic systems. A few typical examples include the chemical and food industries, geophysics, bioengineering, and so on.

Marangoni convection is often encountered in viscoelastic fluids during the phenomenon like drying of thin polymeric films, paint films etc. [41,67–69]. The convective patters developed in such liquid films have promising properties for the nanotechnological applications, e.g. organic photovoltaics and photodiodes [70]. The very first attempt to explore this instability phenomenon in viscoelastic fluids was made by Getachew and Rosenblat [71]. For a Maxwellian viscoelastic film confined between its non-deformable free surface and an ideally thermally conducting substrate, they detected both the monotonic and oscillatory instabilities in the fluid layer. Extending this analysis, Lebon *et al*. [72] analyzed the coupled Bénard-Marangoni instability in a viscoelastic Jefferys' fluid layer. Parmentier *et al*. [73] carried out a nonlinear stability analysis to identify the pattern of convective cells at the onset of instability in the fluid layer. The effect of free surface deformability on the onset of Bénard-Marangoni instability in a viscoelastic film was studied by Ramkisson *et al*. [74]. It should be noted that, in all the investigations mentioned above, the fluid layer was considered to be contained in an ideally thermally conducting substrate. The disturbances emerge in the

short-wave form in such a system, as no long-wave instability modes are detected in these investigations. Furthermore, in the above-cited works, the instability problem was analyzed for heating the system from below, thus leaving the case of heating from above completely unexplored.

Another critical aspect that needs to be highlighted here is that viscoelastic fluids like polymer solutions, biofluids (e.g. DNA solution) are essentially a binary mixture of polymeric solute and Newtonian solvent [62,75]. This binary aspect of the liquid is completely ignored in the above-cited investigations. The Soret effect can yield a stratification of the solutes in such liquids [76]. Usually, while the solutes migrate towards a colder region (owing to their large masses), nevertheless, sometimes depending on the solvent quality and the temperature of the mixture, they can also move into the warmer region [77–82]. Such migration of solutes can lead to the development of solutocapillary stress on the free surface of a viscoelastic film. This aspect necessitates the consideration of a complete thermosolutal model to investigate the Marangoni instability problem in a viscoelastic liquid.

The thermosolutal Marangoni instability problem is analyzed by [83,84] in the context of evaporation in a polymeric film. In these works, the concentration gradient is considered to be solely established by the difference in evaporation rate between the constituents, neglecting the Soret effect. These analyses provide a deep insight into the problem regarding the onset of convection in the film and the evolution of disturbances in the nonlinear regimes. However, the role of liquid elasticity on the film dynamics is not clear from these works, since the polymeric solution is treated as a Newtonian liquid. Furthermore, it also needs to be emphasized that separate thermal and solutal models considered in such works are incapable of depicting the instability modes emerging from the interaction between them. An investigation into the instability phenomenon considering this binary aspect of the fluid where both the thermal and solutal effects can come into the picture together has remained untouched in the literature.

1.4 Objectives of the Research

From the above discussions it is apparent that although numerous studies related to Marangoni instability have already been reported in the literature, several important

aspects of this instability phenomenon are yet to be analyzed for both the Newtonian and viscoelastic fluids. A few such previously unaddressed questions are attempted to be understood through this dissertation. The investigations performed here are based on the following objectives.

- ***To study the Marangoni instability in a Newtonian liquid film whose surface tension varies non-monotonically with temperature.***

  This analysis reveals that both monotonic and oscillatory disturbances can emerge in such a liquid film. It is found that these disturbances can appear either in the long-wave or short-wave form depending on the values of the model parameters.

- ***To explore the possibility of long-wave Marangoni instability in a viscoelastic liquid film.***

  This investigation shows that, in a viscoelastic film confined between its deformable free surface and a rigid insulating substrate, a long-wave mode of oscillatory Marangoni instability appears apart from the conventional short-wave mode. The characteristics of this mode are investigated here in details performing the long-wave asymptotic analysis.

- ***To analyze the Marangoni instability in a viscoelastic liquid film considering the binary aspect of the fluid.***

  A complete thermosolutal model is developed here to study the Marangoni convection in a polymeric film. Due to the thermodiffusion, both thermocapillary and solutocapillary effects are possible in a polymeric liquid film with an imposed temperature. This analysis shows that under such circumstances, the film dynamics is governed by the combined influences of thermo-solutocapillarity and the elasticity of the liquid.

- ***To explore the possibility of Marangoni instability in a viscoelastic liquid film subjected to heating from the free surface.***

  This investigation reveals that Marangoni instability in a viscoelastic film can develop even for heating from the free surface. It will be demonstrated that the elasticity of the fluid plays here a vital role in the onset of instability, as no such instability appears in a pure Newtonian liquid film for this particular direction of heating.

1.5 Layout of the Thesis

The present chapter provides a glimpse of surface tension driven instabilities in thin liquid films. A detailed literature survey and the objectives of the current thesis are also

discussed in this chapter. The remaining part of this thesis is organized as follows: Chapter 2 covers the study on Marangoni instability in a liquid film where surface tension varies non-monotonically with temperature. This problem is tackled here in the framework of linear stability technique, taking into account the deformability of the free surface. Chapters 3–5 covers the study on Marangoni instability in a viscoelastic liquid film. In Chapter 3, the instability problem is studied considering only thermocapillarity as the destabilizing mechanism. A complete thermosolutal model for the fluid is then developed in Chapter 4. The possibility of Marangoni instability in the film for heating from the free surface is analyzed in Chapter 5. Finally, in Chapter 6, the present research contributions are summarized, and the scope for further exploration are outlined.

Chapter 2

Effect of Nonmonotonic Variation of Surface Tension with Temperature on the Marangoni Instability in a Newtonian Liquid Film

In this chapter, the Marangoni instability problem is investigated for a thin liquid film, resting initially on a heated substrate of low thermal conductivity and separated from the ambient gas phase by a deformable free surface. Considering the surface tension to be a quadratic function of temperature, we analytically derive here the expressions for the neutral stability curves under the framework of linear stability analysis for both the long-wave and short-wave perturbations. A set of evolution equations is derived by employing the lubrication approximation that governs the non-linear dynamics of the long-wave perturbations.

2.1 Introduction

The surface tension is a property of liquids that can vary with temperature, concentration, electro-chemical potential etc. For a pure liquid, the surface tension is a sole function of temperature; whereas in binary mixtures, it can vary with both the temperature and concentration of the fluid [12,20]. Several experimental investigations suggest that for most of the liquids, surface tension follows a linear relationship with temperature. With the increase in temperature, the surface tension of such liquids decreases monotonically. The literature is rich in analyzing the Marangoni convection for such kind of fluids [85–95]. Nevertheless, there exist a certain class of liquids (e.g. aqueous solution of long-chain alcohols, ionic liquids, etc.) wherein surface tension varies non-monotonically with temperature [59,96,97]. These liquids exhibit a maximum of surface tension with

The contents of this chapter have been published as Sarma, R. and Mondal, P. K. (2018) "Marangoni Instability in a Thin Film Heated from Below: Effect of Non-Monotonic Dependence of Surface Tension on Temperature", Phys. Rev. E, vol. 97, pp. 043105.

temperature. Here, we investigate the Marangoni instability characteristics of such a liquid film.

This chapter is organized into five sections. The problem is mathematically formulated in Section 2.2. In Section 2.3, we analyze the problem for the long-wave perturbations. A set of non-linear evolution equations are derived in this section using the lubrication approximation. The problem is then analyzed for short-wave perturbations in Section 2.4. Finally, the summary is drawn in Section 2.5.

2.2 Mathematical Formulation of the Problem

The problem is schematically illustrated in Fig. 2.1. We begin by considering a thin film of an incompressible liquid in the gravitational field $\mathbf{g}$. The liquid layer lies atop a solid substrate of low thermal conductivity and is bounded above by a deformable free surface. Due to uniform heating from below, a constant vertical temperature gradient $-\vartheta$ prevails

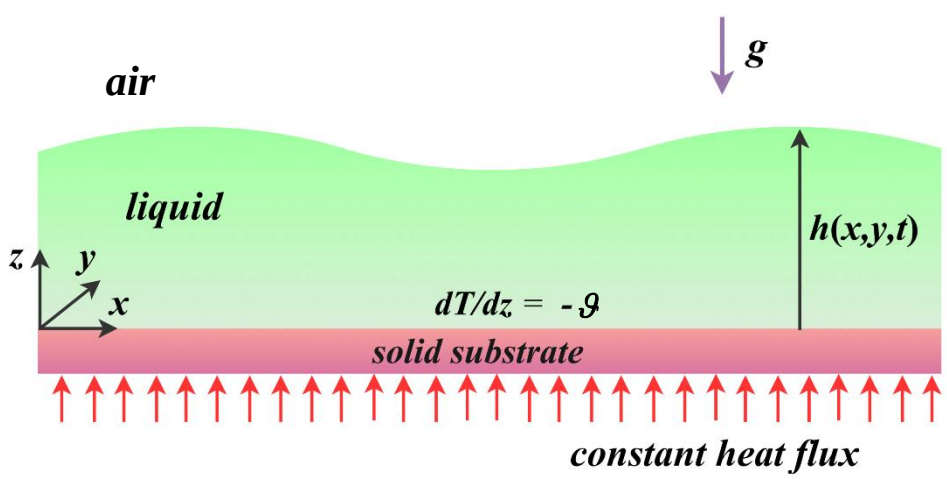

Figure 2.1: Schematic of the physical system under consideration with the imposed boundary conditions. The deformable interface is located at $z = h(x, y, t)$. Constant heat flux at the solid substrate yields the temperature gradient $-\vartheta$ at the $z = 0$ plane.

at the fluid-solid interface (*i.e.*, at the $z = 0$ plane). The liquid layer remains at rest up to a particular critical value of ϑ, above which the Marangoni convection starts appearing in it due to the variation of surface tension (σ) with temperature (T). We assume the unperturbed film thickness H to be sufficiently small so that the effect of buoyancy can

be safely neglected as compared to the Marangoni effect. Furthermore, except surface tension, all other thermophysical properties are assumed to remain invariant with temperature in this analysis.

2.2.1 Governing equations

For this surface tension driven convection process, the governing transport equations and their associated boundary conditions can be represented in dimensional form by the following set of equations

$$\nabla \bullet \boldsymbol{v} = 0 \tag{2.1a}$$

$$\boldsymbol{v}_t + (\boldsymbol{v} \bullet \nabla)\boldsymbol{v} = -\rho^{-1}\nabla p + \nu \nabla^2 \boldsymbol{v} - g\,\mathbf{k} \tag{2.1b}$$

$$T_t + \boldsymbol{v} \bullet \nabla T = \alpha\, \nabla^2 T \tag{2.1c}$$

In Eqs. 2.1(*a*-*c*), the subscript denotes the partial derivative with respect to the corresponding variable, $\boldsymbol{v}(\boldsymbol{u}, w)$ is the velocity field ($\boldsymbol{u}$ is the two-dimensional projection of velocity vector onto the $x-y$ plane and w is the z component of velocity), p is the pressure field and T is the temperature field. The terms ρ, ν, α denote, respectively, the fluid density, kinematic viscosity and thermal diffusivity, while g represents the gravitational field. Moreover, $\mathbf{k}$ is the unit vector in the z direction, $\nabla \equiv (\partial_x, \partial_y, \partial_z)$ and t represents time.

The boundary conditions at the fluid-solid interface (*i.e.*, at $z = 0$ plane) are, respectively, the no-slip condition for velocity and specified heat flux.

$$z = 0: \qquad \boldsymbol{v} = 0, \;\; T_z = -\vartheta \tag{2.2a}$$

At the free surface (*i.e.*, at $z = h(x, y, t)$ plane), the boundary conditions comprise of, respectively, the kinematic boundary condition, heat transfer governed by Newton's law of cooling and the stress balance equation (both normal and tangential stress)

$$z = h(x, y, t): \qquad h_t + \boldsymbol{u} \bullet \nabla h = w \tag{2.2b}$$

$$q(T - T_\infty) = -\kappa(\mathbf{n} \bullet \nabla T) \tag{2.2c}$$

$$\left[u_x\left(1-h_x{}^2\right)+v_y\left(1-h_y{}^2\right)+\left(u_z+w_x\right)h_x-\left(u_y+v_x\right)h_xh_y+\left(w_y+v_z\right)h_y\right]$$
$$=\frac{p\left(1+h_x{}^2+h_y{}^2\right)^{3/2}+\sigma\left[h_{xx}\left(1+h_y{}^2\right)-2h_xh_yh_{xy}+h_{yy}\left(1+h_x{}^2\right)\right]}{-2\mu\sqrt{1+h_x{}^2+h_y{}^2}} \qquad (2.2d)$$

$$2\left(w_z-u_x\right)h_x-\left(v_z+w_y\right)h_xh_y-\left(u_y+v_x\right)h_y+\left(u_z+w_x\right)\left(1-h_x{}^2\right)$$
$$=\left(\sqrt{1+h_x{}^2+h_y{}^2}\,/\,\mu\right)\frac{d\sigma}{dx} \qquad (2.2e)$$

$$2\left(w_z-v_y\right)h_y-\left(u_z+w_x\right)h_xh_y-\left(u_y+v_x\right)h_x+\left(v_z+w_y\right)\left(1-h_y{}^2\right)$$
$$=\left(\sqrt{1+h_x{}^2+h_y{}^2}\,/\,\mu\right)\frac{d\sigma}{dy} \qquad (2.2f)$$

In Eqs. 2.2(*a-f*), q denotes the rate of convective heat transfer from the liquid to the ambient gas-phase held at a fixed temperature T_∞, κ is the thermal conductivity of the liquid, μ is dynamic viscosity, and $\mathbf{n}=\left(\mathbf{k}-\nabla h\right)\Big/\sqrt{1+\left(\nabla h\right)^2}$ is the outward unit vector at the gas-liquid interface in the normal direction.

In this study, since our aim is to investigate the effect of non-linear variation of surface tension (with temperature) on the onset of Marangoni instability in the system, therefore, we consider the relationship [59]:

$$\sigma = \sigma_o-\sigma_T\left(T-T_\infty\right)^2/2 \qquad (2.3)$$

In Eq. 2.3, σ_o is the surface tension at temperature T_∞.

2.2.2 Base state

At equilibrium, the system under present consideration corresponds to a no-flow condition, indicating a laterally uniform base state. This conductive state of the system is represented by

$$h_o=H\,,\ \mathbf{v}_o=0\,,\ p_o=\rho g\left(H-z\right),\ T_o=\vartheta\left(H-z\right)+\frac{\kappa\vartheta}{q}+T_\infty \qquad (2.4)$$

Before proceeding to investigate the stability of this base state, let us first non-dimensionalize the governing equations and the associated boundary conditions.

2.2.3 Dimensionless equations

In order to non-dimensionalize the boundary value problem formulated by Eqs. 2.1 – 2.2, we define the following set of dimensionless variables

$$(\bar{x},\bar{y},\bar{z})=\frac{(x,y,z)}{H},\ \bar{t}=\frac{t}{H^2/\alpha},\ (\bar{u},\bar{v},\bar{w})=\frac{(u,v,w)}{\alpha/H},\ \ \bar{p}=\frac{p}{\rho\nu\alpha/H^2},\ \ \bar{T}=\frac{T-T_\infty}{\vartheta H}$$

Dropping the overbar sign from all the non-dimensional variables for the convenience of presentation, the governing equations in dimensionless form become

$$\nabla\bullet\boldsymbol{v}=0 \tag{2.5a}$$

$$Pr^{-1}\left(\boldsymbol{v}_t+\boldsymbol{v}\bullet\nabla\boldsymbol{v}\right)=-\nabla p+\nabla^2\boldsymbol{v}-Ga\ \ \mathbf{k} \tag{2.5b}$$

$$T_t+\boldsymbol{v}\bullet\nabla T=\nabla^2 T \tag{2.5c}$$

and the associated boundary conditions read

$$z=0:\qquad \boldsymbol{v}=0,\ \ T_z=-1 \tag{2.6a}$$

$$z=h(x,y,t):\qquad h_t+u\,h_x+v\,h_y=w \tag{2.6b}$$

$$(\mathbf{n}\bullet\nabla T)=-Bi\,T \tag{2.6c}$$

$$\left[u_x\left(1-h_x{}^2\right)+v_y\left(1-h_y{}^2\right)+\left(u_z+w_z\right)h_x-\left(u_y+v_x\right)h_xh_y+\left(w_y+v_z\right)h_y\right]$$
$$=\frac{p\left(1+h_x{}^2+h_y{}^2\right)^{3/2}+\Sigma\left[h_{xx}\left(1+h_y{}^2\right)-2h_xh_yh_{xy}+h_{yy}\left(1+h_x{}^2\right)\right]}{-2\sqrt{1+h_x{}^2+h_y{}^2}} \tag{2.6d}$$

$$2\left(w_z-u_x\right)h_x-\left(v_z+w_y\right)h_xh_y-\left(u_y+v_x\right)h_y+\left(u_z+w_x\right)\left(1-h_x{}^2\right)$$
$$=-MaT\,T_x\sqrt{1+h_x{}^2+h_y{}^2} \tag{2.6e}$$

$$2\left(w_z-v_y\right)h_y-\left(u_z+w_x\right)h_xh_y-\left(u_y+v_x\right)h_x+\left(v_z+w_y\right)\left(1-h_y{}^2\right)$$
$$=-MaT\,T_y\sqrt{1+h_x{}^2+h_y{}^2} \tag{2.6f}$$

2.2.4 Dimensionless base state

In dimensionless form, the base state (*i.e.*, Eq. 2.4) can be represented by

$$h_o=1,\ \boldsymbol{v}_o=0,\ T_o=1-z+\frac{1}{Bi},\ \ p_o=Ga(1-z) \tag{2.7}$$

It is important to note that the BVP represented by Eqs. 2.5 – 2.6 is now charac-

terized by the following sets of dimensionless parameters,

$$Bi = \frac{qH}{\kappa},\ Ga = \frac{gH^3}{\nu\alpha},\ Ma = \frac{\sigma_T \vartheta^2 H^3}{\rho\nu\alpha},\ Pr = \frac{\nu}{\alpha},\ \Sigma = \frac{\sigma_o H}{\rho\nu\alpha}$$

which are, respectively, the Biot number, Galileo number, Marangoni number, Prandtl number and the (inverse) Capillary number. Here, it is important to note that except for the Marangoni number (*Ma*), the remaining dimensionless parameters are defined in a manner similar to that in the extant literature [98–101]. However, since we are analyzing here the case of non-monotonic variation of surface tension with temperature, therefore, *Ma* is defined in a slightly different manner, and we name it the quadratic Marangoni number. Compared to linear Marangoni number (defined as $Ma_L = \sigma_T \vartheta H^2 / \rho\nu\alpha$ for fluids whose surface tension varies linearly with temperature [61-64]) the important feature of this quadratic Marangoni number is that, for $\sigma_T > 0$, the latter is always a positive quantity irrespective of the direction of heating (*i.e.*, the sign of ϑ). On the other hand, Ma_L can be either positive or negative depending on the direction of heating (even for $\sigma_T > 0$).

In the forthcoming sections, we now proceed to study the stability of this base state against both the long-wave and short-wave perturbations.

2.3 Long-wave Stability Theory

2.3.1 Lubrication approximation

Let us first study the stability of the base state against the long-wave disturbances. In order to analyze the evolution of such large-scale flows, here we use the lubrication approximation. Following this approximation, the coordinates, time and velocity are rescaled as

$$X = \varepsilon x,\ Y = \varepsilon y,\ Z = z,\ \mathcal{T} = \varepsilon^2 t,\ u = \varepsilon U,\ v = \varepsilon V,\ w = \varepsilon^2 W \tag{2.8}$$

here ε is a small parameter $(0 < \varepsilon << 1)$ and can be thought of as the ratio between H to the longitudinal length scale. Furthermore, we rescale the parameters *Bi* and Σ as

$$Bi = \varepsilon^2 b,\ \Sigma = \varepsilon^{-2}\varsigma \tag{2.9}$$

It may be noted that the scaling adopted in Eq. 2.9 differs from the conventional scaling $Bi \approx O(\varepsilon^4)$, which is typically considered in the study of long-wave Marangoni convection in a liquid film [102,103]. A different scaling is employed in this analysis, accounting the fact that the conventional scaling becomes inadequate at certain situations as demonstrated by Podolny *et al*. [104]. However, we do not impose any restriction on the magnitude of the Galileo number (*Ga*). Depending on the strength of the gravitational field, fluid layer thickness and its properties, *Ga* can vary between ultra-low to a very high value. For instance, for a 0.1 mm thick layer of water-based solution at the terrestrial environment, $Ga \approx O(10^2)$; whereas in the microgravity condition with $g \approx O(10^{-2})\,\mathrm{ms}^{-2}$, $Ga \approx O(10^{-1})$.

We now expand all the dependent variables of the problem in a power series with respect to ε^2 as follows:

$$(U,V,W) = (U_0,V_0,W_0) + \varepsilon^2 (U_1,V_1,W_1) + \ldots \tag{2.10a}$$

$$p = P_0 + \varepsilon^2 P_1 + \ldots \tag{2.10b}$$

$$T = -Z + \frac{1}{\varepsilon^2 b} + T_0 + \varepsilon^2 T_1 + \ldots \tag{2.10c}$$

It may be noted that, in Eq. 2.10, we have not presented an expansion for h. This is because the scaling in Eq. 2.8 is sufficient to ensure a slow variation of h, which further provides a small amplitude of surface deformation [105]. A comparison between Eq. 2.7 and 2.10 now reveal that the base state of the system corresponds to $P_0 = p_o$, $T_0 = 1$.

Substituting the rescaled fields (*i.e.*, Eqs. 2.8 – 2.10) into Eqs. 2.5 – 2.6, and applying the conventional technique of lubrication approximation, we obtain

$$U_{0X} + V_{0Y} + W_{0Z} = 0 \tag{2.11a}$$

$$P_{0X} = U_{0ZZ},\ P_{0Y} = V_{0ZZ},\ P_{0Z} = -Ga \tag{2.11b}$$

$$T_{0ZZ} = 0 \tag{2.11c}$$

$$\text{at } Z = 0\text{:} \quad U_0 = V_0 = W_0 = 0,\ T_{0Z} = 0 \tag{2.12a}$$

$$\text{at } Z = h(X,Y,\mathcal{T})\text{:} \quad W_0 = h_{\mathcal{T}} + U_0 h_X + V_0 h_Y,\quad T_{0Z} = 0$$

$$U_{0Z} = -Ma\left(T_0 + \frac{1}{\varepsilon^2 b} - h\right)\left(T_{0X} - h_X\right),\ V_{0Z} = -Ma\left(T_0 + \frac{1}{\varepsilon^2 b} - h\right)\left(T_{0Y} - h_Y\right) \quad (2.12b)$$

$$-P_0 = \varsigma\left(h_{XX} + h_{YY}\right)$$

The solutions of Eqs. 2.11($a-c$), subject to the boundary conditions given in Eqs. 2.12($a-b$) can be written as

$$U_0 = \frac{1}{2} Z\left(Z - 2h\right)\partial_X\left[Ga\, h - \varsigma\, \nabla^2 h\right] - Ma\, Z\left(\theta + \frac{1}{\varepsilon^2 b} - h\right)\left(\theta_X - h_X\right) \quad (2.13a)$$

$$V_0 = \frac{1}{2} Z\left(Z - 2h\right)\partial_Y\left[Ga\, h - \varsigma\, \nabla^2 h\right] - Ma\, Z\left(\theta + \frac{1}{\varepsilon^2 b} - h\right)\left(\theta_Y - h_Y\right) \quad (2.13b)$$

$$W_0 = \frac{1}{2} Z^2\, \nabla\cdot\left[\frac{1}{3}\left(3h - Z\right)\nabla\Im + Ma\Re\right] \quad (2.13c)$$

$$P_0 = Ga\,\left(h - Z\right) - \varsigma\, \nabla^2 h \quad (2.13d)$$

$$T_0 = \theta\left(X, Y, \mathcal{T}\right) \quad (2.13e)$$

where $\Im = Ga\, h - \varsigma\, \nabla^2 h$ and $\Re = \left(\theta + \frac{1}{\varepsilon^2 b} - h\right)\nabla\left(\theta - h\right)$.

In Eqs. 2.13($a-e$), $\nabla \equiv \left(\partial_X, \partial_Y, 0\right)$ is the two-dimensional projection of the gradient operator onto the $X-Y$ plane. Here, the base state, which corresponds to the motionless state of the film is given by

$$h = 1,\ \ \theta = 1 \quad (2.14)$$

2.3.2 Amplitude equations

In order to obtain the first amplitude equation, we use the condition $h_{\mathcal{T}} = -\nabla\cdot\int_0^h \mathbf{U}_0\, dZ$ which governs the evolution of the fluid layer thickness. This gives

$$h_{\mathcal{T}} = \nabla\cdot\left[\frac{1}{3} h^3\ \ \nabla\Im + \frac{1}{2} Ma\, h^2\, \Re\right] \quad (2.15)$$

The first term on the right-hand side of Eq. 2.15 takes into account the damping effect of gravity and surface tension on the surface deflection of the liquid layer. The second term represents the influence of thermocapillary induced flow on the liquid layer thickness.

The second amplitude equation is obtained from the heat transfer equation. Following the first-order expansion of Eq. 2.5(*c*) and the associated boundary conditions *i.e.*, Eqs. 2.6(*a*) and 2.6(*c*), we get

$$T_{1ZZ} = \theta_{\mathcal{T}} + U_0\, T_{0X} + V_0\, T_{0Y} - \nabla^2\theta - W_0 \tag{2.16}$$

$$\text{at } Z = 0: \qquad T_{1Z} = 0 \tag{2.17a}$$

$$\text{at } Z = h(X,Y,\mathcal{T}): \qquad T_{1Z} = \nabla\theta\cdot\nabla h - \frac{1}{2}(\nabla h)^2 - b(\theta - h) \tag{2.17b}$$

Now, integration of Eq. 2.16 subjected to the boundary conditions given in Eqs. 2.17(*a-b*) provides the second amplitude equation:

$$\begin{aligned} h\,\theta_{\mathcal{T}} = {} & \nabla\cdot\left(\frac{1}{8}h^4\,\nabla\Im + \frac{1}{6}Ma\Re\, h^3\right) + \left(\frac{1}{3}h^3\,\nabla\Im + \frac{1}{2}Ma\,\Re h^2\right)\cdot\nabla(\theta - h) \\ & + \nabla\cdot(h\,\nabla\theta) - \frac{1}{2}(\nabla h)^2 - b(\theta - h) \end{aligned} \tag{2.18}$$

The first two terms on the right-hand side of Eq. 2.18 take into account the advective transport of heat by the fluid; the third term stands for the heat conductivity in the longitudinal directions, while the last two terms take care of the heat loss from the free surface. As such, the set of amplitude Eqs. 2.15 and 2.18 govern the non-linear dynamics of the long-wave perturbations.

2.3.3 Linear stability analysis

The amplitude Eqs. 2.15 and 2.18 are non-linear in h and θ. We now make an effort to linearize these equations using small perturbation analysis. Substituting the perturbed fields $h = 1 + \delta$ and $\theta = 1 + \phi$, and linearizing the equations with respect to small disturbances we get

$$\delta_{\mathcal{T}} = \nabla^2\left[\frac{1}{3}\left(Ga\delta - \varsigma\,\nabla^2\delta\right) + \frac{1}{2}\frac{Ma}{\varepsilon^2 b}(\phi - \delta)\right] \tag{2.19a}$$

$$\phi_{\mathcal{T}} = \nabla^2\left[\phi + \frac{1}{8}\left(Ga\delta - \varsigma\,\nabla^2\delta\right) + \frac{1}{6}\frac{Ma}{\varepsilon^2 b}(\phi - \delta)\right] - b(\phi - \delta) \tag{2.19b}$$

Now, considering the perturbation fields to be proportional to $\exp(iKX + \lambda\mathcal{T})$ where K and $\lambda(=\lambda_r + i\lambda_i)$ are, respectively, the dimensionless wave number and

complex growth rate of the perturbations, we arrive at the following dispersion relation

$$\begin{aligned}&\lambda^2+(\lambda/3)\left[3b+K^2\left(3+Ga+\varsigma K^2-Ma/\,\varepsilon^2 b\right)\right]\\&-\left(K^2/144\varepsilon^2 b\right)\left[Ma\,K^2\left(72+Ga+\varsigma K^2\right)\right]+\left(K^2/3\right)\left[\left(b+K^2\right)\left(Ga+\varsigma K^2\right)\right]=0\end{aligned}\tag{2.20}$$

It may be noted that Eq. 2.20 possess both real and complex solutions. The real solution of Eq. 2.20 represents the monotonic instability, whereas the complex solution corresponds to the oscillatory instability. The stability threshold of the system for both kinds of instabilities is determined in the forthcoming sections.

2.3.3.1 *Monotonic instability*

We first start with the case of monotonic instability. At the monotonic instability threshold, the disturbance growth rate (λ) vanishes. Substituting $\lambda=0$ in Eq. 2.20, we obtain

$$Ma_{mon.}=\frac{48\,\varepsilon^2 b\left(b+K^2\right)\left(Ga+\varsigma\,K^2\right)}{K^2\left(72+Ga+\varsigma\,K^2\right)}\tag{2.21}$$

In terms of the unscaled wave number $k\left(=\varepsilon K\right)$, Biot number $\left(Bi\right)$ and inverse capillary number (Σ), Eq. 2.21 becomes

$$Ma_{mon.}=\frac{48\,Bi\left(Bi+k^2\right)\left(Ga+\Sigma\,k^2\right)}{k^2\left(72+Ga+\Sigma\,k^2\right)}\tag{2.22}$$

For a non-deformable free surface $\left(i.e.\text{ for } Ga+\Sigma\,k^2>>72\right)$ at large *k*, Eq. 2.22 reduces to

$$Ma_{mon.}=48Bi\tag{2.23}$$

2.3.3.2 *Oscillatory instability*

The oscillatory instability boundary is determined by the condition where λ attains a purely imaginary value $\lambda=i\lambda_i$. Here, λ_i is the oscillation frequency and is a real quantity. The neutral stability curve for the oscillatory instability mode is therefore given by

$$Ma_{osc.}=\varepsilon^2 b\left(3+\frac{3\,b}{K^2}+Ga+\varsigma\,K^2\right)\tag{2.24}$$

and the oscillation frequency is determined by the relation

$$\lambda_i = K^2\sqrt{\left(72+Ga+\varsigma K^2\right)\left(Ma_{osc.}-Ma_{mon.}\right)\Big/\ 144\,Bi} \tag{2.25}$$

In terms of the unscaled parameters $k\left(=\varepsilon K\right)$, Biot number $\left(Bi\right)$ and inverse capillary number (Σ), Eq. 2.24 can be re-written as

$$Ma_{osc.} = Bi\left(3+\frac{3\,Bi}{k^2}+Ga+\Sigma\,k^2\right) \tag{2.26}$$

The neutral stability curves for the long-wave monotonic and oscillatory modes of instability is presented in Fig. 2.2. For numerical calculations, consistent with the assumptions considered in the analysis, we use the following range for the parameters *Bi*, Σ and *Ga* [56]:

$$O(10^{-3}) \lesssim Bi \lesssim O(10^{-1}),\quad O(10^{2}) \lesssim \Sigma \lesssim O(10^{4}),\quad O(1) \lesssim Ga \lesssim O(10)$$

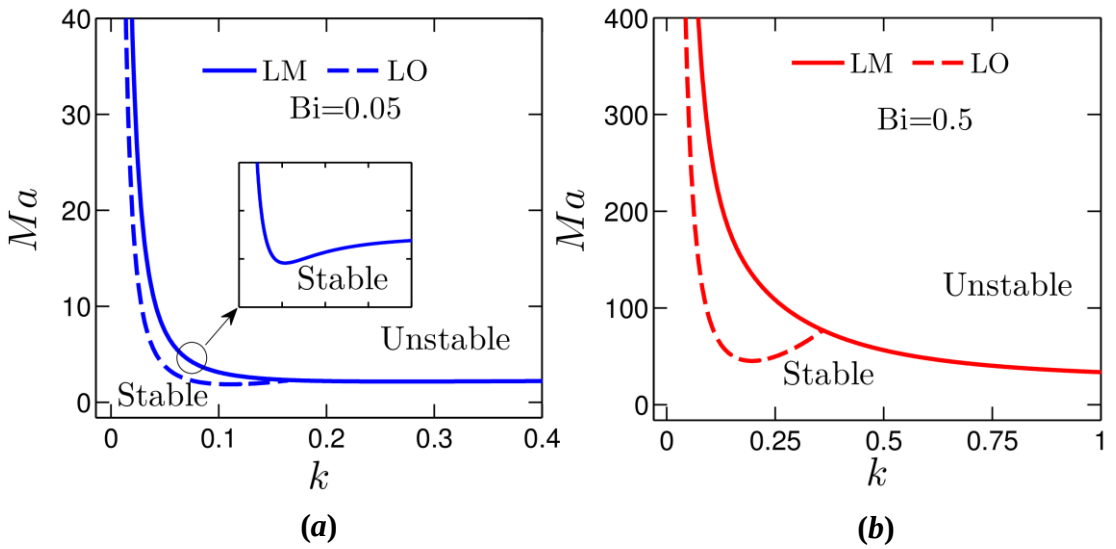

Figure 2.2: Neutral stability curves for the monotonic (solid lines) and oscillatory (dashed lines) modes at $Pr=1$, $Ga=10$, $\Sigma=10^3$. Panel (*a*) corresponds to $Bi=0.05$, panel (*b*) corresponds to $Bi=0.5$. The inset in panel (*a*) shows the zoomed-in view of the stability curve.

From Fig. 2.2, it can be observed that there exists a minimum Marangoni number only above which the instability first appears in the liquid layer. We call this Marangoni number the critical Marangoni number $\left(Ma_c\right)$ and the corresponding disturbance wave number (*k*) as the critical wave number $\left(k_c\right)$. A comparison between panels (*a*) and (*b*)

reveals that the critical Marangoni number (Ma_c) increases with the increasing value of the Biot number (Bi). This suggests that the higher values of Bi enhances the stability of the system. It is important to note that *Bi* characterizes in this analysis the heat loss from the free surface of the liquid film. Therefore, the higher is the heat transfer rate from the free surface; the higher will be the stability of the system. Figure 2.2 further demonstrates that for $Bi = 0.05$, the oscillatory mode is critical, whereas for $Bi = 0.5$ the monotonic mode is critical. A detailed discussion on the variation of instability modes depending on the values of *Bi* is provided later in Section 2.4.

Another key observation from Fig 2.2 is that for $Bi = 0.05$ the neutral stability curve for the monotonic mode has a minimum within finite values of k. On the other hand, for $Bi = 0.5$, this minimum outside the long-wave regime (*i.e.*, $k \gtrsim O(1)$). In this connection, it is important to note from Eq. 2.22 that the neutral stability curve for the monotonic mode has a minimum at finite values of k only for $Bi\,\Sigma < 72$. The critical wave number (k_c) and the critical Marangoni number (Ma_c) corresponding to this minimum are given by

$$k_{c,\,mon.} = \sqrt{\frac{Bi\,Ga\,\Sigma + \sqrt{Bi^2 Ga^2 \Sigma^2 + Bi\,Ga\,\Sigma\left(72+Ga\right)\left(72-Bi\,\Sigma\right)}}{\Sigma\left(72-Bi\,\Sigma\right)}} \tag{2.27}$$

and,
$$Ma_{\,c,\,mon.} = \frac{48Bi\left[\Pi + Bi\,\Sigma\left(72-Bi\,\Sigma\right)\right]\left[Ga\left(72-Bi\,\Sigma\right)+\Pi\right]}{\Pi\left[\left(72-Bi\,\Sigma\right)\left(72+Ga\right)+\Pi\right]} \tag{2.28}$$

respectively, where $\Pi = BiGa\,\Sigma + \sqrt{Bi^2 Ga^2 \Sigma^2 + BiGa\,\Sigma\left(72+Ga\right)\left(72-Bi\,\Sigma\right)}$.

On the other hand, for $Bi\,\Sigma > 72$, this minimum of this neutral stability curve occurs at $k \to \infty$ with $Ma_c = 48Bi$ as can be seen in Fig. 2.2(*b*).

The neutral stability curve for the oscillatory instability mode also presents a minimum as can be observed from Fig. 2.2. The critical Marangoni number $\left(Ma_{\,c,\,osc.}\right)$ and disturbance wave number $\left(k_{\,c,\,osc.}\right)$ corresponding to this minimum is given by

$$\mathrm{Ma}_{c,\,osc.} = Bi\left(3 + Ga + 2\sqrt{3\,Bi\,\Sigma}\right), \qquad k_{c,\,o} = \left(\frac{3Bi}{\Sigma}\right)^{1/4} \tag{2.29}$$

However, irrespective of the values of *Bi*, such disturbances always appear in the long-wave form.

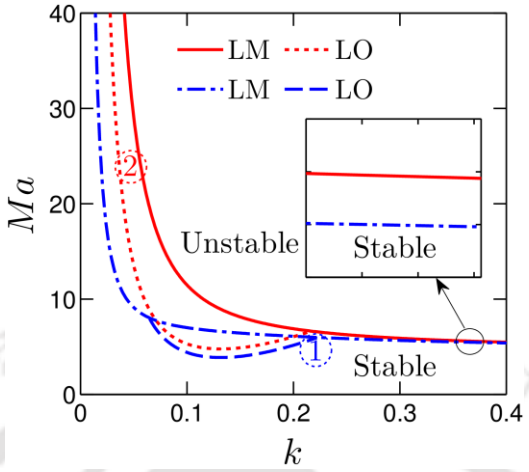

Figure 2.3: Neutral stability curves for the long-wave monotonic (solid and dash-dotted lines) and oscillatory modes (dotted and dashed lines) at different values of *Ga*. Lines marked by 1 and 2 correspond to $Ga = 1$ and $Ga = 10$ respectively. The inset shows the zoomed-in view of the stability curve at higher wave number. $Pr = 1$, $\Sigma = 10^3$ and $Bi = 0.1$.

We demonstrate in Fig. 2.3 the effect of Galileo number (Ga) on the stability of the system. In this analysis, since $\mathbf{g}$ is non-dimensionalized as *Ga*, therefore, Fig. 2.3 essentially addresses the effect of gravity on the stability threshold of the liquid layer. It can be observed that the higher values of *Ga* enhance the stability of the system. This is because, at larger values of *Ga*, the stabilizing action of gravity dominates the destabilizing effect of thermocapillarity, thus enhancing the stability of the system as witnessed from Fig. 2.3.

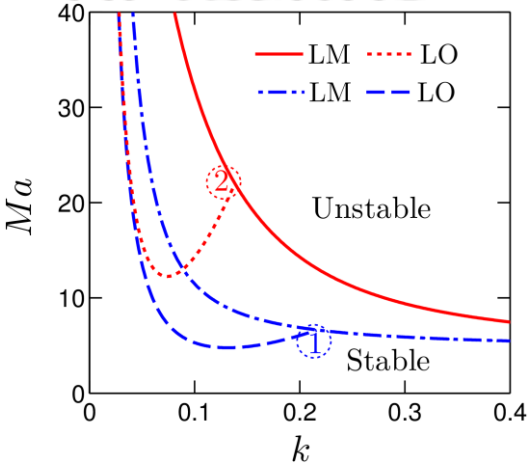

Figure 2.4: Neutral stability curves for the long-wave monotonic (solid and dash-dotted lines) and oscillatory modes (dotted and dashed lines) at different values of Σ. $Pr = 1$, $Ga = 10$ and $Bi = 0.1$. Lines marked by 1 and 2 correspond to $\Sigma = 10^3$ and $\Sigma = 10^4$ respectively.

Figure 2.4 depicts the effect of Σ (inverse capillary number) on the stability threshold of the system. In this study, since Σ represents the non-dimensional surface tension; therefore, Fig. 2.4 essentially demonstrates the effect of surface tension on the stability of the liquid layer. It can be observed that the increasing values of Σ enhances the stability of the system. In this context, it may be mentioned that the surface tension is a fluid property that tries to stabilize a system by dampening the surface deflections. Hence, the increasing magnitude of surface tension (and thus Σ) increases the stability of the fluid layer by reducing the surface deformations as can be verified from Fig. 2.4.

2.4 Short-wave Stability Theory

It is worth noting that the analysis presented in section 2.3 remains accurate only for small values of *k*. Therefore, an attempt is made in this section to study the stability picture for arbitrary values of the disturbance wave number.

2.4.1 Linear stability analysis

Since the problem under present consideration is invariant to the rotation of the system in the $x-y$ plane, we therefore consider two-dimensional infinitesimal perturbations only in the $x-z$ plane for analyzing the stability of the base state in this section. Substituting the perturbed fields $\boldsymbol{v} = (u, 0, w)$, $p = p_0 + P$, $T = T_0 + \theta$ and $h = 1 + \xi$, and linearizing Eqs. 2.5 – 2.6 with respect to these small disturbances, we get

$$\nabla \bullet \boldsymbol{v} = 0 \tag{2.30a}$$

$$Pr^{-1}\boldsymbol{v}_t = -\nabla P + \nabla^2 \boldsymbol{v} \tag{2.30b}$$

$$\theta_t = \nabla^2 \theta + w \tag{2.30c}$$

$$\text{at } z = 0: \qquad \boldsymbol{v} = 0, \quad \theta_z = 0 \tag{2.31a}$$

$$\text{at } z=1: \quad \xi_t = w,\ P - Ga\xi = -\Sigma\xi_{xx} + 2w_x,\ u_z + w_x = -Ma\left(\theta_x - \xi_x\right)/Bi \qquad (2.31b)$$

$$\theta_z = -Bi\left(\theta - \xi\right)$$

Now, utilizing the stream function relations $u = \psi_z$ and $w = -\psi_x$, we can write Eqs. 2.30 – 2.31 in the following form

$$Pr^{-1}\frac{\partial \nabla^2\psi}{\partial t} = \nabla^4\psi \qquad (2.32a)$$

$$\theta_t = \nabla^2\theta - \psi_x \qquad (2.32b)$$

$$\text{at } z=0: \qquad \psi = 0, \quad \psi_z = 0, \quad \theta_z = 0 \qquad (2.33a)$$

$$\text{at } z=1: \ \xi_t = -\psi_x, \ P - Ga\,\xi = -\Sigma\xi_{xx} - 2\frac{\partial^2\psi}{\partial x\,\partial z}, \qquad (2.33b)$$

$$\psi_{zz} - \psi_{xx} = -Ma\left(\theta_x - \xi_x\right)/Bi \qquad \theta_z = -Bi\left(\theta - \xi\right)$$

Representing the perturbation fields to be proportional to $\exp\left(-\lambda t + ikx\right)$, where $\lambda\left(=\lambda_r + i\lambda_i\right)$ and k are respectively, the disturbance growth rate and disturbance wave number, Eqs. 2.32 – 2.33 become

$$\psi^{iv} - \left(2k^2 - \frac{\lambda}{Pr}\right)\psi'' + \left(k^2 - \frac{\lambda}{Pr}\right)k^2\,\psi = 0 \qquad (2.34a)$$

$$\theta'' + \left(\lambda - k^2\right)\theta = i\,k\,\psi \qquad (2.34b)$$

$$\text{at } z=0: \qquad \psi = 0, \ \psi' = 0, \ \theta' = 0 \qquad (2.35a)$$

$$\text{at } z=1: \qquad \lambda\xi = ik\psi, \qquad \psi''' - \left(3k^2 - \frac{\lambda}{Pr}\right)\psi' = i\,k\left(Ga + \Sigma k^2\right)\xi \qquad (2.35b)$$

$$\psi'' + k^2\psi = -ikMa\left(\theta - \xi\right)/Bi, \qquad \theta' = -Bi\left(\theta - \xi\right)$$

In Eqs. 2.34 – 2.35 the prime denotes the z – derivative, and the superscript iv represents the fourth-order derivative.

2.4.1.1 *Monotonic instability*

It is mentioned earlier that for the monotonic instability mode, $\lambda = 0$ at the stability border. Substituting $\lambda = 0$ in Eqs. 2.34 – 2.35 and solving for ψ and θ, we obtain

$$\psi = a_1 \sinh k\,z - a_1 k\,z \cosh k\,z + a_2 k\,z \sinh k\,z \tag{2.36}$$

$$\theta = \frac{i}{4k}\begin{bmatrix} 3a_1 k\,z \cosh k\,z - 3a_1 \sinh k\,z - a_1 k^2 z^2 \sinh k\,z \\ + a_2 k^2 z^2 \cosh k\,z - a_2 k\,z \sinh k\,z + a_3 \cosh k\,z \end{bmatrix} \tag{2.37}$$

It is important to note that the above solutions for ψ and θ are obtained by applying the boundary conditions at the $z = 0$ plane. Substituting the boundary conditions at $z = 1$ into the solution of ψ and θ, and solving for Ma, we get the following expression for the neutral stability curve:

$$Ma_{mon.} = \frac{8\,k\,Bi\left(Ga + \Sigma\,k^2\right)\left(\cosh k \sinh k - k\right)\left(k \sinh k + Bi \cosh k\right)}{\left(Ga + \Sigma\,k^2\right)\left(\cosh k \sinh^2 k - 2\,k \sinh k + k^2 \cosh k - k^3 \sinh k\right) + 8\,k^5 \sinh k} \tag{2.38}$$

It is to be noted that in the limit $k << 1$, $Bi \sim k^2$ and $\Sigma \sim k^{-2}$, Eq. 2.38 resembles Eq. 2.22.

2.4.1.2 *Oscillatory instability*

For the oscillatory instability mode $\lambda_i \neq 0$ at the stability border. Solving Eqs. 2.34 – 2.35 using the boundary conditions at $z = 0$, we get the solution for ψ and θ as given below

$$\psi = -c_1 \left(k_1 / k\right) \sinh k\;z + c_1 \sinh k_1\,z - c_2 \cosh k\,z + c_2 \cosh k_1\,z \tag{2.39}$$

$$\theta = \frac{i}{2\lambda k_1 k_2}\begin{bmatrix} -2k\,c_1 k_1^{\,2} \exp\left(-k_2 z\right) + k\lambda c_1 \exp\left(-k_2 z\right) - 2c_1 k_1^{\,2} k_2 \sinh k\,z + \lambda c_1 k\,k_2 z \cosh k_1 z \\ -2k\,k_1 c_2 k_2 \cosh k\,z + \lambda c_2 k\,k_2 z \sinh k_1 z + 2\lambda k_1 k_2 c_3 \cosh k_2 z \end{bmatrix} \tag{2.40}$$

Employing the boundary conditions at $z = 1$ into the solution of ψ and θ, and solving for Ma, we obtain the expression that governs the stability threshold of the system against the oscillatory disturbances.

$$Ma_{osc.} = \frac{\aleph_1\,\aleph_4 + \aleph_0\,\aleph_1\,\aleph_5}{\aleph_1\,\aleph_6 + \aleph_2\,\aleph_8 + \aleph_0\,\aleph_1\,\aleph_7 + \aleph_0\,\aleph_3\,\aleph_8} \tag{2.41}$$

The quantities $\aleph_0 - \aleph_8$ appearing in Eq. 2.41 are lengthy. For the brevity in presentation, we have defined these parameters in appendix A.

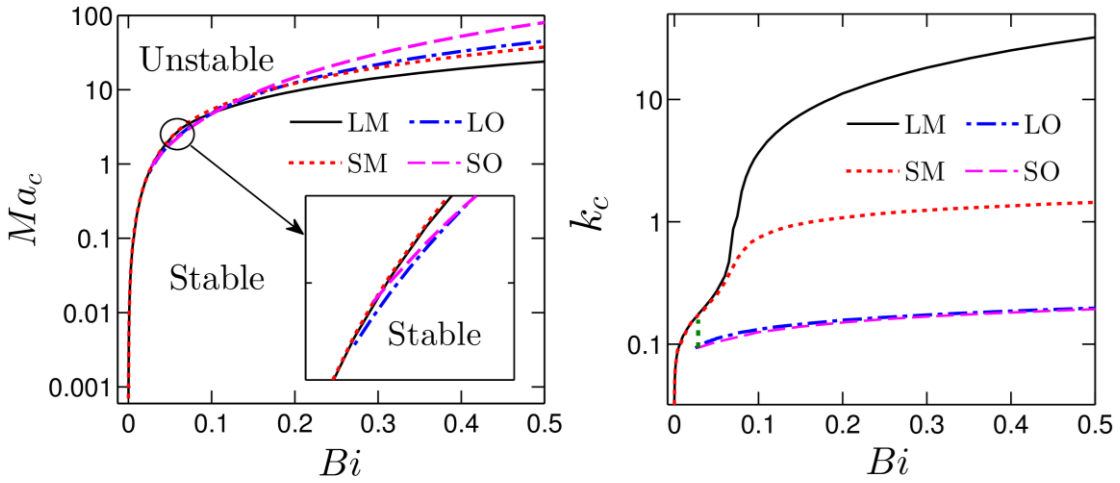

Figure 2.5: Variation of the (*a*) critical Marangoni number, and (*b*) the critical wave number with Bi at $Pr=1$, $Ga=10$, $\Sigma=10^3$. In panels (*a*) and (*b*); LM, LO, SM and SO corresponds to the long-wave monotonic, long-wave oscillatory, short-wave monotonic and short-wave oscillatory respectively. The inset in panel (*a*) shows the zoomed-in view at small Biot number.

Figures 2.5($a-b$) shows the variation of the critical Marangoni number (Ma_c) and the disturbance wave number (k_c) with Biot number (Bi). Clearly, the stability of the system increases with *Bi* as discussed in section 2.3. Interestingly, Fig. 2.5(*a*) demonstrates that there exists a particular range of *Bi* only for which the oscillatory mode becomes critical. This range depends on the deformability of the free surface (*i.e.*, magnitude of the parameters Ga and Σ) as shown in Fig. 2.6. The monotonic mode becomes critical outside this range.

A closer look at Figs. 2.6($a-b$) further reveals that the results of the long-wave theory agree with the short-wave analysis only for small values of Bi. For the monotonic mode of instability, this range is $0<Bi<0.072$ corresponding to $0<Bi\Sigma<72$. Within this regime, the critical wave number (k_c) predicted by the long-wave analysis agrees with the short-wave analysis in a fairly accurate manner as can be seen from Fig. 2.5(*b*). However, for $Bi>0.072$, k_c associated with monotonic disturbance grows rapidly, thus limiting the domain of applicability of the long-wave approximation only within the range $0<Bi\Sigma<72$.

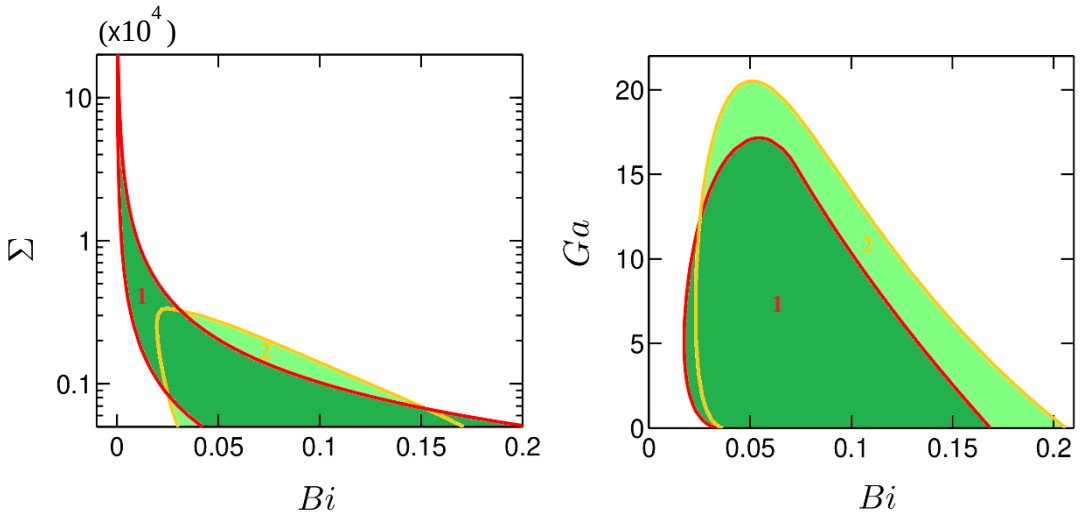

Figure 2.6: Phase diagrams depicting the regimes of dominant instability mode in (*a*) *Bi* - Σ plane at $Pr = 1$, $Ga = 10$ (*b*) *Bi* – *Ga* plane at $Pr = 1$, $\Sigma = 10^3$. The oscillatory mode becomes dominant for parameter values that lie within the shaded region. Shaded region 1 corresponds to the results of the long-wave theory, while regime 2 refers to the results of the short-wave analysis. For parameter values that lie towards the left of the shaded domains 1 and 2, the long-wave monotonic mode gets dominant in the system, whereas for parameter values that lie on its right, the short-wave monotonic mode becomes dominant.

We depict in Fig. 2.7 the variation of critical Marangoni number (Ma_c) and disturbance wave number (k_c) with Galileo number (Ga). It can be observed that the

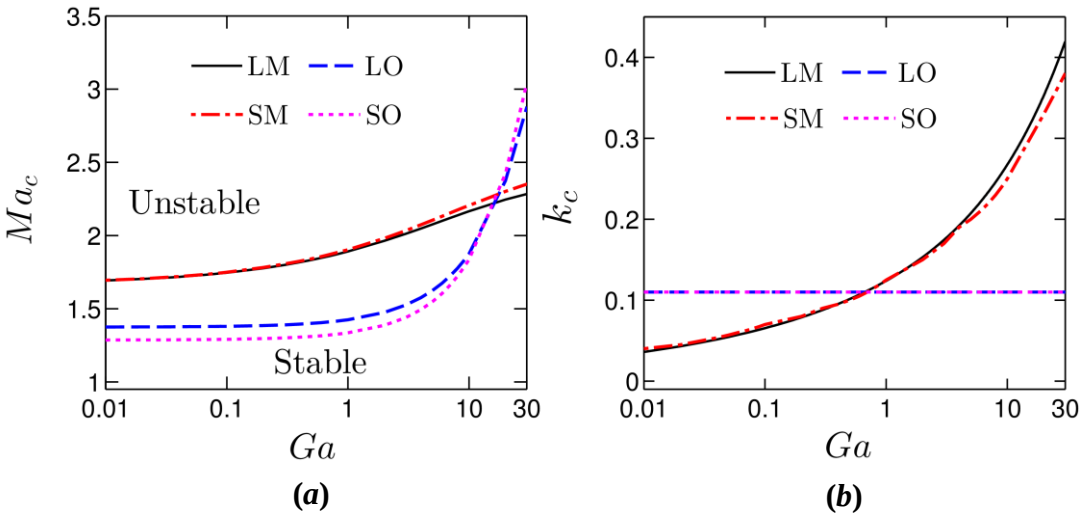

Figure 2.7: (*a*) Variation of the critical Marangoni number and (*b*) the critical wave number with Galileo number at $Bi = 0.05$, $Pr = 1$, $\Sigma = 10^3$.

stability of the system increases with *Ga* for both the monotonic and oscillatory disturbances. Figure 2.7(*a*) further demonstrates that the oscillatory mode is critical only below a particular value of $Ga(\approx 17)$, after which the monotonic mode becomes critical. Since the increasing magnitude of *Ga* reduces the deformability of the free surface, this ensures the fact that for pure thermocapillary driven convection, the oscillatory instability appears only for a fluid layer with a deformable free surface.

The variation of the critical wave number (k_c) with *Ga* is shown in Fig. 2.7(*b*). It can be observed that k_c for the monotonic disturbances increases with *Ga*. On the other hand, for the oscillatory perturbations, k_c remains independent of *Ga*. Hence, the long-wave disturbances are more likely to be visible in the microgravity environment.

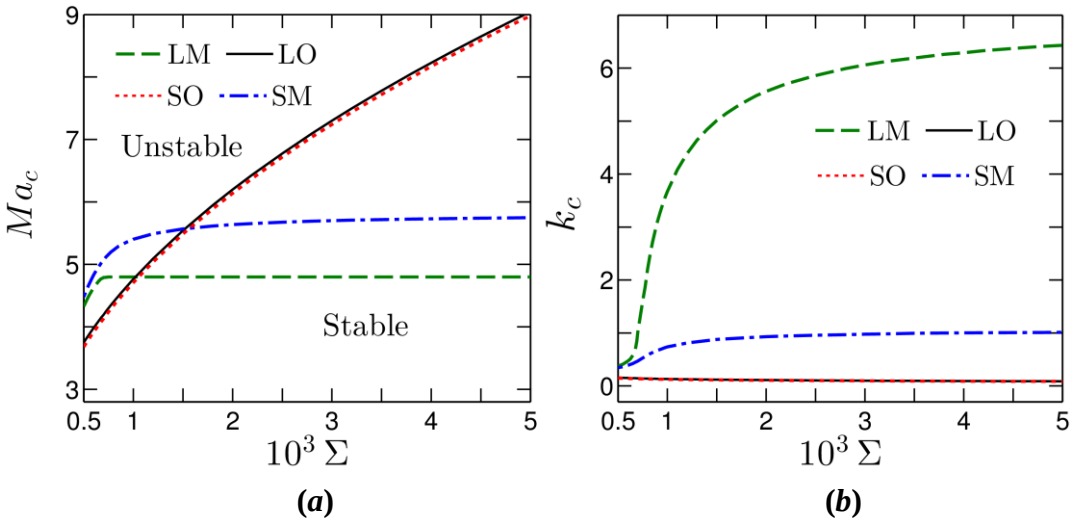

Figure 2.8: Variation of (*a*) the critical Marangoni number and (*b*) the critical wave number with Σ at $Bi = 0.1$, $Pr = 1$, $Ga = 10$.

Figures 2.8(*a*-*b*) show the variation of critical Marangoni number (Ma_c) and disturbance wave number (k_c) with the inverse capillary number (Σ). It can be observed that up to a certain critical value of Σ ($\Sigma = 720$ corresponding to $Bi\,\Sigma = 72$), Ma_c predicted by the long-wave theory increases steadily for the monotonic mode; after which the variation becomes independent of Σ. This is because, for $Bi\,\Sigma \geq 72$, the neutral stability curve for the monotonic mode of instability attains the limiting value

$Ma_c = 48Bi$ as predicted by the long-wave theory (Eq. 2.23). The long-wave theory and the short-wave analysis also lost the quantitative agreement from this point onwards. Figure 2.8(*a*) further reveals that the oscillatory mode becomes critical only for small values of Σ, since the increasing values of Σ reduces the deformability of the free surface.

We demonstrate in Fig. 2.8(*b*) the variation of k_c with Σ. It is found that the monotonic disturbances emerge in the long-wave form below $\Sigma = 720$ (corresponding to $Bi\,\Sigma = 72$). However, for $Bi\Sigma > 72$, the monotonic disturbances appear in the short-wave form. A competition between the long-wave and short-wave monotonic disturbances is therefore possible in the system for $Bi\,\Sigma = 72$. On the other hand, irrespective of the values of Σ, the oscillatory disturbances always appear in the long-wave form.

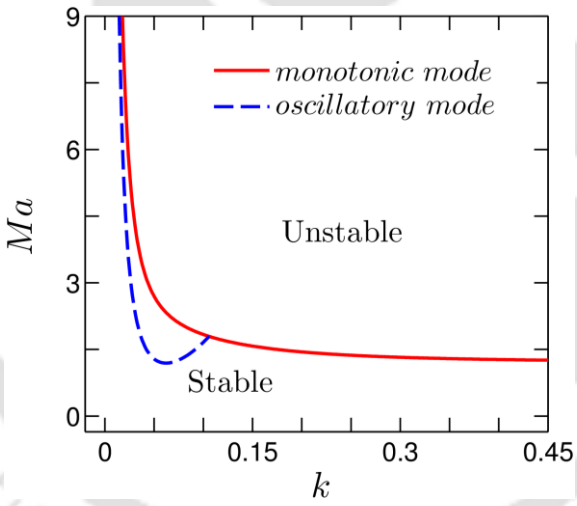

Figure 2.9: Neutral stability curves for a 0.05 mm thick film of the aqueous 1-butanol solution. $\nu = 100$ cSt, $Bi = 0.025$, $Ga = 6$ and $\Sigma = 5\times10^3$.

Now, in order to predict the conditions at the onset of convection for a realistic system, we plot in Fig. 2.9 the neutral stability curve for the aqueous 1-butanol solution. Such a fluid layer demonstrates a non-monotonic variation of surface tension with temperature as verified from experimental observations of Villers and Platten [59]. From Fig. 2.9, we can observe that, for the considered set of dimensionless parameters, the oscillatory mode is critical with $Ma_c = 1.19$ and $k_c = 0.06$. For the film thickness of 0.05 mm, this critical Marangoni number is attained at a temperature difference of 6 K with

the characteristic wavelength 0.5 mm. This theoretical prediction is expected to help in carrying out an experimental analysis of the present problem.

2.5 Summary

Marangoni instability in a thin Newtonian liquid film is investigated in this chapter under the framework of linear stability analysis. The investigation aimed at understanding the effect of non-monotonic variation of surface tension with temperature on the onset of instability in the system. The expressions governing the stability threshold of the system is derived here analytically for both the monotonic and oscillatory instability modes. Using the scaling $k \sim (Bi)^{1/2}$, we have derived a set of amplitude equations (Eqs. 2.15 and 2.18) that govern the coupled non-linear evolution of the fluid layer thickness as well as temperature in the long-wave regime. It is found that non-linear variation of surface tension with temperature non-trivially changes the stability behavior of the liquid layer. This analysis further reveals that the deformability of the free surface and the heat transfer rate from this free surface selects the preferred mode of instability for the system.

Chapter 3

Long-wave Marangoni Instability in a Viscoelastic Liquid Film

In this chapter, the Marangoni instability phenomenon is investigated for in a thin viscoelastic liquid film confined between its deformable free surface and a rigid substrate. Apart from the conventional short-wave oscillatory mode, a novel long-wave oscillatory instability mode is detected in this study for heating the system from below. This long-wave mode is studied here analytically deriving a set of nonlinear evolution equations.

3.1 Introduction

In the previous chapter, we have studied the Marangoni instability in a Newtonian liquid film for which surface tension varies non-monotonically with temperature. Despite a remarkable advancement towards understanding this instability phenomenon in Newtonian fluids, Marangoni instability in viscoelastic liquids has still remained much unexplored. The previously reported investigations in the literature [71–73] suggests that both the monotonic and oscillatory disturbances can emerge in such a liquid film. Quite notably, in these analyses, the fluid layer was considered to be confined between a non-deformable free surface and a perfectly conducting rigid substrate. Under such circumstances, the disturbances are found to appear only in the short-wave form.

The present work aims at revealing the instability modes in a viscoelastic liquid film confined between an insulating solid substrate and a deformable free surface. It is to be noted that here we deal with the case in which heat flux on the boundary with the substrate is fixed; which is different from all the earlier circumstances where the

The contents of this chapter have been published as Sarma, R. and Mondal, P. K. (2019) "Marangoni instability in a heated viscoelastic liquid film: Long-wave versus short-wave perturbations", Phys. Rev. E, vol. 100, pp. 013103.

temperature at the solid substrate was specified. Performing linear stability analysis, we demonstrate that both long-wave and short-wave Marangoni instabilities can appear in such a system under various parameter domains. This chapter is organized as follows: we start with the mathematical formulation of the problem in Section 3.2. A linear stability analysis of the system is then carried out in Section 3.3. The long-wave instability mode is investigated in Section 3.4 deriving a set of nonlinear evolution equations. We study the short-wave instability mode in Section 3.5. And finally, the main conclusions from this analysis are summarized in Section 3.6.

3.2 Mathematical Formulation of the Problem

The schematic of the physical system under investigation is shown in Fig. 3.1. We consider a thin, two-dimensional layer of an incompressible viscoelastic fluid in the gravitational field **g**. Since the physical problem at hand is invariant with respect to the rotation of the system in the $x-y$ plane, we consider a two-dimensional system in the $x-z$ plane. The liquid layer is confined between a heated solid substrate (of lower thermal conductivity compared to the liquid) and a deformable free surface that can exchange heat with the ambient air. We assume the layer to be of the infinite horizontal extent with average thickness *H*. Due to the continuous heating from below, a transverse temperature gradient prevails in the entire liquid layer, which is specified to be $-\vartheta$ at

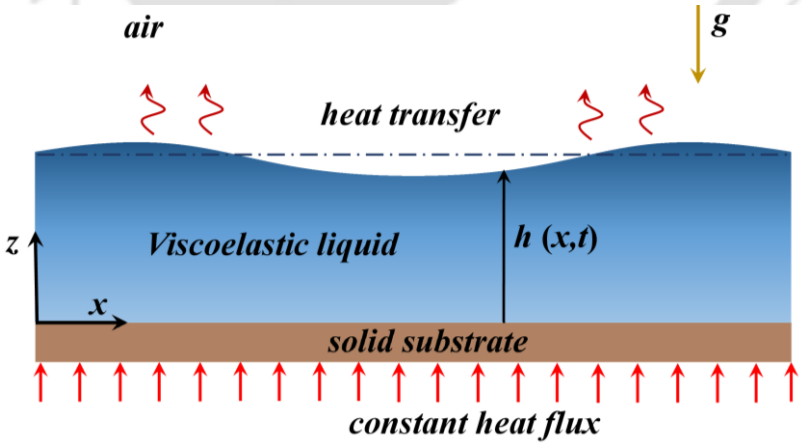

Figure 3.1: Sketch defining the physical system under study. A thin viscoelastic liquid film, resting on a solid substrate of very low thermal conductivity and having a deformable free surface is subjected to heating from below. The dashed-dotted line corresponds to the undisturbed interface at the equilibrium state.

$z = 0$. Now, above a certain critical temperature gradient, the thermocapillary effect induces Marangoni convection in the liquid layer. In this analysis, since the layer is considered to be sufficiently thin; the effect of buoyancy can be safely neglected in comparison to the Marangoni effect. To account for the thermocapillary effect of viscoelastic fluid, here, we assume the surface tension σ to vary monotonically with temperature, dictated by the relationship:

$$\sigma = \sigma_o - \sigma_T (T - T_\infty) \tag{3. 1}$$

where σ_o is the surface tension at the ambient temperature T_∞, and $\sigma_T = -(d\sigma/dT) > 0$.

3.2.1 Governing equations

For this thermocapillary driven convection, the equations governing the fields of velocity $\boldsymbol{v}$ **(***u*, *0*, *w***)**, pressure *p*, and temperature *T* in the bulk of the liquid layer can be represented, respectively, by the continuity, the Cauchy momentum, and the thermal energy equation

$$\nabla \bullet \ \boldsymbol{v} = 0 \tag{3.2a}$$

$$\rho\left(\frac{\partial \boldsymbol{v}}{\partial t} + \boldsymbol{v} \bullet \nabla \boldsymbol{v}\right) = -\nabla p + \nabla \bullet \boldsymbol{\tau} - \rho g \ \mathbf{k} \tag{3.2b}$$

$$\frac{\partial T}{\partial t} + \boldsymbol{v} \bullet \nabla T = \alpha \ \nabla^2 T \tag{3.2c}$$

where *t* represents time, $\boldsymbol{\tau} = \begin{bmatrix} \boldsymbol{\tau}_{xx} & \boldsymbol{\tau}_{xz} \\ \boldsymbol{\tau}_{zx} & \boldsymbol{\tau}_{zz} \end{bmatrix}$ is the deviatoric stress tensor, $\mathbf{k}$ is the unit vector in the *z*-direction, μ_o is the zero-shear-rate viscosity, and $\nabla \equiv (\partial/\partial x, \partial/\partial z)$.

The set of governing Eqs. 3.2(*a*-*c*) is subjected to the following boundary conditions. At the solid-liquid interface, *i.e.*, at the $z = 0$ plane, the boundary conditions reflect the no-slip condition for velocity and a specified heat flux, represented respectively by,

$$\text{at } z = 0: \qquad u = w = 0, \qquad \frac{\partial T}{\partial z} = -\vartheta \tag{3.3a}$$

At the liquid-air interface, *i.e.*, at $z = h(x,t)$, the boundary conditions constitute the kinematic boundary condition, the heat transfer governed by Newton's law of cooling and the balance of tangential as well as normal stress components, given respectively by,

at $z = h(x,t)$: $$w = \frac{\partial h}{\partial t} + u\,\frac{\partial h}{\partial x}, \tag{3.3b}$$

$$-\frac{\kappa}{\sqrt{1+\left(\partial h/\partial x\right)^2}}\left(\frac{\partial T}{\partial z} - \frac{\partial h}{\partial x}\frac{\partial T}{\partial x}\right) = q\left(T - T_\infty\right), \tag{3.3c}$$

$$\frac{1}{\sqrt{1+\left(\partial h/\partial x\right)^2}}\left\{\tau_{xz}\left[1-\left(\frac{\partial h}{\partial x}\right)^2\right] + \tau_{zz}\frac{\partial h}{\partial x} - \tau_{xx}\frac{\partial h}{\partial x}\right\} = \frac{\partial \sigma}{\partial x}, \tag{3.3d}$$

$$-p + \frac{1}{1+\left(\partial h/\partial x\right)^2}\left[\tau_{zz} + \tau_{xx}\left(\frac{\partial h}{\partial x}\right)^2 - 2\,\tau_{xz}\frac{\partial h}{\partial x}\right] = \sigma\frac{\partial^2 h/\partial x^2}{\left[1+\left(\partial h/\partial x\right)^2\right]^{3/2}} \tag{3.3e}$$

It may be mentioned here that, in Eq. 3.3, w is the z-component of velocity, while q denotes the heat transfer coefficient representing the rate of heat transfer from the fluid layer to the ambient air at temperature T_∞.

3.2.1.1 *Constitutive model for the liquid*

Viscoelastic liquids exhibit complex rheology under the simultaneous actions of viscosity and elasticity. A wide variety of constitutive relationships, comprising of both linear and nonlinear models have been developed over the years to describe the rheology of viscoelastic liquids. In this analysis, we proceed with the linear Maxwell model [62]:

$$\boldsymbol{\tau} + \hat{\lambda}\frac{\partial \boldsymbol{\tau}}{\partial t} = \mu_o\left[\left(\nabla \mathbf{v}\right) + \left(\nabla \mathbf{v}\right)^T\right], \tag{3.4}$$

which characterizes the liquid by a single relaxation time $\hat{\lambda}$ without incorporating the rheological nonlinearity. $\hat{\lambda}$ is interpreted here as the longest relaxation time out of the spectrum of relaxation time exhibited by the liquid.

The reasons behind adopting this particular constitutive model for this investigation are as follows: First, in the present convection phenomenon, motion is developed in a liquid film which was at rest in its equilibrium state. This indicates that the shear rates involved with the underlying process are also extremely small. A nonlinear model (*viz*. the upper-convected Maxwell model, wherein the ordinary time derivative of $\boldsymbol{\tau}$ in Eq. 3.4 is replaced by the "upper-convected" time derivatives) is essential to describe the flow dynamics only at higher shear rates. Second, since a linear stability analysis will be carried out around a quiescent base state, any nonlinear terms in the constitutive equation will not make here any contribution to the final linearized set of

equations. Therefore, the stability picture obtained using a linear model will be identical to that with the inclusion of the upper-convected terms. The aspects suggest that the linearized Maxwell model is deemed sufficient to reveal the basic effect of elasticity for this analysis.

3.2.2 Non-dimensionalization

Now, to cast the BVP formed by Eqs. 3.2-3.4 in non-dimensional form, we define the following set of dimensionless variables. It may be noted that the characteristic scales employed here coincide with those in the previous chapter.

$$\left(\bar{x},\bar{z}\right)=\frac{(x,z)}{H},\ \bar{h}=\frac{h}{H},\ \bar{t}=\frac{t}{H^2/\alpha},\ \left(\bar{u},\bar{w}\right)=\frac{u,w}{\left(\alpha/H\right)},$$
$$\bar{\tau}=\frac{\tau}{\mu_o\alpha/H^2},\ \bar{p}=\frac{p}{\mu_o\alpha/H^2},\ \bar{T}=\frac{T-T_\infty}{\vartheta H} \tag{3.5}$$

However, for the convenience in presentation, we drop the overbar sign from the non-dimensional variables in the rest of this paper. The governing equations and the associated boundary conditions in dimensionless form thus read,

$$\nabla\bullet\ \boldsymbol{v}=0 \tag{3.6a}$$

$$Pr^{-1}\left(\frac{\partial\boldsymbol{v}}{\partial t}+\boldsymbol{v}\bullet\nabla\boldsymbol{v}\right)=-\nabla p+\nabla\bullet\boldsymbol{\tau}-Ga\,\mathbf{k} \tag{3.6b}$$

$$\frac{\partial T}{\partial t}+\boldsymbol{v}\bullet\nabla T=\nabla^2T \tag{3.6c}$$

$$\text{at } z=0: \qquad u=w=0, \qquad \frac{\partial T}{\partial z}=-1 \tag{3.7a}$$

$$\text{at } z=h\left(x,t\right): \qquad w=\frac{\partial h}{\partial t}+u\frac{\partial h}{\partial x}\ , \tag{3.7b}$$

$$\frac{1}{\sqrt{1+\left(\partial h/\partial x\right)^2}}\left[\frac{\partial T}{\partial z}-\frac{\partial h}{\partial x}\frac{\partial T}{\partial x}\right]=-Bi\ T\ , \tag{3.7c}$$

$$-p+\frac{1}{1+\left(\partial h/\partial x\right)^2}\left[\tau_{z\,z}+\tau_{x\,x}\left(\frac{\partial h}{\partial x}\right)^2-2\tau_{x\,z}\frac{\partial h}{\partial x}\right]=\Sigma\frac{\partial^2h/\partial x^2}{\left[1+\left(\partial h/\partial x\right)^2\right]^{3/2}}, \tag{3.7d}$$

$$\frac{1}{\sqrt{1+\left(\partial h/\partial x\right)^2}}\left\{\tau_{xz}\left[1-\left(\frac{\partial h}{\partial x}\right)^2\right]+\tau_{zz}\frac{\partial h}{\partial x}-\tau_{xx}\frac{\partial h}{\partial x}\right\}=-Ma\left(\frac{\partial T}{\partial x}+\frac{\partial h}{\partial x}\frac{\partial T}{\partial z}\right) \quad (3.7e)$$

Moreover, in non-dimensional form, the constitutive equation for the viscoelastic Maxwell fluid becomes

$$\boldsymbol{\tau}+De\frac{\partial\,\boldsymbol{\tau}}{\partial t}=\left[\left(\nabla\boldsymbol{v}\right)+\left(\nabla\boldsymbol{v}\right)^{\mathrm{T}}\right] \quad (3.8)$$

Equations 3.6 – 3.8 formulating the problem in the dimensionless form are characterized by the following set of non-dimensional parameters:

$$Pr=\frac{\mu_o}{\rho\alpha},\ Ga=\frac{\rho g H^3}{\mu_o\alpha},\ Ma=\frac{\sigma_T\vartheta H^2}{\mu_o\alpha},\ Bi=\frac{qH}{\kappa},\ \Sigma=\frac{\sigma H}{\mu_o\alpha},\ De=\frac{\lambda\alpha}{H^2} \quad (3.9)$$

The parameters in Eq. 3.9 are, respectively, the Prandtl number, Galileo number, Marangoni number, Biot number, inverse capillary number, and Deborah number. The Galileo number is a measure of the gravity **g**, while the inverse capillary number takes into account the deformability of the free surface. The Biot number signifies the rate of heat transfer across the free surface, and the Marangoni number governs the present instability phenomenon. The Deborah number represents the dimensionless relaxation time of the viscoelastic fluid. In this analysis, the relaxation time is non-dimensionalized by the diffusive time scale H^2/α, which is also considered as the characteristic time scale for the ongoing investigation.

We now take an effort to estimate the typical values of the non-dimensional parameters involved with this analysis. In the context of a viscoelastic fluid, the permissible range of various dimensional parameters pertinent to the present investigation are as follows [98,106,107]: $H \approx O\,(0.01-1)$ mm, $\lambda \approx O\,(0-10)$ s ($\lambda = 0$ represents the characteristics of a Newtonian fluid), $\mu_o \approx O\,(10^{-3}-10^{-1})$ Pa.s, $\sigma \approx O$ (0.01 - 0.07) $\mathrm{Nm^{-1}}$, $\rho \approx O\,(10^3)$ $\mathrm{kg\,m^{-3}}$ and $\alpha \approx O\,(10^{-7})$ $\mathrm{m^2 s^{-1}}$. This allows us to consider the following wide range of the dimensionless parameters: $O(10^3) \lesssim \Sigma \lesssim O(10^5)$, $0 \lesssim De \lesssim O(1)$, $O(0.1) \lesssim Ga \lesssim O(10^2)$. From the definition of Σ and *Ga*, it is clear that while Σ increases with surface tension (σ), *Ga* gets enhanced with the increment in **g**. Noteworthily, in the limit ($Ga,\ \Sigma) \to \infty$, a free surface can be considered non-deformable, which generally occurs for a liquid with very high surface tension at terrestrial conditions.

It may be mentioned that, for a liquid layer with $H \approx O$ (0.1) mm and $\mu_o \approx O$ (10^{-3}) Pa.s, $Ga \approx 0.1$ refers to the microgravity environment (*i.e.*, g = 0.01 ms^{-2}); whereas Ga = 100 corresponds to the normal gravity conditions. For such a liquid layer, $Pr \approx O(10)$. Moreover, the value of Bi is varied in the range $0 \lesssim Bi \lesssim O(1)$ to explore the all possible instability modes persisting in the system and to understand their behavior.

3.2.3 Base state

The physical problem formulated by Eqs. 3.6-3.8 admits a base solution that corresponds to hydrostatic pressure and linear temperature distribution within the quiescent liquid layer. In dimensionless form, this base state can be represented as

$$\boldsymbol{v}^o = 0, \quad \boldsymbol{\tau}^o = 0, \quad h^o = 1, \quad p^o = Ga(1-z), \quad T^o = 1 - z + Bi^{-1} \tag{3.10}$$

Above a certain critical temperature gradient, owing to the thermocapillary effect, the base state represented by Eq. 3.10 ceases to persist and the Marangoni convection starts appearing in the liquid layer. In the forthcoming sections, we study the stability of this base state of the system against infinitesimal normal perturbations under the framework of linear stability technique.

3.3 Linear Stability Analysis

To study the stability of the system with respect to infinitesimal perturbations, we now introduce the following perturbed fields (denoted by a tilde)

$$\boldsymbol{v} = \boldsymbol{v}^o + \tilde{\boldsymbol{v}}(\tilde{u}, 0, \tilde{w}), \quad \boldsymbol{\tau} = \boldsymbol{\tau}^o + \tilde{\boldsymbol{\tau}}, \quad p = p^o + \tilde{p}, \quad T = T^o + \tilde{\theta}, \quad h = h^o + \tilde{\xi} \tag{3.11}$$

into Eqs. 3.6-3.7, and linearize the same around the base state (Eq. 3.10) which finally yields

$$\nabla \cdot \tilde{\boldsymbol{v}} = 0 \tag{3.12a}$$

$$Pr^{-1} \frac{\partial \tilde{\boldsymbol{v}}}{\partial t} = -\nabla \tilde{p} + \nabla \cdot \tilde{\boldsymbol{\tau}} \tag{3.12b}$$

$$\frac{\partial \tilde{\theta}}{\partial t} = \nabla^2 \tilde{\theta} + \tilde{w} \tag{3.12c}$$

The boundary conditions are now reduced to the following form

$$\text{at } z=0: \qquad \tilde{\boldsymbol{v}}=0,\ \frac{\partial\tilde{\theta}}{\partial z}=0 \tag{3.13a}$$

$$\text{at } z=1: \qquad \frac{\partial\tilde{\xi}}{\partial t}=\tilde{w}, \tag{3.13b}$$

$$\frac{\partial\tilde{\theta}}{\partial z}=-Bi\left(\tilde{\theta}-\tilde{\xi}\right), \tag{3.13c}$$

$$\tilde{\tau}_{xz}=-Ma\frac{\partial}{\partial x}\left(\tilde{\theta}-\tilde{\xi}\right), \tag{3.13d}$$

$$-\tilde{p}+Ga\ \tilde{\xi}+\tilde{\tau}_{zz}=\Sigma\ \frac{\partial^2\tilde{\xi}}{\partial x^2} \tag{3.13e}$$

To eliminate $\tilde{p}$, we formulate this BVP in terms of the disturbance stream function $\tilde{\psi}$. Introducing the stream function relationships $\tilde{u}=\partial\tilde{\psi}/\partial z$, $\tilde{w}=-\partial\tilde{\psi}/\partial x$ and employing the constitutive equation for Maxwell viscoelastic model, we finally arrive at the following set of equations,

$$Pr^{-1}\left(\frac{\partial}{\partial t}\nabla^2\tilde{\psi}+De\frac{\partial^2}{\partial t^2}\nabla^2\tilde{\psi}\right)=\nabla^4\tilde{\psi} \tag{3.14a}$$

$$\frac{\partial\tilde{\theta}}{\partial t}=\nabla^2\tilde{\theta}-\frac{\partial\tilde{\psi}}{\partial x} \tag{3.14b}$$

with boundary conditions,

$$\text{at } z=0: \qquad \tilde{\psi}=0,\ \frac{\partial\tilde{\psi}}{\partial z}=0,\ \frac{\partial\tilde{\theta}}{\partial z}=0 \tag{3.15a}$$

$$\text{at } z=1: \qquad \frac{\partial\tilde{\xi}}{\partial t}=-\frac{\partial\tilde{\psi}}{\partial x}, \tag{3.15b}$$

$$\frac{\partial\tilde{\theta}}{\partial z}=-Bi\left(\tilde{\theta}-\tilde{\xi}\right), \tag{3.15c}$$

$$\frac{\partial^2\tilde{\psi}}{\partial z^2}-\frac{\partial^2\tilde{\psi}}{\partial x^2}=-Ma\frac{\partial}{\partial x}\left(\tilde{\theta}-\tilde{\xi}\right)-Ma\ De\frac{\partial^2}{\partial t\,\partial x}\left(\tilde{\theta}-\tilde{\xi}\right), \tag{3.15d}$$

$$\left(1+De\frac{\partial}{\partial t}\right)\left(\tilde{p}-Ga\ \tilde{\xi}+\Sigma\ \frac{\partial^2\tilde{\xi}}{\partial x^2}\right)=-2\frac{\partial^2\tilde{\psi}}{\partial x\,\partial z} \tag{3.15e}$$

We analyze the arbitrary perturbations in terms of the following normal modes

$$\begin{bmatrix} \tilde{\psi}(x,z,t) \\ \tilde{\theta}(x,z,t) \\ \tilde{\xi}(x,z,t) \end{bmatrix} = \begin{bmatrix} \hat{\psi}(z) \\ \hat{\theta}(z) \\ \hat{\xi}(z) \end{bmatrix} \exp\left(i\,k\,x - \lambda\,t\right) \tag{3.16}$$

where $\hat{\psi}$, $\hat{\theta}$ and $\hat{\xi}$ are the amplitude of the corresponding normal modes. Moreover, k denotes the disturbance wave number (a real quantity) and $\lambda = \lambda_r + i\omega$ refers to the decay rate. The parameter ω represents the frequency of perturbation. It is important to note that, $\lambda_r < 0$ describes an unstable system for which the disturbances grow in time. On the other hand, the disturbances get damped for $\lambda_r > 0$ yielding a stable system. Employing the normal mode form of perturbations, we now obtain the following set of equations:

$$Pr\frac{d^4\hat{\psi}}{dz^4} - \left(\lambda^2 De - \lambda + 2Pr\,k^2\right)\frac{d^2\hat{\psi}}{dz^2} + \left(\lambda^2 De - \lambda + Pr\,k^2\right)k^2\hat{\psi} = 0 \tag{3.17a}$$

$$\frac{d^2\hat{\theta}}{dz^2} + \left(\lambda - k^2\right)\hat{\theta} = i\,k\,\hat{\psi} \tag{3.17b}$$

The boundary conditions read

at $z = 0$: $$\hat{\psi} = 0,\ \frac{d\hat{\psi}}{dz} = 0,\ \frac{d\hat{\theta}}{dz} = 0 \tag{3.18a}$$

at $z = 1$: $$i\,k\,\hat{\psi} = \lambda\hat{\xi}, \tag{3.18b}$$

$$\frac{d\hat{\theta}}{dz} = -Bi\left(\hat{\theta} - \hat{\xi}\right), \tag{3.18c}$$

$$\frac{d^2\hat{\psi}}{dz^2} + k^2\hat{\psi} = i\,Ma\,k\left(\lambda De - 1\right)\left(\hat{\theta} - \hat{\xi}\right), \tag{3.18d}$$

$$Pr\frac{d^3\hat{\psi}}{dz^3} + \left(\lambda - \lambda^2 De - 3Pr\,k^2\right)\frac{d\hat{\psi}}{dz} = i\,k\,Pr\left(1 - \lambda De\right)\left(Ga + \Sigma k^2\right)\hat{\xi} \tag{3.18e}$$

Equations 3.17 – 3.18 constitute a linear eigenvalue system for the present problem with λ and Ma as the eigenvalues. Solving it for $\lambda_r = 0$, we can now obtain the neutral stability curves that demarcate the stable region from the unstable one. However, due to its complex nature, this eigenvalue problem cannot be solved analytically. We thus solve it numerically using the Runge-Kutta method with shooting technique [108]. In doing so, we check the accuracy of our numerical procedure by reproducing the results

reported in the literature. In Fig. 3.2, we have compared our results with the results of Pearson [11]. An excellent quantitative agreement with the results of the above-cited paper supports the accuracy of the present numerical implementation.

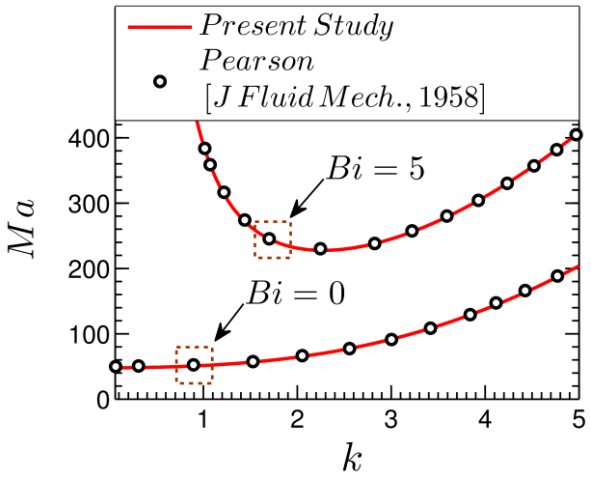

Figure 3.2: Neutral stability curves for a Newtonian liquid layer confined between a horizontal substrate of low thermal conductivity and a non-deformable free surface. The results obtained from the present study (shown by solid lines) are compared with the results of Pearson [11] (shown by marker 'o') for two different *Bi* (0 and 5 respectively). To mimic the characteristics of a non-deformable free surface, here we consider $(Ga, \Sigma) = (10^2, 10^6)$.

3.3.1 Monotonic mode

We first study the monotonic instability mode (*i.e.*, the stationary convection). At the monotonic instability threshold, λ vanishes. Therefore, the substitution of $\lambda = 0$ in Eqs. 3.17-3.18 yields the neutral stability curve for this instability mode.

3.3.2 Oscillatory mode

At the oscillatory instability threshold, λ attains a purely imaginary value, *i.e.*, $\lambda = i\omega$ $(\omega > 0)$. On solving the present eigenvalue problem for such λ, we obtain *Ma* in complex form. However, to have a physical meaning, *Ma* must be a real quantity. Hence, we numerically search such value of λ for which the imaginary part of *Ma* vanishes. For the parameter set (*k*, *Pr*, *Bi*, *Ga*, Σ, *De*), if such a λ exists, then only we get an oscillatory mode of instability. Otherwise, the instability appears in the form of stationary convection. The value of λ for which *Ma* becomes real, is called the perturbation

frequency (ω) for the corresponding *k*. It is worth mentioning here that the repetition of this procedure for different values of *k* gives us the neutral stability curve for oscillatory instability mode. Such stability curves for both the monotonic and oscillatory instability modes are presented in Fig. 3.3.

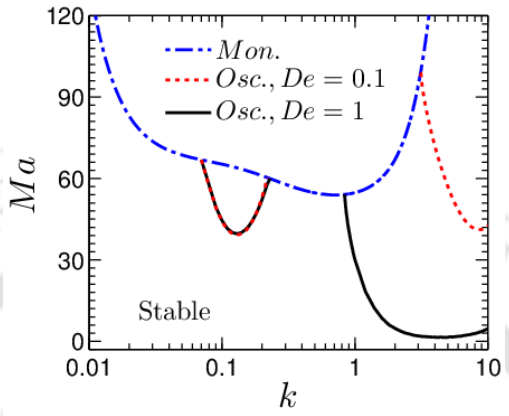

Figure 3.3: Variation of the monotonic (*mon.*: dashed-dotted line) and oscillatory (*osc.*: solid and dotted lines) instability threshold for a viscoelastic liquid layer for $(Ga,\Sigma)=(0.1,10^3)$, $Bi=0.1$, $Pr=10$ and various values of Deborah number, *De*. The domain of stability is situated below the lines. For the long-wave oscillatory mode $Ma_c|_{\mathrm{De}=0.1}=39.15$, $Ma_c|_{\mathrm{De}=1}=39.6$; while for the short-wave oscillatory mode $Ma_c|_{\mathrm{De}=0.1}=42$, $Ma_c|_{\mathrm{De}=1}=2$.

It is important to note that, the value of parameters (Ga, Σ, Bi) considered in this plotting refers to a liquid layer with a deformable free surface having poorly conducting boundaries. Figure 3.3 shows that the monotonic instability threshold is not affected by the elastic behavior of the fluid. However, the magnitude of *De* significantly influences the oscillatory instability margin. It is clear that for both the monotonic and oscillatory instability modes, there exists a minimum value of *Ma* only above which the instability first sets in the liquid layer. We call this *Ma* as the critical Marangoni number (Ma_c), and the corresponding *k* and ω as the critical wavenumber (k_c) and critical frequency (ω_c) respectively. The instability mode with the minimum Ma_c for the entire range of *k* is called the critical mode and becomes the dominant instability mode in the system for the considered set of parameters. Figure 3.3 further reveals that depending on the range of the model parameters, both the long-wave $(k_c \to 0)$ and short-wave $(k_c \approx O(1))$

Marangoni instability can emerge in the present system. The long-wave (oscillatory) mode is critical for $De = 0.1$, whereas, the short-wave (oscillatory) mode gets critical at $De = 1$. In what follows, we investigate both these instability modes separately in a systematic manner.

3.4 Long-wave Instability

It is ensured from Section 3.3 that a long-wave instability can emerge in the present system at least for typical values of the physical parameters. Here, we investigate this instability mode using the lubrication theory and derive an analytical expression for the neutral stability curve. We will also demonstrate that, for small values of k ($<<1$), this analysis accurately reproduces the (numerical) results obtained in Section 3.3.

It was mentioned in Chapter 2 that, to analyze the long-wave Marangoni instability in a Newtonian liquid film, there exist two different characteristic wavenumber scales *i.e.*, $k \sim Bi^{1/4}$ and $k \sim Bi^{1/2}$ [102–104]. However, no such scaling law for a viscoelastic fluid is available in the literature, since the existence of long-wave instability for such a fluid layer has not been detected earlier. At this juncture, it is worth to emphasize that under certain situations as mentioned by Podolny *et al*. [104], the scaling $k \sim Bi^{1/4}$ becomes insufficient, for which the critical perturbations are materialized at $k \sim Bi^{1/2}$. On account of this, we use the later relationship in this analysis. The results obtained with this scaling agrees well with the numerical results, as discussed in the forthcoming sections.

3.4.1 Lubrication approximation

In order to analyze the large-scale evolution of the long-wave Marangoni convection, we rescale the spatial coordinates and time in the following manner

$$X = \varepsilon\, x, \quad Z = z, \quad \mathcal{T} = \varepsilon^2\, t \tag{3.19}$$

where ε $(0 < \varepsilon << 1)$ is a small parameter and can be thought of as the ratio of thickness of the film to its longitudinal length scale. This allows us to write

$$u = \varepsilon\, U, \; w = \varepsilon^2\, W, \; \tau_{xx} = \varepsilon^2\, \breve{\tau}_{XX}, \; \tau_{zz} = \varepsilon^2\, \breve{\tau}_{ZZ}, \; \tau_{xz} = \varepsilon\, \breve{\tau}_{XZ} \tag{3.20}$$

We now expand all the dependent variables of the present problem into a power

series of ε as follows

$$U = U_0 + \varepsilon^2 U_1 + \ldots\ , \qquad W = W_0 + \varepsilon^2 W_1 + \ldots\ , \tag{3.21a}$$

$$p = p_0 + \varepsilon^2 p_1 + \ldots\ , \qquad T = T_0 - z + Bi^{-1} + \varepsilon^2 T_1 + \ldots\ , \tag{3.21b}$$

$$\breve{\tau}_{xx} = \breve{\tau}_{0,\,xx} + \varepsilon^2 \breve{\tau}_{1,\,xx} + \ldots\ ,\ \breve{\tau}_{xz} = \breve{\tau}_{0,\,xz} + \varepsilon^2 \breve{\tau}_{1,\,xz} + \ldots\ ,\ \breve{\tau}_{zz} = \breve{\tau}_{0,\,zz} + \varepsilon^2 \breve{\tau}_{1,\,zz} + \ldots \tag{3.21c}$$

Direct comparison between Eq. 3.21(*b*) and 3.10 reveals that the base state of the system corresponds to $p_0 = p^o$ and $T_0 = 1$. Finally, for this long-wave analysis, we rescale the non-dimensional parameters Bi, De and Σ as:

$$Bi = \varepsilon^2 b\,, \quad De = \varepsilon^{-2} \mathcal{D}e\,, \quad \Sigma = \varepsilon^{-2} c \tag{3.22}$$

This scaling suggests that the present analysis holds good only for small values of Bi and large Σ and De. Here, the scaling of the Deborah number is essential to incorporate the effect of viscoelasticity and to make this analysis mathematically consistent. Due to the weak dependence of the stability threshold on the magnitude of De within this long-wave regime (apparent from Fig. 3.3), the results of the long-wave analysis consistently reproduce the numerical results even for $De \approx O(0.1)$ as will be demonstrated in Section 3.5. The domain of applicability of this long-wave analysis with respect to the other scaled parameters *i.e.*, Bi and Σ will also be discussed therein.

Now, substituting these expansions and the rescaled parameters into the system of governing equations and the boundary conditions *i.e.*, Eqs. 3.6-3.8, and collecting the terms with identical powers of ε, we obtain in the zeroth-order

$$\frac{\partial W_0}{\partial Z} = -\nabla U_0\,, \qquad \frac{\partial p_0}{\partial Z} = -Ga \tag{3.23a}$$

$$\frac{\partial^2 U_0}{\partial Z^2} = \nabla p_0 + \mathcal{D}e \frac{\partial \nabla p_0}{\partial \mathcal{T}}\,, \qquad \frac{\partial^2 T_0}{\partial Z^2} = 0 \tag{3.23b}$$

with the boundary conditions being

$$\text{at } Z = 0: \qquad U_0 = W_0 = 0\,, \quad \frac{\partial T_0}{\partial Z} = 0 \tag{3.24a}$$

$$\text{at } Z = h: \qquad W_0 = \frac{\partial h}{\partial \mathcal{T}} + U_0\, \nabla h\,, \quad \frac{\partial T_0}{\partial Z} = 0 \tag{3.24b}$$

$$c\,\nabla^2 h = -p_0\,, \qquad U_{0\,Z} = -Ma\,\nabla\left(T_0 - h\right) - Ma\,\mathcal{D}e\,\frac{\partial}{\partial \mathcal{T}}\nabla\left(T_0 - h\right) \tag{3.24c}$$

In Eqs. 3.23-3.24 and thus hereafter, $\nabla \equiv \left(\partial/\partial X\,, 0, 0\right)$. The solution to this BVP is given by

$$p_0 = \chi\left(X, \mathcal{T}\right) - GaZ\,, \qquad T_0 = \Theta\left(X, \mathcal{T}\right) \tag{3.25a}$$

$$U_0 = \frac{1}{2}Z\left(Z - 2h\right)\nabla\left(\chi + \mathcal{D}e\,\frac{\partial \chi}{\partial \mathcal{T}}\right) - Ma\;Z\;\nabla\left(\gamma + \mathcal{D}e\,\frac{\partial \gamma}{\partial \mathcal{T}}\right) \tag{3.25b}$$

$$W_0 = \frac{1}{2}Z^2\;\nabla\left[\frac{1}{3}\left(3h - Z\right)\nabla\left(\chi + \mathcal{D}e\,\frac{\partial \chi}{\partial \mathcal{T}}\right) + Ma\;\nabla\left(\gamma + \mathcal{D}e\,\frac{\partial \gamma}{\partial \mathcal{T}}\right)\right] \tag{3.25c}$$

where $\chi = Ga\;h - c\,\nabla^2 h$ and $\gamma = \Theta - h$.

Here also, the base state corresponds to a quiescent liquid layer with a uniform transverse temperature gradient, represented by,

$$h = 1, \qquad \Theta = 1 \tag{3.26}$$

3.4.2 Amplitude equations

We now derive a closed set of amplitude equations that govern the spatiotemporal dynamics of the long-wave perturbations. To obtain the first amplitude equation, we use the condition $\dfrac{\partial h}{\partial \mathcal{T}} = -\nabla\int_0^h U_0\;dZ$ that yields

$$\frac{\partial h}{\partial \mathcal{T}} = \nabla\left[\frac{1}{3}h^3\;\nabla\left(\chi + \mathcal{D}e\,\frac{\partial \chi}{\partial \mathcal{T}}\right) + \frac{1}{2}Ma\;h^2\;\nabla\left(\gamma + \mathcal{D}e\,\frac{\partial \gamma}{\partial \mathcal{T}}\right)\right] \tag{3.27}$$

Equation 3.27 depicts the evolution of liquid layer thickness. The first term on the right-hand side of Eq. 3.27 takes into account the effect of gravity and surface tension on the deformation of the free surface, while the second term represents the influence of the thermocapillary flow on the fluid layer thickness.

We obtain the second amplitude equation by considering up to the first order of the expansion of energy equation. This yield

$$\frac{\partial^2 T_1}{\partial Z^2} = \frac{\partial \Theta}{\partial \mathcal{T}} + U_0\;\nabla\Theta - \nabla^2\;\Theta - W_0 \tag{3.28}$$

$$\text{at } Z=0: \qquad \frac{\partial T_1}{\partial Z}=0 \tag{3.29a}$$

$$\text{at } Z=1: \qquad \frac{\partial T_1}{\partial Z}=\nabla h\,\nabla\Theta-\left(\nabla h\right)^2-b\,\gamma \tag{3.29b}$$

Integrating Eq. 3.28 across the liquid layer and accounting the boundary conditions 3.29(*a*-*b*), we get the second amplitude equation as written below:

$$\begin{aligned} h\frac{\partial\Theta}{\partial\mathcal{T}}=\nabla\left(h\nabla\Theta\right)+\left[\frac{1}{3}h^3\,\nabla\left(\chi+\mathcal{D}e\frac{\partial\chi}{\partial\mathcal{T}}\right)+\frac{1}{2}Ma\,h^2\,\nabla\left(\gamma+\mathcal{D}e\frac{\partial\gamma}{\partial\mathcal{T}}\right)\right]\nabla\gamma \\ +\nabla\left[\frac{1}{8}h^4\,\nabla\left(\chi+\mathcal{D}e\frac{\partial\chi}{\partial\mathcal{T}}\right)+\frac{1}{6}Ma\,h^3\,\nabla\left(\gamma+\mathcal{D}e\frac{\partial\gamma}{\partial\mathcal{T}}\right)\right]-\left(\nabla h\right)^2-b\gamma \end{aligned} \tag{3.30}$$

Equation 3.30 describes the evolution of the liquid layer temperature (averaged across the layer). The first term of Eq. 3.30 takes into account the conductive heat transfer in the longitudinal direction, the second and third term account for the advective heat transfer (by the flow), and the remaining terms represent the heat loss from the free surface.

3.4.3 Dispersion relation

The amplitude equations 3.27 and 3.30 derived in Section 3.4.2 are nonlinear in h and Θ. We now linearize both these equations for infinitesimal perturbations around the base state. Substituting the perturbed fields $h=1+\zeta$, $\Theta=1+\phi$ into Eqs. 3.27 and 3.30, and linearizing the same, we finally arrive at

$$\frac{\partial\zeta}{\partial\mathcal{T}}=\nabla^2\left[\frac{1}{3}\left(\aleph+\mathcal{D}e\frac{\partial\aleph}{\partial\mathcal{T}}\right)+\frac{1}{2}Ma\left(\vartheta+\mathcal{D}e\frac{\partial\vartheta}{\partial\mathcal{T}}\right)\right] \tag{3.31a}$$

$$\frac{\partial\phi}{\partial\mathcal{T}}=\nabla^2\left[\frac{1}{8}\left(\aleph+\mathcal{D}e\frac{\partial\aleph}{\partial\mathcal{T}}\right)+\frac{1}{6}Ma\left(\vartheta+\mathcal{D}e\frac{\partial\Re}{\partial\mathcal{T}}\right)+\phi\right]-b\,\Re \tag{3.31b}$$

where $\aleph=Ga\zeta-c\nabla^2\zeta$ and $\Re=\phi-\zeta$.

Assuming the normal form for the perturbations

$$\begin{bmatrix}\zeta(X,\mathcal{T})\\ \phi(X,\mathcal{T})\end{bmatrix}=\begin{bmatrix}\tilde{\zeta}\\ \tilde{\phi}\end{bmatrix}\exp\left(i\,K\,X+\lambda\,\mathcal{T}\right) \tag{3.32}$$

yields the following dispersion relation which dictates the variation of the disturbance growth rate, λ with dimensionless wave number K.

$$\lambda^2\left[48(\Omega-3)+\Lambda\mathcal{D}e\,K^2(\Omega-48)\right]+24\lambda\left[2\,Ma\,K^2+3(\,\Omega\,K^2-2K^2-2b)\right]$$
$$+2\lambda\,\Lambda\,K^2\left[\Omega-24\left(1+\mathcal{D}e\,K^2+\mathcal{D}e\,b\right)\right]+Ma\,K^4(72+\Lambda)-48\Lambda\,K^2\left(b+K^2\right)=0 \tag{3.33}$$

here $\Lambda = Ga + cK^2$ and $\Omega = Ma\,\mathcal{D}e\,K^2$.

Equation 3.33 suggests the appearance of two different long-wave instabilities in the system; namely, the monotonic mode (for $\lambda = 0$) and the oscillatory mode (for $\lambda = i\omega$). In what follows, we analyze both these modes separately and derive analytical expressions governing the stability threshold of the system for each mode.

3.4.3.1 *Monotonic mode*

We first start with the case of monotonic instability. Substituting $\lambda = 0$ in Eq. 3.33, we find the neutral stability curve for the monotonic mode. This is given by,

$$Ma_{mon.} = \frac{48\left(b+K^2\right)\left(Ga+cK^2\right)}{K^2\left(72+Ga+cK^2\right)} \tag{3.34}$$

In terms of the unscaled parameters *viz.*, $k = \varepsilon K$, $Bi = \varepsilon^2 b$ and $\Sigma = \varepsilon^{-2} c$; Eq. 3.34 turns

$$Ma_{mon.} = \frac{48\left(Bi+k^2\right)\left(Ga+\Sigma\,k^2\right)}{k^2\left(72+Ga+\Sigma\,k^2\right)} \tag{3.35}$$

It can be seen from Eq. 3.35 that the monotonic instability threshold is independent of the viscoelastic parameter *De*. This complies with the numerical results presented in Section 3.3. In fact, the existing literature on Marangoni instability in a viscoelastic fluid layer also supports this characteristic [71–73].

3.4.3.2 *Oscillatory mode*

The neutral stability curve governing the oscillatory instability threshold is given by the relationship

$$Ma_{osc.} = \frac{72\left(b+K^2\right)+24K^2\left(Ga+cK^2\right)\left(1+\mathcal{D}e\,b+\mathcal{D}e\,K^2\right)}{12\,K^2\left(2+3\mathcal{D}e\,K^2\right)+\mathcal{D}e\,K^4\left(Ga+cK^2\right)} \tag{3.36}$$

Recasting Eq. 3.36 in terms of the unscaled fields $k = \varepsilon K$, $Bi = \varepsilon^2 b$, $De = \varepsilon^{-2}\mathcal{D}e$ and $\Sigma = \varepsilon^{-2} c$; we obtain

$$Ma_{osc.} = \frac{72\left(Bi+k^2\right)+24\,k^2\left(Ga+\Sigma\,k^2\right)\left(1+De\,Bi+De\,k^2\right)}{12k^2\left(2+3De\,k^2\right)+De\,k^4\left(Ga+\Sigma\,k^2\right)} \tag{3.37}$$

Furthermore, the oscillation frequency of the neutral perturbations for this long-wave oscillatory mode is given by,

$$\omega = k^{2}\sqrt{\frac{\left(72+Ga+\Sigma k^{2}\right)\left(Ma_{mon.}-Ma_{osc.}\right)}{48\left[3+De\,k^{2}\left(Ga+\Sigma k^{2}\right)\right]-Ma_{osc.}De\,k^{2}\left[48+De\,k^{2}\left(Ga+\Sigma k^{2}\right)\right]}} \qquad (3.38)$$

The neutral stability curves for both the long-wave monotonic and oscillatory instability modes are demonstrated in Fig. 3.4. Moreover, a comparison between the outcome of long-wave theory with the numerical results is also presented in Fig. 3.4(*a*). A closer look at Fig. 3.4(*a*) reveals that for small values of *k*, both the results agree in a good quantitative manner for each instability mode. In particular, the critical Marangoni number (Ma_c) and the wave number (k_c) are nicely captured by the long-wave analysis for both the monotonic and oscillatory modes as witnessed in Fig. 3.4(*a*).

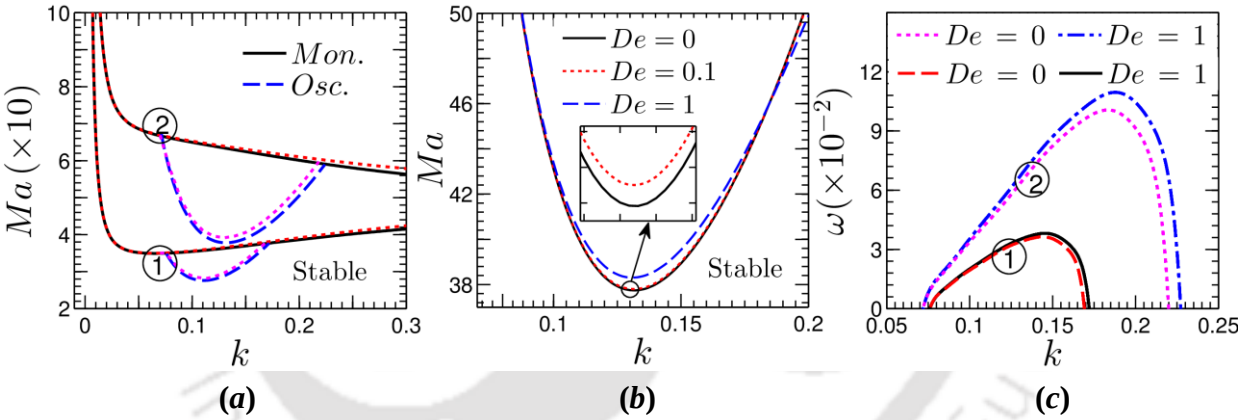

Figure 3.4: (*a*) Neutral stability curves for the long-wave monotonic (*mon.*: solid lines) and oscillatory (*osc.*: dashed lines) modes of instability at $(Ga,\Sigma)=(0.1,10^3)$ and $De=0.1$. The solid and dashed lines represent the result of the asymptotic analysis, while the dotted lines represent the numerical result. (*b*) Variation of the stability threshold for the long-wave oscillatory mode with *De* at $Bi=0.1$, $(Ga,\Sigma)=(0.1,10^3)$ (inset shows the zoomed-in view of the neutral curves for *De* = 0 and 0.1 respectively). (c) Variation of the growth rate of neutral perturbations for *De* = 0 (dashed and dotted lines) and *De* = 1 (dashed-dot and solid lines) at $(Ga,\Sigma)=(0.1,10^3)$. In panels (*a*) and (*c*) lines marked by 1 and 2 correspond to $Bi=0.05$ and $Bi=0.1$ respectively.

It is important to note that the magnitude of parameters *Ga* and Σ considered in plotting Fig. 3.4(*a*) refers to a liquid layer with a deformable free surface. For both the

considered values of *Bi*, there exists a local minimum[1] in the neutral stability curve for oscillatory mode within the long-wavelength limit. However, for the monotonic mode, although such a minimum appears for $Bi = 0.05$, no minimum point is observed for $Bi = 0.1$ within the long-wave regime. This is because, the long-wave theory suggests a minimum in the neutral stability curves (for monotonic mode) within finite values of *k* only for $Bi\,\Sigma < 72$. The critical Marangoni number and the wave number at this point are given by

$$Ma_{c,mon.} = \frac{48\left[\Pi + Bi\,\Sigma\left(72 - Bi\,\Sigma\right)\right]\left[\Pi + Ga\left(72 - Bi\,\Sigma\right)\right]}{\Pi\left[\Pi + \left(72 - Bi\,\Sigma\right)\left(72 + Ga\right)\right]} \tag{3.39}$$

$$k_{c,mon.} = \sqrt{\frac{\Pi}{\Sigma\left(72 - Bi\,\Sigma\right)}} \tag{3.40}$$

respectively, where $\Pi = Bi\,\Sigma Ga\left[1 + \sqrt{1 + \left\{\left(72 - Bi\,\Sigma\right)\left(72 + Ga\right)/Bi\,\Sigma Ga\right\}}\right]$

On the other hand, for $Bi\,\Sigma > 72$, the long-wave theory predicts a minimum in the neutral curve at the limit $k \to \infty$ (*i.e.*, in the short-wave regime) with $Ma_{c,\,mon.} = 48$.

The parameters $Ma_{c,osc.}$, $k_{c,osc.}$ and $\omega_{c,osc.}$ governing the local minimum of long-wave oscillatory mode can also be estimated from Eq. 3.37. However, the final expression in this case is too convoluted and lengthy, and hence, for the conciseness in presentation, we have not presented it here. The procedure for evaluating these parameters is discussed in Appendix B of this thesis.

Figure 3.4(*a*) further reveals that Ma_c increases with *Bi* for both the long-wave instability modes. This observation indicates an enhancement in the stability of the system for higher values of Biot number. The increased heat transfer rate from the free liquid surface enhances the stability of the system for higher values of *Bi*. A detailed discussion on the variation of Ma_c and k_c with *Bi* for both the monotonic and oscillatory modes is presented later in the context of the discussion of Fig. 3.6.

[1] *We call it a local minimum because there can be another minimum point in the neutral curve within the shortwave regime as shown in Fig. 3.3. We will demonstrate below that depending on the magnitude of physical parameters, either of this local minima can become the global minimum.*

Figure 3.4(*b*) demonstrates the variation in long-wave (oscillatory) instability threshold with the Deborah number. Clearly, the increasing magnitude of *De* enhances the stability of the system (although very mild) in the long-wave regime. This phenomenon may be interpreted as: for higher values of *De*, owing to the pronounced elastic behavior, the fluid resists large-scale deformations. This enhances the stability of the system for higher values of *De* within the long-wave regime.

For the long-wave oscillatory mode, the variation in the frequency of neutral perturbations (ω) with disturbance wave number is demonstrated in Fig. 3.4(*c*). It is found that, compared to a Newtonian fluid, ω is marginally higher for a viscoelastic fluid. Moreover, with the increment in *Bi*, ω increases for both the Newtonian and viscoelastic fluids.

3.5 Short-wave Instability

The long-wave analysis presented in Section 3.4 remains accurate only for small wave number. Hence, we now extend this analysis for sufficiently large (but finite) values of *k*. Solving the linear BVP formulated by Eqs. 3.17-3.18 numerically (following the procedure mentioned in Section 3.3) within all permissible range of the model parameters, we obtain the neutral stability curves governing the monotonic and oscillatory instability thresholds for the present system.

It is worth mentioning here that the numerical results demonstrate no substantial deviation in the stability margin with Prandtl number for both the instability modes. This is also apparent from the previous section where the neutral curves are found to be independent of *Pr* (Eqs. 3.35 and 3.37). For this reason, we fix $Pr = 10$ in all the graphical results.

The typical neutral stability curves for both the monotonic and oscillatory instability modes are demonstrated in Figs. 3.5(*a*–*b*) for different combinations of *Bi* and *De*. The values of *Ga* and Σ considered in this plotting refers to a deformable free surface.

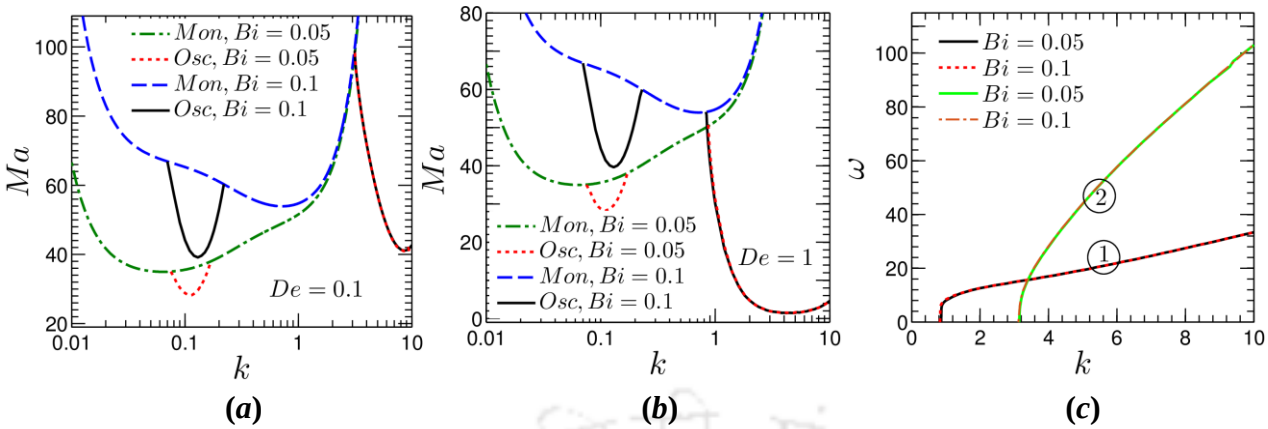

Figure 3.5: Variation of the stability threshold with Biot number for $(Ga, \Sigma) = (0.1, 10^3)$ and $Pr = 10$. Panels (*a*) and (*b*) display the neutral stability curves for monotonic (*mon.*: dashed and dashed-dotted lines) and oscillatory (*osc.*: solid and dotted lines) modes for $De = 0.1$ and 1 respectively. Panel (*c*) displays the variation of the frequency of neutral perturbations for $Bi = 0.05$ (solid lines) and $Bi = 0.1$ (dotted and dashed-dotted lines). Lines marked by 1 and 2 in panel (*c*) correspond to $De = 1$ and 0.1 respectively. Domains of stability are situated below the lines.

Figures 3.5(*a*–*b*) shows that, for viscoelastic fluids, apart from the long-wave oscillatory mode, a different oscillatory instability can emerge in the system for higher values of *k*. We call this the *short-wave oscillatory* mode. It is worth mentioning here that this short-wave oscillatory mode is a characteristic of viscoelastic fluids only, as no such instability mode is detected for a Newtonian liquid layer (*i.e.*, *De* = 0). Therefore, this is purely an outcome of the elastic behavior of the liquid.

Interestingly Fig. 3.5 further reveals that the behavior of the system for short-wave disturbances is quite different from the long-wave disturbances. One can observe that, for small *k* (*i.e.*, within the long-wave regime), an increase in the magnitude of *Bi* leads to a well-pronounced stabilization of the system for both the monotonic and oscillatory modes. On the other hand, this dependency of the stability threshold on *Bi* vanishes in the short-wave regime; and the neutral curves for different *Bi* collapse into a single curve. However, the elastic behavior of the fluid has a marked influence on the stability threshold inside this regime, making the system more unstable towards the short-wave oscillatory mode for higher values of *De*. This is in stark contrast to the long-wave regime, for which the system stability was found to be increased with increasing degree of elasticity of the fluid [Fig. 3.4(*b*)]. It should be mentioned here that, for large *De*, the enhanced elasticity of the fluid makes it an appropriate medium to sustain the oscillatory

wave-like motion. Primarily, for this reason, the short-wave oscillatory mode becomes the dominant instability mode in the system for higher values of *De*.

The variation of the oscillation frequency of neutral perturbations for the short-wave oscillatory mode is presented in Fig. 3.5(*c*). Clearly, ω reduces with increasing *De*. However, in contrast to the long-wave oscillatory mode [Fig. 3.4(*c*)], ω for the short-wave oscillatory mode apparently remains independent of *Bi*.

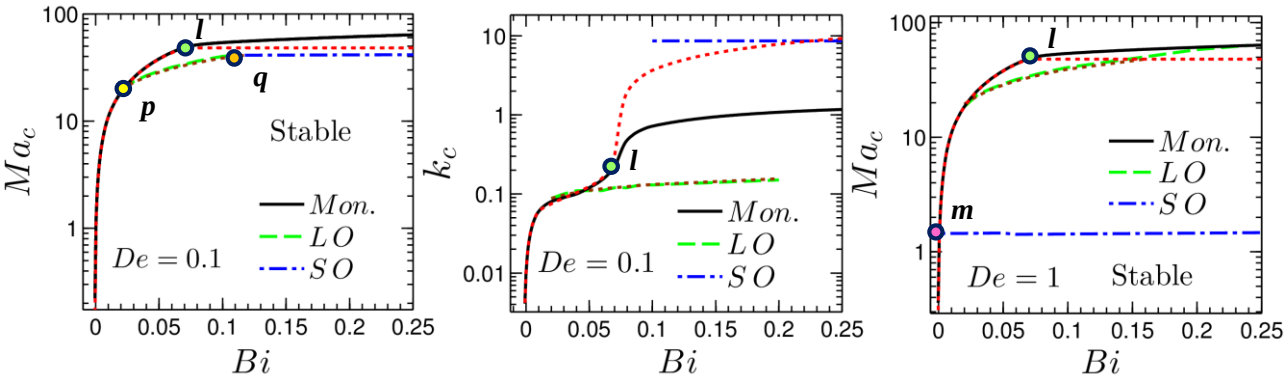

Figure 3.6: Variation of the critical Marangoni number (*a*) and (*c*), and critical wave number (*b*) with *Bi* at $(Ga, \Sigma) = (0.1, 10^3)$ and $Pr = 10$. Panels (*a*, *b*) and (*c*) represent the variations for $De = 0.1$ and 1 respectively. The solid line corresponds to the monotonic (*mon.*) mode, dashed one to the long-wave oscillatory (LO) mode and the dashed-dotted line represents the variation for the short-wave oscillatory (SO) mode. For each long-wave instability mode, the results of the asymptotic analysis (represented by dotted lines) are juxtaposed with the corresponding numerical results in each panel.

The variation of the critical Marangoni number Ma_c and the corresponding wavenumber k_c with *Bi* is presented in Fig. 3.6 for a liquid layer with a deformable free surface. A comparison is also made here between the results of long-wave analysis with the numerical computation. It is observed that, for the long-wave oscillatory mode, Ma_c and k_c predicted by the long-wave theory agrees well with the numerical results within the entire range of *Bi*. However, for the monotonic mode, both the results agree in a quantitative manner only up to *Bi* = 0.072 (point ***l*** in Fig. 3.6) corresponding to $Bi\,\Sigma \le 72$ predicted by the long-wave theory. This is true for all *De* since the monotonic instability threshold does not vary with the same. However, for $Bi\,\Sigma > 72$, as can be seen from Fig. 3.6(*b*), the critical wave number predicted by the long-wave theory grows rapidly for the

monotonic mode tending to infinity. This limits the domain of applicability of the long-wave approximation for the monotonic mode only up to $Bi\,\Sigma \le 72$. For $Bi\,\Sigma > 72$, the numerical results indicate a mild increase in Ma_c for the monotonic instability mode with $k_c \sim 1$. This suggests the appearance of a short-wave monotonic mode in the system for higher values of *Bi* and Σ.

Figure 3.6 further demonstrates that depending on the magnitude of *Bi*, the dominant instability mode can vary within the system. For *De* = 0.1, Fig. 3.6(*a*) reveals that at small *Bi*, instability appears in the form of stationary convection. However, with the increment in *Bi*, first, a long-wave oscillatory instability prevails in the liquid layer which then switches into the short-wave oscillatory mode with further increment in *Bi*. Hence, depending on the magnitude of *Bi*, a competition between the long-wave monotonic – long-wave oscillatory [point ***p*** in Fig. 3.6(*a*)] and long-wave oscillatory – short-wave oscillatory mode (point ***q***) can occur in the system.

However, with the increment in *De*, the competition primarily takes place between the monotonic and short-wave oscillatory mode [point ***m*** in Fig. 3.6(*c*)]. For this case, the monotonic mode is critical at $Bi = 0$, whereas the short-wave oscillatory mode gets dominant for $Bi > 0$. A detailed discussion on the variation of instability modes with the magnitude of *De* and *Bi* for both the case of deformable and non-deformable free surface is presented later in the context of Fig. 3.9.

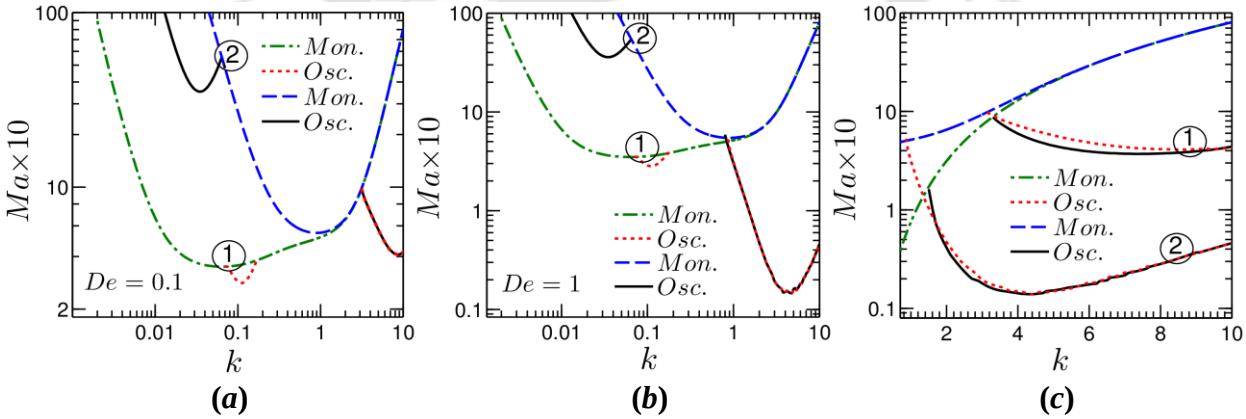

Figure 3.7: Variation of the stability margin for the monotonic (*mon.*: dashed-dotted and dashed lines) and oscillatory (*osc.*: dotted and solid lines) instability modes for different values of *De*, *Ga* and Σ at $Pr = 10$. Panel (*a*) corresponds to *De* = 0.1, panel (*b*) corresponds to $De = 1$, panel (*c*) corresponds to $Ga = 0.1$. In panels (*a*, *b*), the lines marked by 1 and 2 correspond to $(Ga, \Sigma) = (0.1, 10^3)$ and $(Ga, \Sigma) = (10^2, 10^5)$

respectively. For panel (*c*), the dashed and dotted lines correspond to $\Sigma = 10^3$, while the dashed-dotted and solid lines correspond to $\Sigma = 10$. Here, the lines marked by 1 and 2 correspond to $De = 0.1$ and $De = 1$ respectively.

The effect of deformability of the free surface on the onset of instability in the system is demonstrated in Fig. 3.7. From panels ($a-b$) it is evident that, within the long-wave regime, the stability threshold for both the monotonic and oscillatory modes is significantly affected by the deformability of the free surface. An enhanced dampening of the free surface deflection for higher values of *Ga* and Σ substantially increases the stability of the system within this regime. However, in stark contrast to this observation, the marginal stability curve for the short-wave regime remains apparently unaffected of the free surface deformations, within which the stability threshold is primarily governed by the viscoelasticity of the fluid [shown in Fig. 3.7(*c*)].

Interestingly, a comparison between Figs. 3.7 (*a*–*b*) reveals that, while a long-wave oscillatory instability sets in a liquid layer with a deformable free surface at *De* = 0.1, the short-wave oscillatory mode becomes dominant for the same surface at *De* = 1. It is therefore evident that there must exist a critical Deborah number for which competition between the long-wave and short-wave oscillatory mode takes place in the system. On the other hand, no such competition between the respective instability modes occurs for a non-deformable free surface, at least for the considered values of *De*. We discuss this issue in details in Fig. 3.8 for a wide range of *De*.

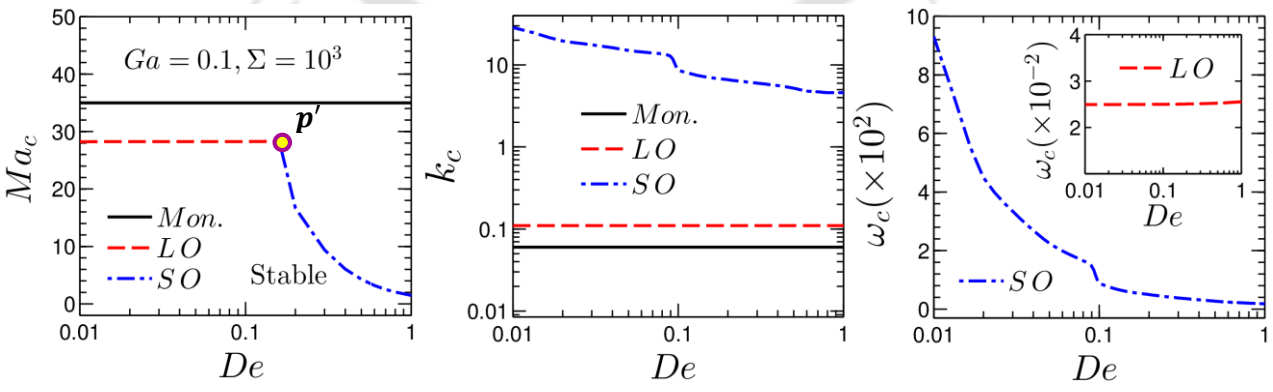

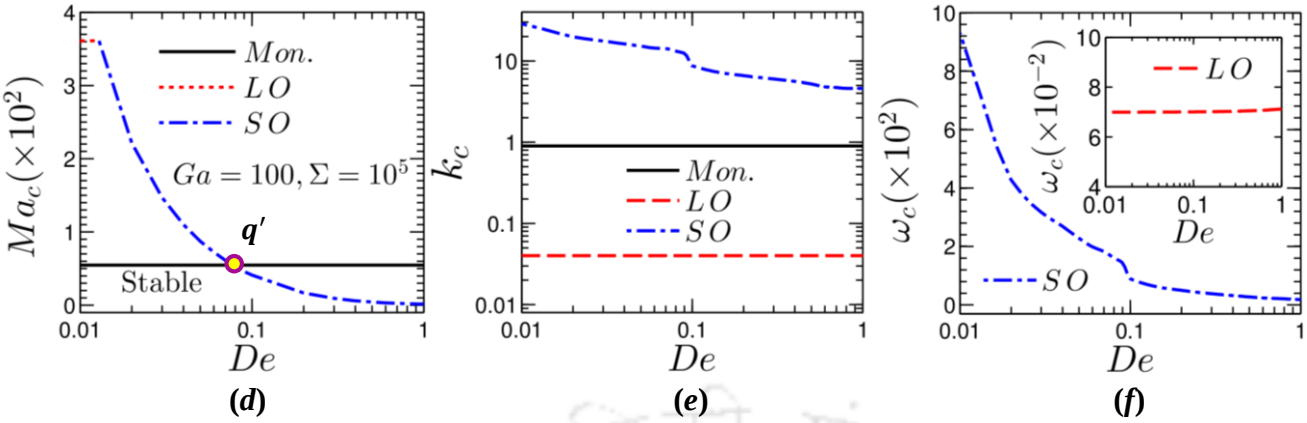

Figure 3.8: Variation of the critical Marangoni number (*a*) and (*d*), the corresponding critical wave number (*b*) and (*e*), and the frequency of critical perturbations (*c*) and (*f*) with Deborah number at $Bi = 0.05$ and $Pr = 10$. Panels (*a*)-(*b*)-(*c*) and (*d*)-(*e*)-(*f*) represent the variations for $(Ga, \Sigma) = (0.1, 10^3)$ and $(Ga, \Sigma) = (10^2, 10^5)$ respectively. In each panel, the solid line corresponds to the monotonic (*mon.*) mode, dashed one to the long-wave oscillatory (LO) mode and the dashed-dotted line represent the short-wave oscillatory (SO) mode respectively.

A comparison between Figs. 3.8 (*b* – *c*) and 3.8 (*e* – *f*) further reveal that k_c and ω_c for the short-wave oscillatory mode remain independent of the deformability of the free surface, but vary drastically with *De*. This variation can be approximated by the asymptotes $k_c \sim De^{-3}$ and $\omega_c \sim De^{-1}$ respectively, which suggests that oscillatory convection cells are more likely to be visible for a fluid with higher elasticity and remains non-existent in Newtonian fluids. The Biot number, which dictates the variation of k_c and ω_c in the long-wave regime, has apparently no influence in this elasticity induced instability mode. The dominance of the fluid elasticity over the viscous effects makes this instability mode fundamentally different from the instabilities in Newtonian fluids.

Figure 3.9 depicts the boundary between the monotonic and oscillatory instability modes in the $De - Bi$ plane for the long-wave and short-wave disturbances. It is worth mentioning here that, each point on this *De* – *Bi* plane represents a global minimum in the neutral stability curve. Therefore, for any particular combination of *Bi* and *De*, Fig. 3.9 can tell us the instability mode prevailing in the liquid layer. Notably, a parameter set corresponding to any of these curves depicts a competition between its adjacent instability modes. It is clear that when the deformability of the free surface is high, both long-wave and short-wave instabilities can appear in the system depending on the magni-

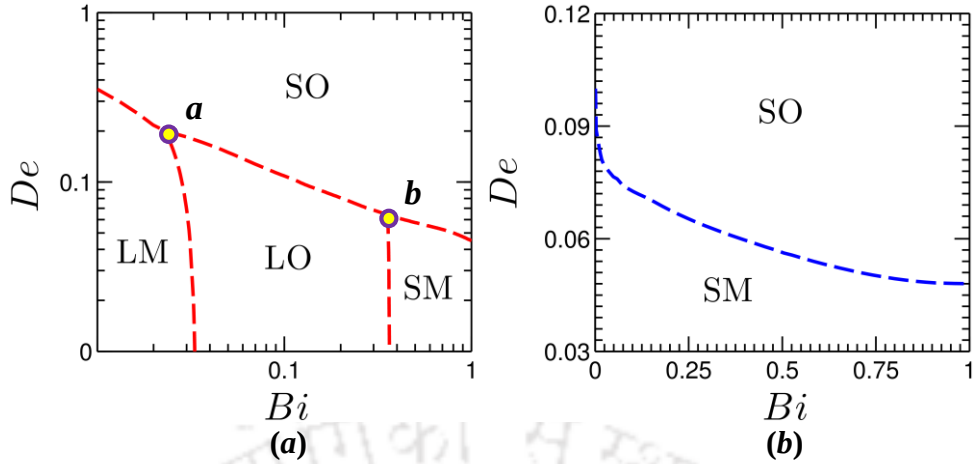

Figure 3.9: The domains of monotonic and oscillatory instability modes. Panel (*a*) corresponds to $(Ga,\Sigma)=(0.1,10^3)$; panel (*b*) corresponds to $(Ga,\Sigma)=(10^2,10^5)$. $Pr=10$. LM, LO, SM and SO represent the domains of long-wave monotonic, long-wave oscillatory, short-wave monotonic and short-wave oscillatory mode respectively.

tude of *De* and *Bi*. Noteworthily, for this kind of a system, point ***a*** and ***b*** draws special attention, where three different instability modes *viz.* LM – LO – SO and SM – SO – LO respectively, compete to become the dominant instability mode in the system. On the other hand, with the reduction in deformability of the free surface, irrespective of the magnitude of *Bi*, the short-wave instability mode takes the dominant form as can be seen from Fig. 3.9(*b*).

3.6 Experimental Feasibility

In this section, we discuss the experimental possibilities regarding the observation of Marangoni instability in a viscoelastic liquid layer. For doing so, we consider a system comprising of polyethylene oxide (PEO) solution with $\rho=10^3\,\mathrm{kg\,m^{-3}}$, $\mu_o=0.01\,\mathrm{Pa.s}$, $\lambda=0.02\,\mathrm{s}$ [75]. As demonstrated in Fig. 3.3, for the set of parameters $De=0.1$, $Ga=0.1$, the long-wave oscillatory mode becomes critical with $Ma_c\approx 39$, $k_c\approx 0.13$ and $\omega_c\approx 0.1$. Now, considering $\sigma_T\approx O(10^{-4})\,\mathrm{Nm^{-1}\,K^{-1}}$ and $\alpha\approx O(10^{-7})\mathrm{m^2s^{-1}}$, we found H and g as 0.14 mm and 0.04 m s^{-2} respectively. Under these sets of conditions, the abovementioned critical Marangoni number is attained at a temperature difference of 3 K. The characteristic wavelength is estimated to be 1.1 mm with the period of oscillations

2 s. Furthermore, since this long-wave oscillatory instability emerges in the range $Bi \approx O(10^{-2} \sim 10^{-1})$, q can be $O(10)\,\mathrm{Wm^{-2}K^{-1}}$.

3.7 Summary

We investigate in this study, the thermal Marangoni instability in a thin viscoelastic Maxwellian liquid film confined between its deformable free surface and a flat substrate of very low thermal conductivity. Linear stability analysis reveals that; besides the conventional short-wave mode, long-wave disturbances can also emerge in this system depending on the values of the model parameters. This long-wave instability mode is investigated here by deriving a set of amplitude equations that govern the coupled non-linear evolution of the liquid layer thickness and primary part of the temperature (averaged across the layer). Linear stability analysis performed within this set of amplitude equations yields a dispersion relationship that ensures the emergence of both the long-wave monotonic and oscillatory instability in the system. The short-wave oscillatory instability is detected in the system for $De > 0$, which is exclusively governed by the elasticity of the fluid.

Chapter 4

Thermosolutal Marangoni Instability in a Viscoelastic Liquid Film

In this chapter, the Marangoni instability problem in a viscoelastic film is studied considering a complete thermosolutal model. The film, bounded above by a deformable free surface, is subjected to heating from below by a solid substrate. Linear stability analysis shows that both the monotonic and oscillatory disturbances are possible in this system. Besides exploring the role of liquid elasticity on the film dynamics, this investigation also reveals the instability modes emerging from the interaction between the thermocapillary and solutocapillary forces.

4.1 Introduction

In Chapter 3, the instability problem for a viscoelastic film is studied considering a purely thermal model. However, it is important to note that viscoelastic liquids such as polymeric solutions, biofluids etc. are essentially binary in nature. They are the binary mixture of polymeric solute in a Newtonian solvent, e.g. poly(ethylene oxide) in water, poly(vinyl alcohol) in water, polystyrene in dioctyl phthalate etc. [77]. Quite interestingly, an applied temperature gradient usually leads to the stratification of these solutes via the Soret effect. While the solutes usually migrate towards a colder region (owing to their large masses), nevertheless, they also move sometimes into the warmer region depending on the solvent quality and the temperature of the mixture [76]. This migration of the solutes can lead to the development of solutocapillary stress on the free surface of a viscoelastic liquid film. Hence, a complete thermosolutal model is essential to investigate the Marangoni instability in a viscoelastic liquid film. This is the primary objective of this study. It is found that in the presence of Soret diffusion, the interaction

The contents of this chapter have been published as Sarma, R. and Mondal, P. K. (2021) "Marangoni instability in a viscoelastic binary film with cross-diffusive effect", J. Fluid Mech., vol. 910, A30.

between thermocapillary and solutocapillary forces is found to give rise to two different oscillatory instabilities, of which one mode was overlooked previously, even for the Newtonian binary mixtures. An approximate model is also developed here under the framework of long-wave analysis, which can qualitatively depict the stability behavior of the system without numerically solving the problem.

The contents of this chapter are organised as follows: the problem is mathematically formulated in Section 4.2 by presenting the set of governing equations and boundary conditions. Linear stability analysis of the system is then carried out in Section 4.3. The stability picture generated by numerically solving the eigenvalue problem is analysed in Section 4.4. An approximate model is then developed in Section 4.5. To provide a comprehensive picture of the susceptibility to different instability modes based on model parameter values, we plot the phase diagrams in Section 4.6. Finally, the conclusions are drawn in Section 4.7.

4.2 Mathematical Model

We begin by considering a thin, two-dimensional layer of an incompressible viscoelastic polymer solution in the gravitational field **g** as shown in Fig. 4.1. The solution is a binary mixture of polymeric solute and Newtonian solvent, characterized by the relaxation time λ, viscosity μ_o, density ρ, thermal conductivity κ, thermal diffusivity α, mass diffusivity D, and surface tension σ.

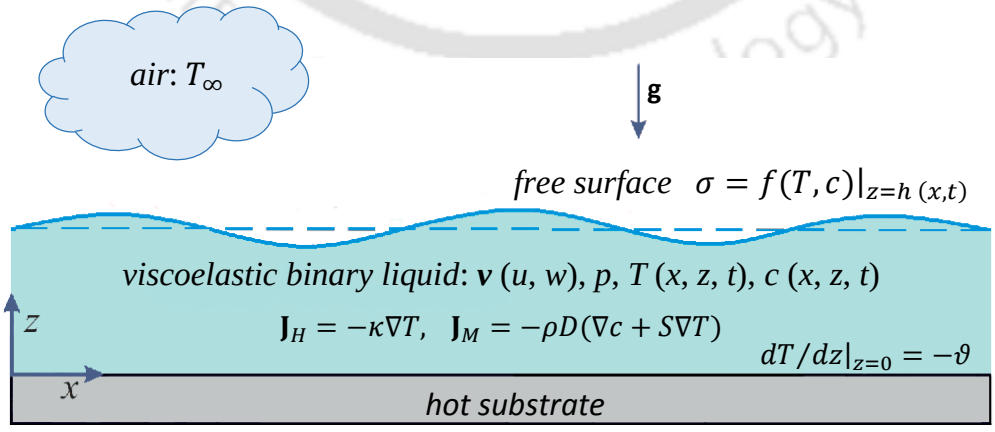

Figure 4.1: Schematic illustration of the physical system under consideration. A thin viscoelastic film (composed of a polymeric solute in a Newtonian solvent) confined

between its deformable free surface $z = h(x,t)$ and a horizontal substrate in the gravitational field **g**, is subjected to a vertical temperature gradient. This applied temperature gradient induces a concentration gradient in the film via the Soret effect. The surface tension gradient arising from inhomogeneities in temperature and concentration at the air-liquid interface induces Marangoni convection in the liquid layer. The dashed line corresponds to the undeformed interface at the quiescent base state.

We consider the film to be of infinite horizontal extent $x \in (-\infty, \infty)$ with unperturbed thickness *H*. At the $z = 0$ plane, the film is in thermal contact with a poorly conductive rigid substrate, while a deformable free surface located at $z = h(x,t)$ separates it from the ambient gas phase. A transverse temperature gradient exists in the entire binary mixture, which is specified to be $-\vartheta$ at $z = 0$. This signifies that $\vartheta > 0$ ($\vartheta < 0$) corresponds to the case of heating the liquid layer from the substrate (gas) side. We restrict this analysis only to the case of heating from below. The incorporation of Soret effect into the analysis indicates that mass flux in the flow domain is a combination of concentration and temperature gradients [109]. Hence, the heat $\mathbf{J}_{\mathrm{H}}$ and mass $\mathbf{J}_{\mathrm{M}}$ fluxes within the film are governed by,

$$\mathbf{J}_{\mathrm{H}} = -\kappa \nabla T, \tag{4.1a}$$

$$\mathbf{J}_{\mathrm{M}} = -\rho D\left(\nabla c + \mathcal{S}\nabla T\right), \tag{4.1b}$$

where $\mathcal{S}$ is the Soret coefficient of the mixture. For a polymeric solution, $\mathcal{S}$ can be either positive or negative depending on the solvent quality, the mole fractions of the components, and the temperature of binary mixture [77]. A negative (positive) sign of $\mathcal{S}$ signifies the migration of polymeric solutes towards the warmer (colder) region. It follows from Eq. 4.1 that, at the conductive state, the externally applied heat flux generates a temperature difference $\Delta T = \vartheta H$, which, in turn, yields a concentration difference $\Delta c = -\mathcal{S}\Delta T$ across the layer.

Now, above a particular temperature gradient, the thermo- and solutocapillary effects induce Marangoni convection in this mixture. The buoyancy effect is neglected in this study, considering the small thickness of the film. We assume the surface tension to vary linearly with temperature and solute concentration, dictated by the relationship:

$$\sigma = \sigma_o - \sigma_T\left(T - T_o\right) + \sigma_c\left(c - c_o\right), \tag{4.2}$$

where σ_o is the surface tension at the reference temperature T_o and concentration c_o;

$\sigma_T = -d\sigma/dT$ and $\sigma_c = d\sigma/dc$ quantifies the rate of change of surface tension with respect to temperature and concentration. It should be noted that for most of the polymeric solutions $(\sigma_T, \sigma_c) > 0$ [84]. Furthermore, except σ, all other thermophysical properties are assumed to remain invariant of temperature in this analysis.

4.2.1 Governing equations

In the presence of linear Soret effect, the equations governing the fields of fluid velocity $\boldsymbol{v} \equiv \{u(x,z,t), w(x,z,t)\}$, pressure $p(x,z,t)$, temperature $T(x,z,t)$ and concentration $c(x,z,t)$ in the bulk of the film are given by,

$$\nabla \bullet \boldsymbol{v} = \boldsymbol{0}, \tag{4.3a}$$

$$\rho\left(\frac{\partial \boldsymbol{v}}{\partial t} + \boldsymbol{v} \bullet \nabla \boldsymbol{v}\right) = -\nabla p + \nabla \bullet \boldsymbol{\tau} - \rho g\, \boldsymbol{k}, \tag{4.3b}$$

$$\frac{\partial T}{\partial t} + \boldsymbol{v} \bullet \nabla T = \alpha\, \nabla^2 T, \tag{4.3c}$$

$$\frac{\partial c}{\partial t} + \boldsymbol{v} \bullet \nabla c = D\nabla^2 c + \mathcal{S}D\, \nabla^2 T, \tag{4.3d}$$

respectively, where *t* represents time, $\boldsymbol{\tau} = \begin{bmatrix} \boldsymbol{\tau}_{xx} & \boldsymbol{\tau}_{xz} \\ \boldsymbol{\tau}_{zx} & \boldsymbol{\tau}_{zz} \end{bmatrix}$ is the deviatoric stress tensor, $\boldsymbol{k}$ is the unit vector in the *z*-direction, and $\nabla \equiv \{\partial/\partial x, \partial/\partial z\}$. The above set of governing equations are accompanied by the following boundary conditions:

At the $z = 0$ plane, where the film is in thermal contact with a rigid substrate, the pertinent boundary conditions encompass the no-slip, no penetration condition for velocity, a specified uniform normal heat flux, and the mass impermeability condition, represent respectively by,

$$\boldsymbol{v} = \boldsymbol{0}, \quad \frac{\partial T}{\partial z} = -\vartheta, \quad \frac{\partial c}{\partial z} = \mathcal{S}\vartheta \qquad \text{at } z = 0. \tag{4.4a-c}$$

At the deformable free surface $z = h(x,t)$, the boundary conditions comprise of the kinematic boundary condition, heat exchange with the ambient-gas phase (characterized by Newton's law of cooling), mass impermeability condition, and the balance of tangential and normal stress components, represented respectively by

$$w = \frac{\partial h}{\partial t} + u\ \frac{\partial h}{\partial x}, \tag{4.5a}$$

$$-\kappa\left(\frac{\partial h}{\partial x}\frac{\partial T}{\partial x} - \frac{\partial T}{\partial z}\right) + q\left(T - T_\infty\right)\sqrt{1+\left(\partial h/\partial x\right)^2} = 0, \tag{4.5b}$$

$$\kappa\left(-\frac{\partial h}{\partial x}\frac{\partial c}{\partial x} + \frac{\partial c}{\partial z}\right) - \mathcal{S}q\left(T - T_\infty\right)\sqrt{1+\left(\partial h/\partial x\right)^2} = 0, \tag{4.5c}$$

$$\frac{1}{\sqrt{1+\left(\partial h/\partial x\right)^2}}\left\{\tau_{xz}\left[1-\left(\frac{\partial h}{\partial x}\right)^2\right] + \tau_{zz}\frac{\partial h}{\partial x} - \tau_{xx}\frac{\partial h}{\partial x}\right\} = \frac{\partial \sigma}{\partial x} + \frac{\partial \sigma}{\partial z}\frac{\partial h}{\partial x}, \tag{4.5d}$$

$$-p + \frac{1}{1+\left(\partial h/\partial x\right)^2}\left[\tau_{zz} + \tau_{xx}\left(\frac{\partial h}{\partial x}\right)^2 - 2\ \tau_{xz}\frac{\partial h}{\partial x}\right] = \sigma\frac{\partial^2 h/\partial x^2}{\left[1+\left(\partial h/\partial x\right)^2\right]^{3/2}}$$

$$\text{at } z = h\left(x,t\right). \tag{4.5e}$$

In Eqs. 4.5(*b*,*c*), q denotes the rate of heat exchange between the free surface and the ambient air at temperature T_∞. The kinematic boundary condition (Eq. 4.5*a*) gives the interface location at time t, while the mass impermeability condition (Eq. 4.5*c*) portrays the non-volatile behavior of the binary mixture. The dynamics of gas-phase are decoupled here from the liquid phase by considering large differences in the physical properties between both phases.

We use here the Maxwell constitutive model to depict the rheological behavior of the liquid [62]:

$$\boldsymbol{\tau} + \lambda\frac{\partial \boldsymbol{\tau}}{\partial t} = \mu_o\left[\left(\nabla \boldsymbol{v}\right) + \left(\nabla \boldsymbol{v}\right)^T\right], \tag{4.6}$$

4.2.2 Non-dimensionalization

The BVP formulated by Eqs. 4.3 – 4.5 is now non-dimensionalized considering the unperturbed film thickness H as characteristic length scale, the thermal diffusion time H^2/α as characteristic time scale, and ϑH as temperature scale.

This allows us to define the following set of dimensionless variables:

$$\left.\begin{aligned}\left(\bar{x},\bar{z}\right) = \frac{(x,z)}{H},\quad \bar{h} = \frac{h}{H},\quad \bar{t} = \frac{t}{H^2/\alpha},\quad \left(\bar{u},\bar{w}\right) = \frac{u,w}{\left(\alpha/H\right)},\quad \bar{\tau} = \frac{\tau}{\mu\alpha/H^2},\\ \bar{p} = \frac{p}{\mu\alpha/H^2},\quad \bar{T} = \frac{T-T_\infty}{\vartheta H},\quad \bar{c} = \frac{c}{\sigma_T\vartheta H/\sigma_c}.\end{aligned}\right\} \tag{4.7}$$

With this choice of the non-dimensional variables, we finally obtain the governing equations and the boundary conditions (dropping the overbar sign for notational convenience) in the following dimensionless form:

$$\nabla \bullet \boldsymbol{v} = \boldsymbol{0}, \tag{4.8a}$$

$$Pr^{-1}\left(\frac{\partial \boldsymbol{v}}{\partial t} + \boldsymbol{v} \bullet \nabla \boldsymbol{v}\right) = -\nabla p + \nabla \bullet \boldsymbol{\tau} - Ga\,\boldsymbol{k}\,, \tag{4.8b}$$

$$\frac{\partial T}{\partial t} + \boldsymbol{v} \bullet \nabla T = \nabla^2 T\,, \tag{4.8c}$$

$$\frac{\partial c}{\partial t} + \boldsymbol{v} \bullet \nabla c = Le\left(\nabla^2 c + \chi \nabla^2 T\right); \tag{4.8d}$$

$$\boldsymbol{v} = \boldsymbol{0}, \qquad \frac{\partial T}{\partial z} = -1, \qquad \frac{\partial c}{\partial z} = \chi \qquad \text{at } z = 0, \tag{4.9a-c}$$

$$w = \frac{\partial h}{\partial t} + u\frac{\partial h}{\partial x}\,, \tag{4.10a}$$

$$\left(\frac{\partial T}{\partial z} - \frac{\partial h}{\partial x}\frac{\partial T}{\partial x}\right) + Bi\; T\sqrt{1+\left(\partial h/\partial x\right)^2} = 0\,, \tag{4.10b}$$

$$\left(\frac{\partial c}{\partial z} - \frac{\partial h}{\partial x}\frac{\partial c}{\partial x}\right) - \chi Bi\; T\sqrt{1+\left(\partial h/\partial x\right)^2} = 0\,, \tag{4.10c}$$

$$-p + \frac{1}{1+\left(\partial h/\partial x\right)^2}\left[\tau_{zz} + \tau_{xx}\left(\frac{\partial h}{\partial x}\right)^2 - 2\tau_{xz}\frac{\partial h}{\partial x}\right] = \Sigma\frac{\partial^2 h/\partial x^2}{\left[1+\left(\partial h/\partial x\right)^2\right]^{3/2}}\,, \tag{4.10d}$$

$$\frac{1}{\sqrt{1+\left(\partial h/\partial x\right)^2}}\left\{\tau_{xz}\left[1-\left(\frac{\partial h}{\partial x}\right)^2\right] + \tau_{zz}\frac{\partial h}{\partial x} - \tau_{xx}\frac{\partial h}{\partial x}\right\} = Ma\left[-\frac{\partial T}{\partial x} + \frac{\partial c}{\partial x} + \left(-\frac{\partial T}{\partial z} + \frac{\partial c}{\partial z}\right)\frac{\partial h}{\partial x}\right]$$

$$\text{at } z = h\left(x,t\right). \tag{4.10e}$$

Moreover, in non-dimensional form, the Maxwell constitutive model reads

$$\boldsymbol{\tau} + De\frac{\partial \boldsymbol{\tau}}{\partial t} = \left[\left(\nabla \boldsymbol{v}\right) + \left(\nabla \boldsymbol{v}\right)^T\right]. \tag{4.11}$$

This problem is now characterized by the following set of dimensionless parameters: the Marangoni number, *Ma*, the Prandtl number, *Pr*, the Deborah number, *De*, the (inverse) Lewis number, *Le*, the Soret number, χ, the Biot number, *Bi*, the Galileo number, *Ga*, and the (inverse) capillary number, Σ:

$$\left.\begin{aligned} Ma &= \frac{\sigma_T \vartheta H^2}{\mu_o \alpha}, \quad Pr = \frac{\mu_o}{\rho \alpha}, \quad De = \frac{\lambda \alpha}{H^2}, \quad Le = \frac{D}{\alpha}, \\ \chi &= \frac{\mathcal{S}\sigma_c}{\sigma_T}, \quad Bi = \frac{qH}{\kappa}, \quad Ga = \frac{\rho g H^3}{\mu_o \alpha}, \quad \Sigma = \frac{\sigma H}{\mu_o \alpha}. \end{aligned}\right\} \tag{4.12}$$

Except for *Le* and χ, the rest of the parameters are defined in the same manner as that in Chapter 3. The (inverse) Lewis number compares the characteristic mass diffusion time scale H^2/D to the thermal diffusion time scale H^2/α. *Le* is usually small for binary liquid mixtures and lies within $O(10^{-5}) \lesssim Le \lesssim O(10^{-1})$. The Soret number takes into account the relative contribution of thermocapillary and solutocapillary force to the free surface force. χ can be either positive or negative based on the Soret coefficient $\mathcal{S}$. The typical value of χ varies within $-1 \le \chi \le 1$. Furthermore, to reveal the role of surface deformability on stability characteristics of the system, we consider here two separate cases : (*i*) $(Ga, \Sigma) = (0.1, 10^3)$, that represents a liquid layer with a deformable free surface at the microgravity environment, and (*ii*) $(Ga, \Sigma) \to \infty$, which refers to a liquid layer with a non-deformable free surface.

4.3 Base State and Linear Stability Analysis

This section presents a linear stability analysis for small perturbations around the quiescent liquid film with laterally uniform temperature and concentration distribution. This purely conductive state of the system is represented by

$$\begin{aligned} \boldsymbol{v}^o = \boldsymbol{0}, \quad \boldsymbol{\tau}^o = \boldsymbol{0}, \quad h^o = 1, \quad p^o = Ga(1-z), \\ T^o = 1 - z + Bi^{-1}, \quad c^o = \chi z + const. \end{aligned} \tag{4.13a-f}$$

which are steady-state solutions of Eqs. 4.8 – 4.10. One can notice that the elasticity of the liquid does not influence this basic state. We now study the stability of this base state by introducing the following two-dimensional infinitesimal normal perturbations (denoted by a tilde) to the steady-state solutions,

$$\begin{aligned} \boldsymbol{v} &= \boldsymbol{v}^o + \tilde{\boldsymbol{v}}(x,z,t), \quad \boldsymbol{\tau} = \boldsymbol{\tau}^o + \tilde{\boldsymbol{\tau}}(x,z,t), \quad p = p^o + \tilde{p}(x,z,t), \\ T &= T^o + \tilde{\theta}(x,z,t), \quad h = h^o + \tilde{\xi}(x,z,t), \quad c = c^o + \tilde{c}(x,z,t). \end{aligned} \tag{4.14a-f}$$

Linearization of Eqs. 4.8 – 4.10 by neglecting the terms nonlinear in perturbations yields the following set of governing equations and boundary conditions:

$$\nabla \bullet \tilde{\boldsymbol{v}} = \mathbf{0}, \tag{4.15a}$$

$$Pr^{-1}\frac{\partial \tilde{\boldsymbol{v}}}{\partial t} = -\nabla \tilde{p} + \nabla \bullet \tilde{\boldsymbol{\tau}}, \tag{4.15b}$$

$$\frac{\partial \tilde{\theta}}{\partial t} = \nabla^2 \tilde{\theta} + \tilde{w}, \tag{4.15c}$$

$$\frac{\partial \tilde{c}}{\partial t} + \chi \tilde{w} = Le\left(\nabla^2 \tilde{c} + \chi \nabla^2 \tilde{T}\right); \tag{4.15d}$$

$$\tilde{\boldsymbol{v}} = \mathbf{0}, \quad \frac{\partial \tilde{\theta}}{\partial z} = 0, \quad \frac{\partial \tilde{c}}{\partial z} = 0 \qquad \text{at } z = 0, \tag{4.16a-c}$$

$$\frac{\partial \tilde{\xi}}{\partial t} = \tilde{w}, \quad \frac{\partial \tilde{\theta}}{\partial z} = -Bi\left(\tilde{\theta} - \tilde{\xi}\right), \quad \frac{\partial \tilde{c}}{\partial z} = \chi Bi\left(\tilde{\theta} - \tilde{\xi}\right),$$
$$\tilde{\tau}_{xz} = Ma\frac{\partial}{\partial x}\left(\tilde{c} - \tilde{\theta} + \tilde{\xi} + \chi\tilde{\xi}\right), \quad -\tilde{p} + Ga\ \tilde{\xi} + \tilde{\tau}_{zz} = \Sigma\ \frac{\partial^2 \tilde{\xi}}{\partial x^2} \quad \text{at } z = 1, \tag{4.17a-e}$$

whereas the constitutive Eq. 4.11 reads

$$\tilde{\boldsymbol{\tau}} + De\frac{\partial \tilde{\boldsymbol{\tau}}}{\partial t} = \left[\left(\nabla \tilde{\boldsymbol{v}}\right) + \left(\nabla \tilde{\boldsymbol{v}}\right)^T\right]. \tag{4.18}$$

We now cast this BVP in terms of the stream function $\tilde{\psi}(x,z,t)$ so that

$$\tilde{u} = \frac{\partial \tilde{\psi}}{\partial z}, \qquad \tilde{w} = -\frac{\partial \tilde{\psi}}{\partial x}. \tag{4.19a,b}$$

The basic idea behind the stream function formulation is to eliminate the pressure term $\tilde{p}$ from the system of Eqs. 4.15 – 4.17. Introducing relationships (4.19) and the constitutive equation for Maxwell viscoelastic model into Eqs. 4.15 – 4.17, we finally arrive at:

$$Pr^{-1}\left(\frac{\partial}{\partial t}\nabla^2 \tilde{\psi} + De\frac{\partial^2}{\partial t^2}\nabla^2 \tilde{\psi}\right) = \nabla^4 \tilde{\psi}, \tag{4.20a}$$

$$\frac{\partial \tilde{\theta}}{\partial t} = \nabla^2 \tilde{\theta} - \frac{\partial \tilde{\psi}}{\partial x}, \tag{4.20b}$$

$$\frac{\partial \tilde{c}}{\partial t} - \chi\frac{\partial \tilde{\psi}}{\partial x} = Le\left[\nabla^2 \tilde{c} + \chi \nabla^2 \tilde{T}\right], \tag{4.20c}$$

with the boundary conditions,

$$\tilde{\psi} = 0, \quad \frac{\partial \tilde{\psi}}{\partial z} = 0, \quad \frac{\partial \tilde{\theta}}{\partial z} = 0, \quad \frac{\partial \tilde{c}}{\partial z} = 0 \qquad \text{at } z = 0, \tag{4.21a-d}$$

$$\frac{\partial \tilde{\xi}}{\partial t} = -\frac{\partial \tilde{\psi}}{\partial x}, \quad \frac{\partial \tilde{\theta}}{\partial z} = -Bi\left(\tilde{\theta} - \tilde{\xi}\right), \quad \frac{\partial \tilde{c}}{\partial z} = \chi Bi\left(\tilde{\theta} - \tilde{\xi}\right), \tag{4.22a-c}$$

$$\frac{\partial^2\tilde{\psi}}{\partial z^2}-\frac{\partial^2\tilde{\psi}}{\partial x^2}=Ma\frac{\partial}{\partial x}\left(\tilde{c}-\tilde{\theta}+\tilde{\xi}+\chi\tilde{\xi}\right)+Ma\,De\frac{\partial^2}{\partial t\partial x}\left(\tilde{c}-\tilde{\theta}+\tilde{\xi}+\chi\tilde{\xi}\right), \qquad (4.22d)$$

$$\left(1+De\frac{\partial}{\partial t}\right)\left(\Sigma\ \frac{\partial^3\tilde{\xi}}{\partial x^3}-Pr^{-1}\frac{\partial^2\tilde{\psi}}{\partial t\partial z}-Ga\ \ \frac{\partial\tilde{\xi}}{\partial x}\right)=-\frac{\partial}{\partial z}\left(3\frac{\partial^2}{\partial x^2}+\frac{\partial^2}{\partial z^2}\right)\tilde{\psi}\quad \text{at } z=1. \quad (4.22e)$$

Noticing that the basic state is invariant with respect to x and t, we use the Fourier decomposition to separate the x and t dependency of the perturbed fields $(\tilde{\psi},\tilde{\theta},\tilde{c},\tilde{\xi})$ from that with z:

$$\left(\tilde{\psi}(x,z,t),\ \tilde{\theta}(x,z,t),\ \tilde{c}(x,z,t),\ \tilde{\xi}(x,z,t)\right)=\left(\hat{\psi}(z),\ \hat{\theta}(z),\ \hat{c}(z),\ \hat{\xi}(z)\right)\exp\left(i\,k\,x-\lambda\,t\right), \quad (4.23)$$

where $(\hat{\psi},\hat{\theta},\hat{c},\hat{\xi})$ are the amplitudes of perturbations, k denotes the dimensionless horizontal wavenumber and $\lambda=\Omega+i\omega$ refers to the decay rate of perturbations. The parameter ω (a real quantity) represents the frequency of perturbation. Hence, the dynamics of these infinitesimal perturbations is now governed by the following EVP:

$$Pr\frac{d^4\hat{\psi}}{dz^4}-\left(\lambda^2De-\lambda+2Prk^2\right)\frac{d^2\hat{\psi}}{dz^2}+\left(\lambda^2De-\lambda+Prk^2\right)k^2\hat{\psi}=0, \qquad (4.24a)$$

$$\frac{d^2\hat{\theta}}{dz^2}+\left(\lambda-k^2\right)\hat{\theta}=i\,k\ \hat{\psi}, \qquad (4.24b)$$

$$Le\frac{d^2\hat{c}}{dz^2}+\left(\lambda-Lek^2\right)\hat{c}=-Le\chi\left(\frac{d^2\hat{\theta}}{dz^2}-k^2\hat{\theta}\right)-i\chi k\hat{\psi}; \qquad (4.24c)$$

$$\hat{\psi}=0,\quad \frac{d\hat{\psi}}{dz}=0,\quad \frac{d\hat{\theta}}{dz}=0,\quad \frac{d\hat{c}}{dz}=0 \qquad \text{at } z=0, \qquad (4.25a\text{-}d)$$

$$i\,k\hat{\psi}=\lambda\hat{\xi},\quad \frac{d\hat{\theta}}{dz}=-Bi\left(\hat{\theta}-\hat{\xi}\right),\quad \frac{d\hat{c}}{dz}=\chi Bi\left(\hat{\theta}-\hat{\xi}\right), \qquad (4.26a\text{-}c)$$

$$\frac{d^2\hat{\psi}}{dz^2}+k^2\hat{\psi}=i\,Ma\,k\left(1-\lambda De\right)\left(\hat{c}-\hat{\theta}+\chi\hat{\xi}+\hat{\xi}\right), \qquad (4.26d)$$

$$Pr\frac{d^3\hat{\psi}}{dz^3}+\left(\lambda-\lambda^2De-3Prk^2\right)\frac{d\hat{\psi}}{dz}=i\,kPr\left(1-\lambda De\right)\left(Ga+\Sigma k^2\right)\hat{\xi}$$
$$\text{at } z=1, \qquad (4.26e)$$

with λ and Ma as the eigenvalues. Solving the system of Eqs. 4.24 – 4.26 for $\Omega=0$, now one can obtain the neutral stability curves which demarcate the stable regime from the unstable one. However, the complexity of solvability conditions here restrains us from taking an analytical approach. Therefore, the EVP is solved numerically using the fourth-order Runge-Kutta method with shooting technique [108] for disturbances with arbitrary

values of k. An approximate model will be developed in Section 4.5 in the asymptotic limit $k \to 0$.

We have verified the accuracy of our numerical scheme by comparing the results with those available in the literature as well as with the results obtained from the approximate model. However, confronted by the lack of published results on the thermosolutal Marangoni convection for viscoelastic liquids, we first test the accuracy of our numerical solution against the results of Shklyaev *et al.* [110]. These authors numerically investigated the instability problem for a Newtonian binary mixture. In Fig. 4.2, one can see that an excellent quantitative agreement exists between the present results and the computations of [110] for both the values of *Bi*. The numerical results are also found to agree well with the results of the approximate model (compared in Figs. 14-16) for all but excluding the parameter values that violate the approximations necessary to derive the model (discussed in Section 4.5). These comparisons ensure the accuracy of the present numerical scheme for the entire parametric range of interest.

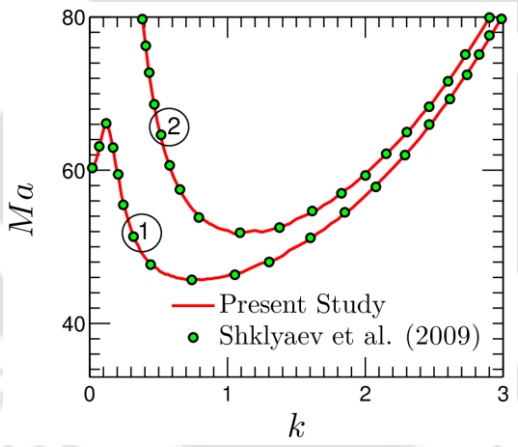

Figure 4.2: Comparison of the present numerical result with the results of Shklyaev *et al.* [110] (shown by marker "**o**") via the neutral stability curve at $Pr = 2$, $\chi = -0.2$, $Le = 10^{-3}$. Curves marked by 1 and 2 corresponds to $Bi = 0$ and $Bi = 0.1$ respectively. To represent the characteristics of a Newtonian binary liquid with a non-deformable free surface, we consider $De = 0$ and $(Ga, \Sigma) \to \infty$.

The EVP posed by Eqs. 4.24 – 4.26 suggests the possible emergence of two different instability modes in the system: (*i*) monotonic mode (or stationary convection) and (*ii*) oscillatory mode (or overstability) for which the disturbances grow with temporal oscillations. The stability thresholds for the monotonic and oscillatory modes can be obt-

ained from Eqs. 4.24 – 4.26 by substituting $\lambda = 0$ and $\lambda = i\omega$ respectively.

4.4 The Linear Stability Picture

In this section, we analyze the stability picture obtained through numerical computations. Emphasis is put on understanding how viscoelasticity in the presence of Soret effect deviates the stability characteristics of the system from its Newtonian counterpart. For convenience in analysis, we divide the entire disturbance spectrum into two different regimes: (*i*) long-wave regime, $k < O(1)$, and (*ii*) short-wave regime, $k \gtrsim O(1)$. Furthermore, it is important to remark that we fix $Pr = 10$ for all the graphical results. This is because the stability margin shows no substantial variation with *Pr* against both the long-wave and short-wave perturbations (this is also apparent from the approximate model derived in Section 4.5).

4.4.1 Effect of elasticity and the free surface deformability

Let us first start with the monotonic instability mode. Figure 4.3 plots the neutral stability curves for this instability mode. The solid line represents here the stability threshold for a liquid layer with a deformable free surface $(Ga, \Sigma) = (0.1, 10^3)$, while the dotted one depicts the stability margin for a non-deformable surface $(Ga, \Sigma) \to \infty$. It can be observ-

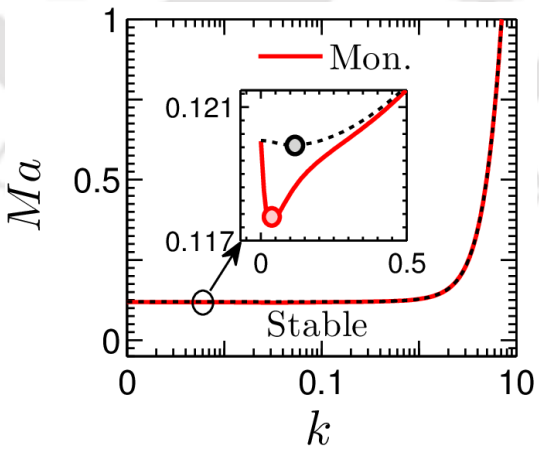

Figure 4.3: Neutral stability curves $Ma\,(k)$ for the monotonic instability mode. The solid line represents the stability threshold for a deformable free surface $(Ga, \Sigma) = (0.1, 10^3)$, whereas the dotted line demonstrates the stability margin for a non-deformable free surface $(Ga, \Sigma) \to \infty$. The dot (o) mark on each neutral curve represents the critical point of the curve. Inset depicts the effect of free surface deformability on the stability threshold

in the long-wave regime. Other parameters: $Bi = 0.01$, $\chi = 0.5$, $Le = 10^{-3}$, $Pr = 10$.

ed that over the entire range of disturbance wavenumber *k*, there exists a minimum value for Marangoni number *Ma* (indicated by the marker "o") only above which the instability first sets in the system. We call this *Ma* as the critical Marangoni number (Ma_c) and the corresponding *k* and ω as the critical wavenumber (k_c) and critical oscillation frequency (ω_c), respectively.

From Fig. 4.3 it is clear that irrespective of the free surface deformability, the monotonic disturbances always emerge in the long-wave form ($k_c << O(1)$). Nevertheless, the increased gravitational and surface tension forces for a non-deformable surface slightly delay the onset of these disturbances in the system ($Ma_{c,(Ga,\Sigma)\to\infty} > Ma_{c,(Ga,\Sigma)\to(0.1,10^3)}$, as can be clearly seen in the inset of Fig. 4.3). Notably, the monotonic instability threshold is not affected by the elastic behavior of the liquid. This is due to the vanishing of any temporal components for this stationary convection. The role of other non-dimensional parameters on the stability margin for this instability mode will be discussed systematically in the subsequent subsections.

We now focus our attention on the disturbances that emerge with temporal oscillations $(\omega \neq 0)$, giving rise to Hopf bifurcation. The analysis in Chapter 2 suggests that the oscillatory disturbances are more likely to appear in a highly viscoelastic film. For the present thermo-solutal convection process, we will demonstrate that depending on the nature of Soret coefficient (*i.e.*, whether $\chi > 0$ or $\chi < 0$), two different oscillatory instabilities can emerge in the system. We call them as the oscillatory-I and oscillatory-II mode. It is important to remark that the characteristics of oscillatory-I mode have been extensively studied in the literature in the context of a Newtonian binary mixture [13,104,110,111]. However, its behavior for a viscoelastic binary liquid has not been investigated yet. On the other hand, to our knowledge, the oscillatory-II mode has entirely remained unexplored, even for a Newtonian binary liquid (perhaps due to limited examination over the model parameters). We will demonstrate that for a viscoelastic binary mixture, while the oscillatory-I mode is more universal, the oscillatory-II instability can also get dominant in the system under appropriate model parameter values.

Figure 4.4 plots the neutral stability curves as well as the corresponding oscillation frequencies for the oscillatory-I mode. The solid and the dash-dotted lines represent here the stability margin for a deformable free surface, while their adjacent dotted lines depict the stability boundary for a non-deformable free surface.

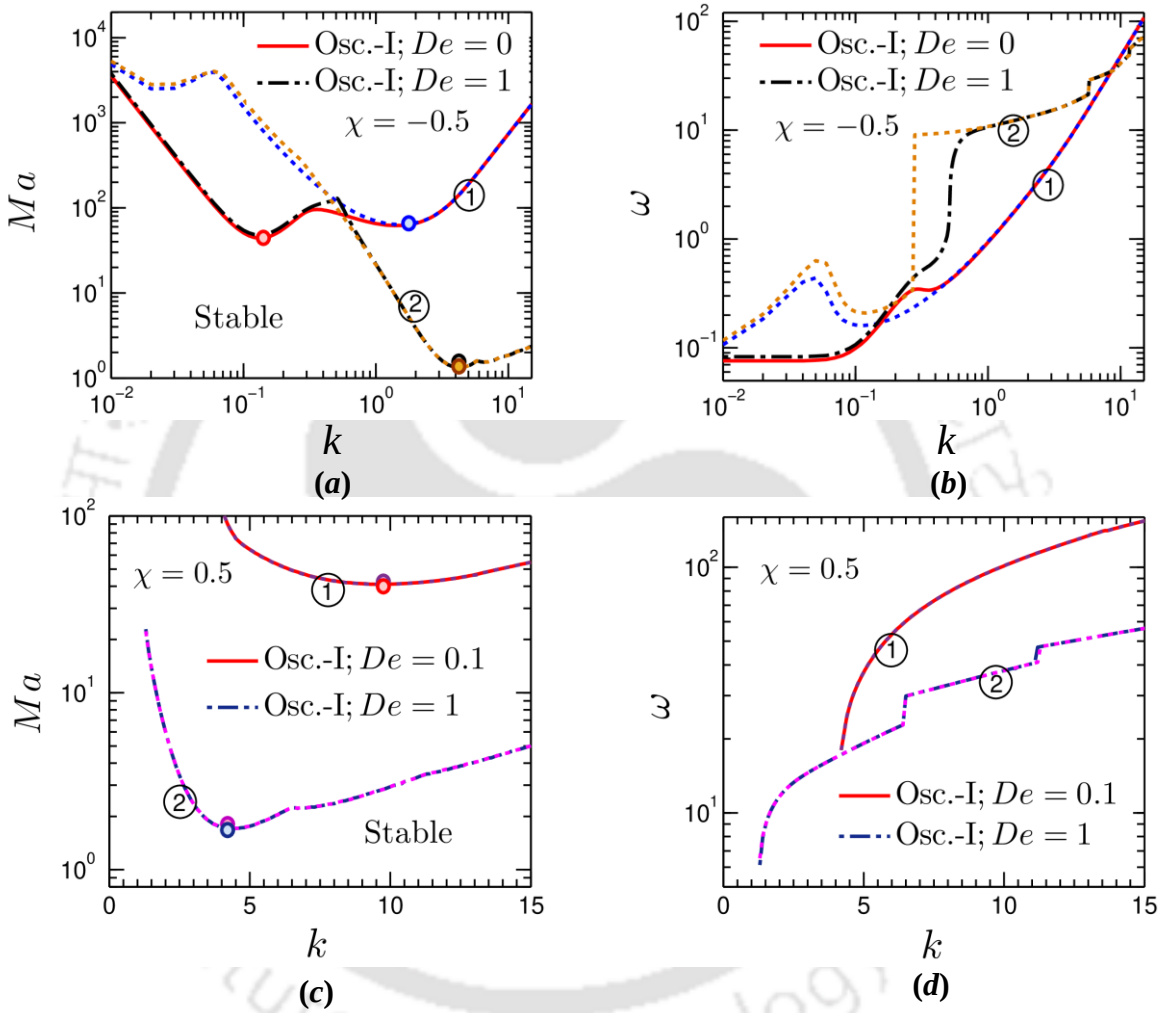

Figure 4.4: (*a*,*c*) Neutral stability curves $Ma(k)$, and (*b*,*d*) the corresponding oscillation frequency ω for oscillatory-I instability mode for $\chi < 0$ $(=-0.5)$ and $\chi > 0$ $(=0.5)$ respectively. For (*a*,*b*): lines marked by 1 and 2 corresponds to $De = 0$ and $De = 1$ respectively; for (*c*,*d*): lines marked by 1 and 2 corresponds to $De = 0.1$ and $De = 1$ respectively. In each panel, the solid and the dash-dotted lines depict the results for a deformable free surface $(Ga, \Sigma) = (0.1, 10^3)$; the adjacent dotted lines represents the results for a non-deformable free surface $(Ga, \Sigma) \to \infty$. The dot (o) mark on each neutral curve denotes the critical point (or the global minimum) of the curve. Other parameters: $Bi = 0.1$, $Le = 0.01$, $Pr = 10$.

Panel (*a*) demonstrates that for $\chi < 0$, the neutral curves consist of two branches, each characterized by a distinct local minimum. Of these two minima, while one resides in the long-wave regime $(k_c < O(1))$, other lies in the short-wave regime $(k_c \gtrsim O(1))$. Accordingly, we call these branches as the long-wave and short-wave branch, respectively. It can be clearly seen that, for the long-wave branch, Ma_c is a strong function of the deformability of free surface. Similar to the monotonic mode, a reduced free surface deformability enhances the stability of the system against the long-wave oscillatory-I disturbances as well. However, the onset of these disturbances essentially remains unaffected by the elastic behavior of the liquid as can be seen from panel *a* (the long-wave branch for $De = 0$ and 1 merge into a single curve). On the other hand, Ma_c for the short-wave branch is not influenced by the deformability of free surface, but governed by the elasticity of the mixture. An increased elasticity of the liquid substantially promotes here the onset of instability in the system. This suggests that depending on the free surface deformability and the elasticity level of the liquid, either of the long-wave or short-wave branches can hold the position of global minimum (shown by the marker "o" on each neutral curve in panel *a*). In other words, the oscillatory-I disturbances can emerge both in the long-wave and short-wave form for $\chi < 0$.

Panel (*c*) shows that for $\chi > 0$, the long-wave branch disappears, leaving only the short-wave branch. In particular, in this regime of χ, the oscillatory-I disturbances are found only for $De > 0$. This indicates that the emergence of short-wave oscillatory-I instability for $\chi > 0$ is a sole manifestation of the elastic behavior of the liquid. Similarly to the case $\chi < 0$, the stability threshold remains unaltered by the deformability of free surface but diminishes drastically with the increasing elasticity of the mixture.

The oscillation frequency ω of the neutral perturbations corresponding to each neutral curve of panels (*a*,*c*) is plotted in panels (*b*,*d*). The deformability of free surface controls ω only in the long-wave regime, whereas, ω is primarily modulated by the elasticity of the liquid in the short-wave regime. It should be further noted that although the $\omega(k)$ variation is smooth in the long-wave regime, discontinuity appears in the short-wave regime (in particular at higher values of *De*). In the neighbourhood of such points of discontinuity, a sudden change in the gradient of *Ma*(*k*) neutral curve occurs as can be observed from panels (*a*,*c*). Similar features of the neutral curves have been previously

reported by [73,106] in the context of pure thermocapillary driven convection in a viscoelastic film.

It is now clear that for $\chi < 0$, the oscillatory-I disturbances can develop both in the Newtonian and viscoelastic binary mixtures. However, the elasticity of the liquid significantly influences the onset of this particular instability mode in the system. To illustrate this elasticity-based transition of the stability picture, we plot in Fig. 4.5 the critical Marangoni number, Ma_c, the corresponding wavenumber, k_c, and the oscillation frequency, ω_c as functions of Deborah number, De for both the cases of deformable (solid line) and non-deformable (dotted line) free surface. It is to be noted that Ma_c refers here to the global minimum of oscillatory-I neutral curve. Two regimes are clearly distinguishable from the variations depicted by Fig. 4.5: a weakly elastic regime (for $De \lesssim 0.1$) wherein the stability behavior resembles that of a Newtonian binary liquid (at least for bifurcation around the conductive base state), and a strong elastic regime (for $De > 0.1$) where the elasticity of the liquid governs the stability threshold and the critical parameters (k_c, ω_c). The transition between these two regimes is marked by sharp discontinuities in k_c and ω_c (indicated by the arrow mark in panels *b*,*c*).

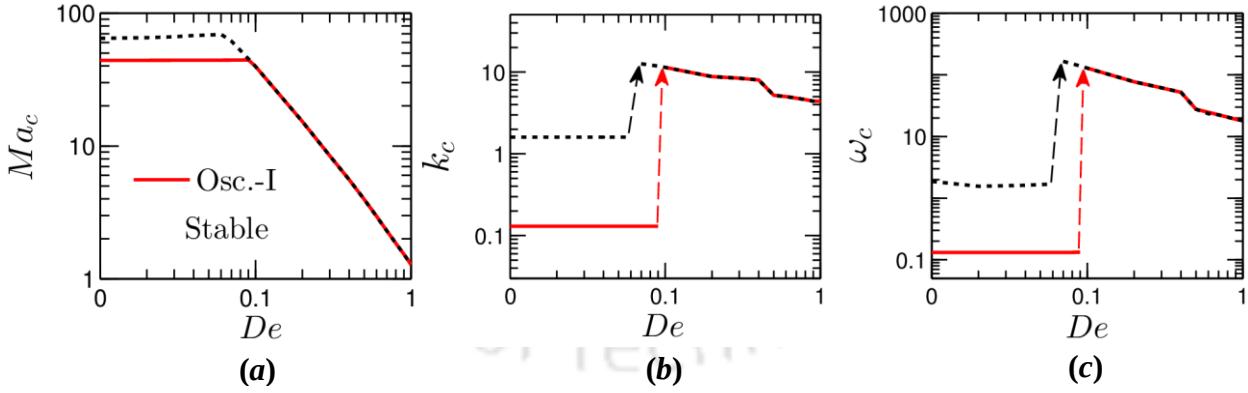

Figure 4.5: Variation of the (*a*) critical Marangoni number Ma_c, and the corresponding critical (*b*) wavenumber k_c, and (*c*) oscillation frequency ω_c with Deborah number De for the oscillatory-I instability mode for $\chi < 0$. The solid line depicts the variation for a deformable free surface $(Ga, \Sigma) = (0.1, 10^3)$; and the dotted one for a non-deformable surface $(Ga, \Sigma) \to \infty$. The arrow marks in panels (*b*,*c*) illustrate a switchover in the instability behavior with the increasing elasticity of the liquid. Other parameters: $Bi = 0.1$, $Le = 0.01$, $\chi = -0.5$.

A key observation from Fig. 4.5 is that, in the weakly elastic regime, while the critical parameters (Ma_c, k_c, ω_c) are governed by the deformability of free surface rather than the elasticity of the liquid, the opposite is true for the highly elastic regime. Panel (*a*) shows that the reducing deformability of free surface dampens the onset of oscillatory-I instability for $De \lesssim 0.1$. The resulting disturbances emerge in the long-wave form ($k_c \approx 0.1$) for a deformable free surface and the short-wave form ($k_c \approx 1$) in case of a non-deformable free surface (panel *b*). On the other hand, for a highly viscoelastic mixture ($De > 0.1$), irrespective of the free surface deformability, the disturbances always set in the short-wavelength form. An inverse variation of the parameters (Ma_c, k_c, ω_c) with *De* in this regime suggests that, for the enhanced elasticity of the binary mixture, the conductive state is more likely to bifurcate to the short-wave oscillatory-I mode with a more easily detectable convective pattern.

Another interesting feature presented by Fig. 4.5 is that, for $De \approx 0.1$ (*i.e.*, the boundary separating the weakly and highly elastic regime for a liquid layer with a deformable free surface), Ma_c for the onset of long-wave and short-wave oscillatory-I perturbations coincide. Therefore, a competition between the respective instability modes can take place in the system for $(De, Ga, \Sigma) \approx (0.1, 0.1, 10^3)$.

4.4.2 The role of thermocapillary and solutocapillary effects

In this subsection, we investigate the contributions of thermocapillary and solutocapillary forces on the development of instabilities in the system. This is done by plotting the neutral stability curves for monotonic and oscillatory modes at different values of χ. It is to be noted that $\chi = 0$ refers in this analysis to the case of purely thermocapillary driven convection. Figure 4.6(*a*) shows that the domain of stability reduces substantially as χ increases from zero. This suggests that both thermocapillary and solutocapillary forces play a destabilizing role in the emergence of monotonic instability for $\chi > 0$. However, k_c for this instability mode is not decided by the solutal effects (at least for a deformable surface, the case of non-deformable surface will be discussed in Fig. 4.7). Although not shown here graphically, this particular instability mode can appear even for $\chi < 0$, within a narrow interval of χ. This range will be identified in Section 4.5, perfor-

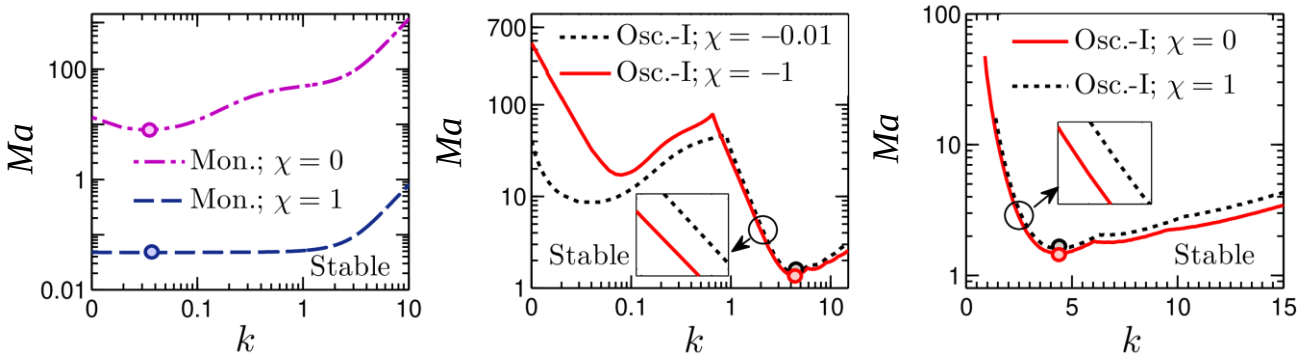

(*a*) **(*b*)** **(*c*)**

Figure 4.6: Neutral stability curves $Ma(k)$ for the monotonic and oscillatory–I modes in the (*a*,*c*) positive, and (*b*) negative Soret number χ domains. The long-wave branch for the oscillatory-I mode emerges only when $\chi<0$. The dot (○) mark on each neutral curve represents the critical point of the curve. Other parameters: $Bi=0.01$, $De=1$, $Le=10^{-3}$, $Ga=0.1$, $\Sigma=10^{3}$.

ming a long-wave asymptotic analysis of the problem.

Figure 4.6(*b*) demonstrates that for the long-wave branch of oscillatory-I mode, solutocapillary acts stabilizing, while thermocapillary turns into the destabilizing mechanism. Such opposite contributions of the driving forces give rise to the long-wave oscillatory-I perturbations in the system. On the other hand, thermocapillarity, coupled with the elasticity of the liquid, primarily give rise to the short-wave disturbances. Solutocapillarity provides here only a small correction to the stability margin. Interestingly, for this short-wave branch, an increasing $|\chi|$ in the range $\chi<0$ weakly destabilizes the system, whereas increment in χ for $\chi>0$ leads to a mild stabilization of the system as can be observed from the inset of Figs. 4.6(*b*,*c*).

Figure 4.7 plots the variations of critical Marangoni number Ma_c and the corresponding wavenumber k_c with χ for both the cases of a deformable and non-deformable free surface. Clearly, an increasing $\chi(>0)$ leads to a strong destabilization of the system with respect to the monotonic disturbances. It should be noted that, for this instability mode, although the deformability of free surface weakly influences the stability threshold (this is not even perceptible in the scale of Fig. 4.7*a*); nevertheless, it plays a vital role in determining the size of the convection cells. In Fig. 4.7(*b*) one can see that $k_{c,(Ga,\Sigma)\to\infty} > k_{c,(Ga,\Sigma)=(0.1,10^3)}$, implying a highly deformable free surface allows the

formation of much larger sized stationary convective patterns compared to its non-deformable counterpart.

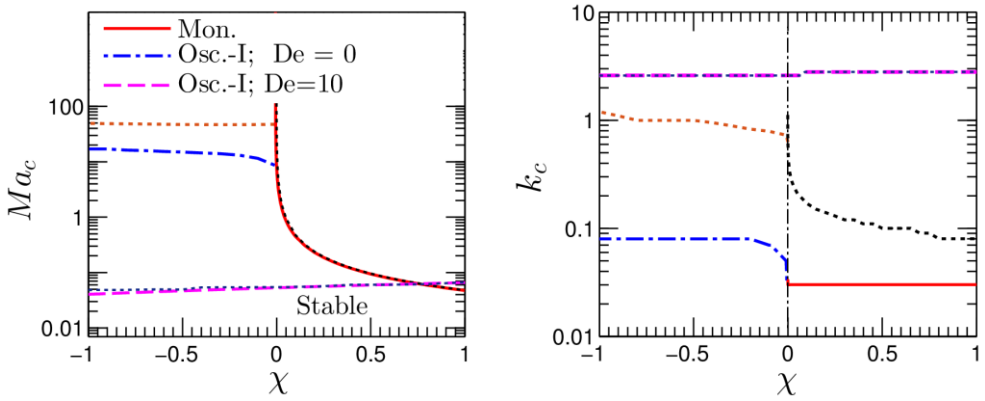

(*a*) **(*b*)**

Figure 4.7: Variation of the (*a*) critical Marangoni number Ma_c, and the corresponding (*b*) critical wavenumber k_c with χ. In each panel, the solid, dash-dotted, and dashed lines represent the variations for a deformable free surface $(Ga, \Sigma) = (0.1, 10^3)$. The dotted lines adjacent to each instability mode represent the variations for a non-deformable free surface $(Ga, \Sigma) \to \infty$. Other parameters: $Bi = 0.01$, $Le = 10^{-3}$.

For the oscillatory-I mode, Fig. 4.7(*a*) shows that an increasing $|\chi|$ augments the stability region for a Newtonian binary liquid film having a deformable free surface. However, in the case of a non-deformable free surface (or for a highly viscoelastic mixture irrespective of the free surface deformability), the stability thresholds are found to remain nearly independent of χ. In this regard, it is important to observe in Fig. 4.7(*b*) that, for a Newtonian binary mixture with a deformable surface k_c lies in the long-wave regime, whereas, for a non-deformable surface (or, for a highly viscoelastic mixture) k_c resides in the short-wave regime. The fact that solutocapillary effect is dominant only in the long-wave regime thus explains the variations in Fig. 4.7(*a*).

Before concluding this subsection, an additional remark about Fig. 4.7(*a*) is necessary. At the intersection point between the neutral curves for monotonic and oscillatory-I modes, $Ma_{c,mon.} = Ma_{c,osc.\text{-}I}$. Therefore, a competition between the respective instability modes can occur for χ values corresponding to this point. Now, for $De > 0$ since the oscillatory-I disturbances can appear for any $\chi \in \mathbb{R}$, and as their onset gets

triggered by the increasing elasticity of the liquid, the neutral curve for the monotonic mode presented in Fig. 4.7(*a*) is essentially the locus of codimension-two bifurcation points. Towards the left of this curve, the conductive state bifurcates into the oscillatory-I mode, while a steady bifurcation (*i.e.*, monotonic instability) takes place on to its right.

4.4.3 The role of thermal and solutal diffusivities

Let us now discuss the influence of thermal and solute diffusivities on the onset of instability in the system. Here, we will demonstrate that a different kind of oscillatory instability (*i.e.*, oscillatory-II) can emerge in the liquid layer based on the diffusivity ratio $Le(=D/\alpha)$. Before that, we first investigate the role played by *Le* on the emergence of oscillatory-I disturbances.

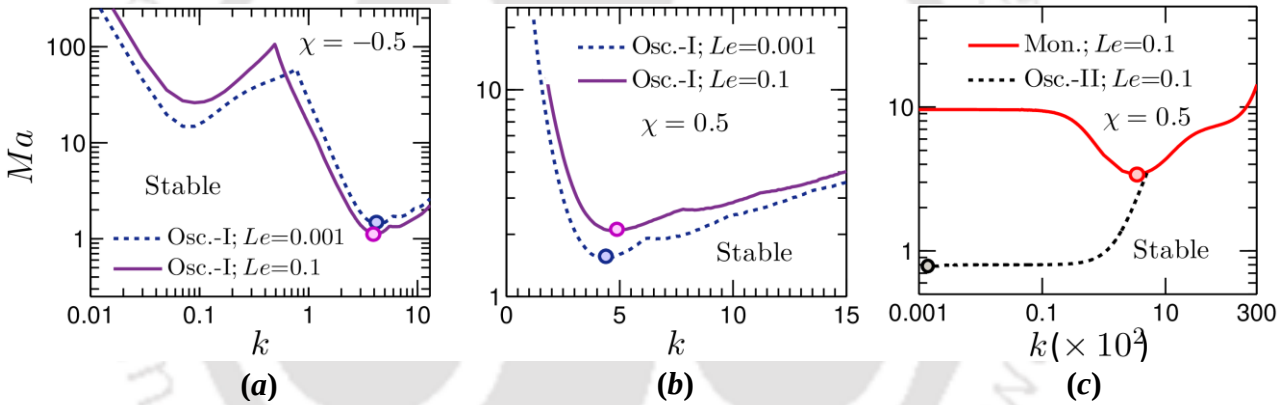

Figure 4.8: Effect of Lewis number *Le* on the monotonic and oscillatory instability threshold for (*a*,*c*) $\chi<0(=-0.5)$, and (*b*) $\chi>0(=0.5)$. The dot (o) mark on each neutral curve represents the critical point of the curve. Panel (*c*) shows that for a deformable free surface at higher value of *Le*, a different type of long-wave oscillatory instability (oscillatory-II) can emerge in the fluid layer. Other parameters: $Bi=0.01$, $De=1$, $Ga=0.1$ and $\Sigma=10^3$.

Figure 4.8(*a*) shows that an increased solute diffusivity corresponding to higher values of *Le* enhances the stability of the system against the long-wave oscillatory-I disturbances. This is due to the stabilizing role of solutocapillarity in producing this instability mode. Similarly, a destabilizing (stabilizing) solutocapillary force for $\chi<0$ $(\chi>0)$ in the short-wave regime leads to a reduction (enhancement) in the stability threshold for higher solute diffusivity (cf. Figs. 8*a*,*b* with Figs. 6*b*,*c*).

Figure 4.8(*c*) shows that for a sufficiently large *Le* ($\gtrsim O(10^{-2})$), the oscillatory-II disturbances can emerge in systems with a deformable free surface. Notably, at higher values *k*, the neutral curve for this particular instability mode (the dotted line) merges with the neutral curve for the monotonic mode (the solid line). This limits the appearance of oscillatory-II disturbances only in the long-wave form.

The other features of this instability mode are also quite different from the oscillatory-I mode. First, while the oscillatory-I instability can emerge in the system for the entire permissible range of model parameters, the oscillatory-II instability appears only in case of a deformable free surface, for $\chi > 0$ and $Le \gtrsim O(10^{-2})$. Although not shown here graphically, such disturbances get damped with the reducing deformability of free surface and eventually disappears in a non-deformable free surface. Second, the

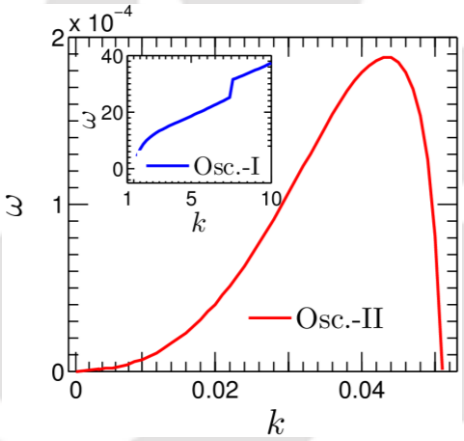

Figure 4.9: Comparison of the oscillation frequency of neutral perturbations for oscillatory–II mode with oscillatory–I mode (shown in the inset). $\chi = 0.5$, $Bi = 0.01$, $De = 1$, $Le = 0.1$, $Ga = 0.1$, $\Sigma = 10^3$.

oscillation frequency of the oscillatory-II mode is several orders of magnitude smaller than that of the oscillatory-I mode (compared in Fig. 4.9). This suggests that the oscillatory-II perturbations develop with a significantly large oscillation period compared to the oscillatory-I disturbances.

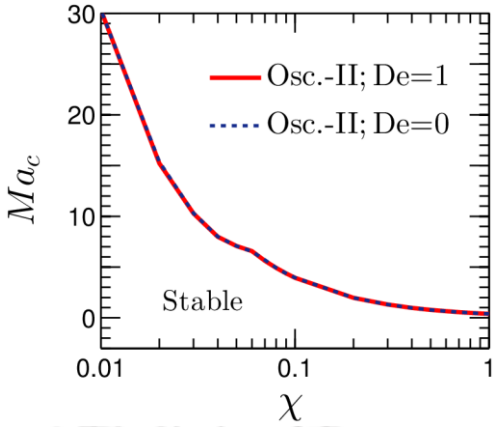

Figure 4.10: Variation of the critical Marangoni number Ma_c with χ for the oscillatory–II mode at $Bi = 0.01$, $Le = 0.1$, $Ga = 0.1$, $\Sigma = 10^3$. No oscillatory–II instability emerges for $\chi \le 0$.

Now, in order to understand the physical mechanism behind the origination of the oscillatory-II disturbances and to elucidate the role of liquid elasticity on their onset, we plot in Fig. 4.10 the variation of $Ma_c(\chi)$ with De for this instability mode. The disappearance of these disturbances for purely thermocapillary driven convection ($Ma_c \to \infty$ as $\chi \to 0$) and the reduction of Ma_c with χ suggests that the competition between stabilizing thermocapillary and destabilizing solutocapillary forces give rise to the oscillatory-II mode. A shorter mass diffusion time scale (H^2/D) is essential here to overcome the stabilizing action of thermocapillary by the destabilizing solutocapillary force. This explains the reason behind the emergence of oscillatory-II instability only for higher values of $Le\left(=\frac{H^2}{\alpha}\Big/\frac{H^2}{D} \gtrsim O(10^{-2})\right)$. Another key observation from Fig. 4.10 is that the $Ma_c(\chi)$ neutral curves for different values of $De(=0 \text{ and } 1)$ collapse into a single curve. This implies that the stability threshold for the oscillatory-II mode is not affected by the elastic behavior of the binary mixture.

4.4.4 The role of heat transfer rate at the free surface

Lastly, we discuss the role of the Biot number on the stability threshold of the system. In Fig. 4.11, the neutral stability curves for each instability mode are plotted for two different values of Bi ($=10^{-3}$ and 0.1). It turns out that at higher values of Bi, the enhanced

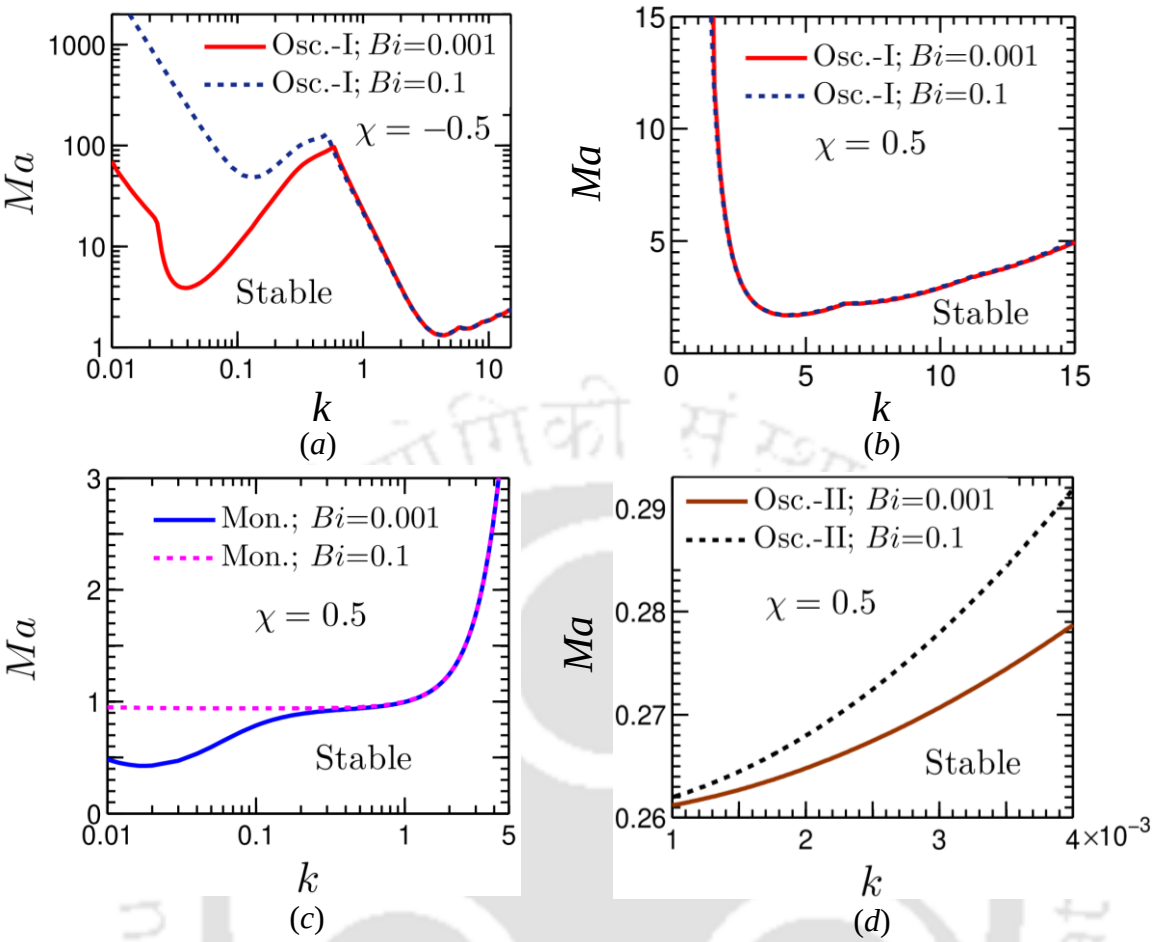

Figure 4.11: Effect of Biot number *Bi* on the monotonic and oscillatory instability threshold for (a) $\chi < 0 (= -0.5)$, and (b,c,d) $\chi > 0 (= 0.5)$ for a film with deformable free surface $(Ga, \Sigma) = (0.1, 10^3)$. Other parameters: $De = 1$, $Le = 0.01$.

heat transfer rate from the free surface increases the stability of the system against the long-wave disturbances. However, the influence of *Bi* is less significant in the short-wave regime, as reflected by the saturation of curves in this regime. The magnitude of *Bi*, therefore, bears significant importance in the emergence of long-wave instability in the liquid layer.

4.5 An Approximate Model

In this section, we derive an approximate model by performing long-wave asymptotic expansion of the EVP and rescaling the parameters (Bi, De, Σ). This model can be helpful in getting a qualitative insight into the stability picture without numerically solving the

problem.

In the long-wavelength limit, given the very small ratio between mean film thickness H and disturbance wavelength ℓ (*i.e.* $\varepsilon = H/\ell \ll 1$), the horizontal variations evolve much slowly compared to the vertical ones. Here, we can apply the lubrication approximation, consisting of slow longitudinal $X \sim \varepsilon x$ and temporal $\mathcal{T} \sim \varepsilon^2 t$ variables. We, therefore, proceed with introducing the following scaling for k and λ:

$$k = \varepsilon q\,, \quad \lambda = \varepsilon^2 \lambda_o\,. \tag{4.27a,b}$$

Furthermore, for this analysis, we rescale the parameters *Bi*, *De* and Σ as

$$Bi = \varepsilon^2 \mathcal{B}\,, \quad De = \varepsilon^{-2} \mathcal{D}e\,, \quad \Sigma = \varepsilon^{-2} Ca\,. \tag{4.28a-c}$$

However, we do not impose any restrictions on the magnitude of other dimensionless parameters, and they remain at $O(1)$ with respect to ε.

The perturbation fields are now expanded for ε as follows:

$$\bar{\psi} = \varepsilon\psi_o + \varepsilon^3\psi_2 + \ldots\,,\ \ \bar{\theta} = T_o + \varepsilon^2 T_2 + \ldots\,,\ \ \bar{c} = c_o + \varepsilon^2 c_2 + \ldots\,,\ \ \bar{\xi} = \xi_o + \varepsilon^2\xi_2 + \ldots\ . \tag{4.29a-d}$$

Introducing the rescaled parameters and expansions into the EVP (4.24 – 4.26), we first collect the terms with identical order in ε. At the leading order, the governing Eqs. 4.24(*a-c*) simplify to

$$\frac{d^4\psi_o}{dz^4} = 0\,, \quad \frac{d^2 T_o}{dz^2} = 0\,, \quad \frac{d^2 c_o}{dz^2} = 0\,; \tag{4.30a-c}$$

and accompanied by the following set of boundary conditions:

$$\psi_o = 0\,, \quad \frac{d\psi_o}{dz} = 0\,, \quad \frac{dT_o}{dz} = 0\,, \quad \frac{dc_o}{dz} = 0 \quad \text{at } z = 0\,, \tag{4.31a-d}$$

$$iq\psi_o = \lambda_o \xi_o\,, \quad \frac{dT_o}{dz} = 0\,, \quad \frac{dc_o}{dz} = 0\,, \tag{4.32a-c}$$

$$\frac{d^3\psi_o}{dz^3} = iq\xi_o\left(Ga + Ca\,q^2\right)\left(1 - \lambda_o \mathcal{D}e\right), \tag{4.32d}$$

$$\frac{d^2\psi_o}{dz^2} = iqMa\left(1 - \lambda_o \mathcal{D}e\right)\left(c_o - T_o + \xi_o + \chi\xi_o\right) \quad \text{at } z = 1. \tag{4.32e}$$

The solutions to the BVP (4.30 – 4.32) is given by

$$\psi_o = \frac{i\xi_o}{6q}\left[q^2\left(Ga + Ca\,q^2\right)\left(1 - \lambda_o \mathcal{D}e\right)\left(z^3 - z^2\right) - 6\lambda_o z^2\right], \quad T_o = \mathcal{J}\,, \quad c_o = \wp\,, \tag{4.33a-c}$$

where $\mathcal{J}$ and $\wp$ are constants yet to be determined.

At the second order with respect to ε, only the energy and mass balance equations find relevance. They read

$$\frac{d^2T_2}{dz^2}+\left(\lambda_o-q^2\right)T_o=iq\psi_o, \tag{4.34a}$$

$$Le\frac{d^2c_2}{dz^2}+\left(\lambda_o-Le\,q^2\right)c_o=-i\chi\left(1+Le\right)q\psi_o+Le\chi\lambda_o T_o. \tag{4.34b}$$

The associated boundary conditions (4.25*c*,*d*) and (4.26*b*,*c*) now take the following form

$$\frac{dT_2}{dz}=0,\quad \frac{dc_2}{dz}=0 \quad \text{at} \quad z=0, \tag{4.35}$$

$$\frac{dT_2}{dz}=-\mathcal{B}\left(T_o-\xi_o\right),\quad \frac{dc_2}{dz}=\chi\mathcal{B}\left(T_o-\xi_o\right) \quad \text{at } z=1. \tag{4.36}$$

Integrating Eqs. 4.34(*a*,*b*) across the film $0\le z\le 1$ and incorporating the boundary conditions (4.35) – (4.36), we obtain

$$\xi_o=\frac{72\left(\phi+q^2\right)}{72\mathcal{B}-24\lambda_o-\mathcal{G}\mathcal{Q}q^2}\mathcal{J}, \tag{4.37}$$

$$\varphi=\frac{\chi\phi\left(72\mathcal{B}-24\lambda_o-\mathcal{G}\mathcal{Q}q^2\right)+\left[\chi\left(1+Le^{-1}\right)\left(24\lambda_o+\mathcal{G}\mathcal{Q}q^2\right)-72\mathcal{B}\chi\right]\left(\phi+q^2\right)}{\left(72\mathcal{B}-24\lambda_o-\mathcal{G}\mathcal{Q}q^2\right)\left(q^2-\lambda_o Le^{-1}\right)}\mathcal{J}, \tag{4.38}$$

where $\phi=\mathcal{B}-\lambda_o$, $\mathcal{G}=\left(1-\lambda_o\mathcal{D}e\right)$ and $\mathcal{Q}=Ga+Ca\,q^2$.

Finally, the substitution of ξ_o and φ into the tangential stress balance boundary condition (4.32*e*) yields the following sought expression for *Ma*:

$$Ma=\frac{24}{q^2}\frac{\mathcal{N}_0+\lambda_o\mathcal{N}_1+\lambda_o^2\mathcal{N}_2+\lambda_o^3\mathcal{N}_3}{\mathcal{D}_0+\lambda_o\mathcal{D}_1+\lambda_o^2\mathcal{D}_2+\lambda_o^3\mathcal{D}_3}, \tag{4.39}$$

the coefficients $\mathcal{N}_j$ and $\mathcal{D}_j$ $\left(j=0-3\right)$ are defined in Appendix C.1.

Equation 4.39 governs the stability threshold for both the monotonic and oscillatory disturbances within the approximations made in Eqs. 4.27 – 4.28. The validity bound for this analysis will be discussed in the forthcoming subsections. An inspection of Eq. 4.39 reveals that, in accordance with the numerical results presented in Section 4.4, the stability threshold for both the instability modes are independent of *Pr*.

4.5.1 Monotonic mode

Let us start with the case of monotonic instability. Substitution of $\lambda_o = 0$ in Eq. 4.39 yields the explicit expression of the neutral stability curve for this instability mode:

$$Ma_{mon.} = \frac{48Le\mathcal{Q}\left(\mathcal{B}+q^2\right)}{\mathcal{B}\chi\mathcal{Q}+\left[\mathcal{Q}\chi+Le\left(72+\mathcal{Q}\right)\left(1+\chi\right)\right]q^2}. \tag{4.40}$$

Returning to the unscaled parameters *k*, *Bi* and Σ, we get

$$Ma_{mon.} = \frac{48Le\left(Ga+\Sigma k^2\right)\left(Bi+k^2\right)}{Bi\chi\left(Ga+\Sigma k^2\right)+\left[\chi\left(Ga+\Sigma k^2\right)+Le\left(1+\chi\right)\left(72+Ga+\Sigma k^2\right)\right]k^2}. \tag{4.41}$$

Equation (4.41) depicts the stability boundary for a system with deformable free surface. For a non-deformable surface (*i.e.*, in the limit $(Ga+\Sigma k^2)\to\infty$), the stability margin becomes

$$Ma_{mon.} = \frac{48Le\left(Bi+k^2\right)}{Bi\chi+\left(Le+\chi+Le\chi\right)k^2}. \tag{4.42}$$

The minimization of Eq. 4.41 for *Ma* now yields the following expression for critical wavenumber k_c

$$k_c = \sqrt{\frac{BiGa\Sigma+\sqrt{72BiGa\Sigma\left(72+Ga-Bi\Sigma\right)}}{\Sigma\left(72-Bi\Sigma\right)}} \quad \text{for } \chi\neq -1. \tag{4.43}$$

Interestingly, Eq. 4.43 also indicates the validity domain of this approximate model. It is important to note that for $Bi\Sigma = 72$, $k_c\to\infty$, violating the lubrication approximation $k<<1$. Therefore, the proposed model holds good only for $Bi\Sigma<72$. This event is graphically demonstrated in Fig. 4.12. One can readily see that the critical parameters (Ma_c, k_c) predicted by the long-wave theory agree with the numerical results only for $Bi\Sigma = 10(<72)$ (*i.e.*, for a deformable free surface, as can be seen in panel *a*).

Equations 4.41 and 4.42 indicate that at $k\to\infty$, irrespective of the deformability of free surface, *Ma* attains the limiting value

$$Ma_{mon.,k\to\infty} = \frac{48Le}{Le+\chi+Le\chi}. \tag{4.44}$$

It should be noted that for $Bi\Sigma \geq 72$, $Ma \to Ma_c$ in Eq. 4.44. However, this Ma_c lost the quantitative agreement with the numerical results owing to the violation of long-wave approximation. A comparison between panels *a* and *b* of Fig. 4.12 reveals this.

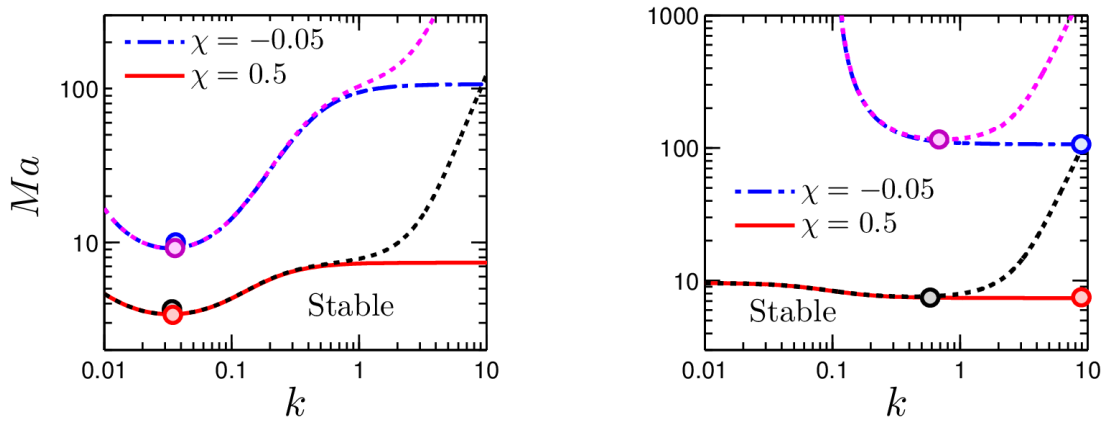

Figure 4.12: Comparison of results obtained from the approximate model (solid and dash-dotted lines) with the numerical results (dotted lines) for the monotonic instability mode via the neutral stability curve (*a*) deformable surface $(Ga, \Sigma) = (0.1, 10^3)$, (*b*) non-deformable surface $(Ga, \Sigma) \to \infty$. The dot (o) mark on each neutral curve represents the critical point of the curve. Other parameters: $Bi = 0.01$, $Le = 0.1$.

From Eqs. 4.41 – 4.42 it further follows that for $k \in [0, \infty)$, irrespective of the deformability of free surface, *Ma* remains positive for $\chi > 0$ and becomes negative when $\chi < -Le/(1+Le)$. Hence, there must be a discontinuity in the neutral curves in the domain $0 > \chi > -Le/(1+Le)$, suggesting the emergence of instability for heating from the top as well as from below. For the case of a deformable free surface, this point of discontinuity (k_d) is given by the real and positive root of

$$\gamma_0 k_d^4 + \gamma_1 k_d^2 + \gamma_2 = 0, \tag{4.45}$$

the coefficients γ_j ($j = 0 - 2$) are presented in Appendix C.2.

On the other hand, for a non-deformable surface, the point of discontinuity (k_d^{nd}) lies at

$$k_d^{nd} = \sqrt{-\frac{Bi\chi}{Le + \chi + Le\chi}}, \tag{4.46}$$

Thus, for $\chi \in (0, -Le/1+Le)$, the monotonic instability sets in for heating the liquid layer from below with $k > k_d$ (or k_d^{nd} for a non-deformable surface) and vice versa. For the parameter values $(Le, \chi) = (0.1, -0.05)$ this situation is graphically illustrated in Fig. 4.12. Here, $k_d = 2.8\times10^{-3}$ and $k_d^{nd} = 0.105$. A comprehensive study of the stability characteristics of the branch pertaining to the negative values of *Ma* is studied in Chapter 5.

Finally, a few previously reported results in the literature can be derived from the expressions (4.41) and (4.42). Since the monotonic instability threshold remains unaffected by the elastic behavior of the liquid; therefore, in the limit $\chi = 0$, Eq. 4.41 yields the results for purely thermocapillary driven convection in a Newtonian liquid layer [55]. For such a film, Eq. 4.42 yields the well-known asymptotic $Ma_{mon.} = 48$ in the limit $(Ga, \Sigma) \to \infty$, either for $Bi = 0$ or $k \to \infty$ [11].

4.5.2 Oscillatory mode

The stability threshold for this instability mode is obtained by substituting $\lambda_o = i\omega$ in Eq. 4.39. This yield

$$Ma_{\pm osc.} = \frac{\left(\mathcal{N}_0 - \omega_\pm^2 \mathcal{N}_2\right)\left(\mathcal{D}_0 - \omega_\pm^2 \mathcal{D}_2\right) + \omega_\pm^2\left(\mathcal{N}_1 - \omega_\pm^2 \mathcal{N}_3\right)\left(\mathcal{D}_1 - \omega_\pm^2 \mathcal{D}_3\right)}{\left(\mathcal{D}_0 - \omega_\pm^2 \mathcal{D}_2\right)^2 + \omega_\pm^2\left(\mathcal{D}_1 - \omega_\pm^2 \mathcal{D}_3\right)^2}, \quad (4.47)$$

where $\omega_\pm = (\omega_+, \omega_-)$ are the oscillation frequencies for $Ma_{\pm osc.} = (Ma_{+osc.}, Ma_{-osc.})$ respectively and given by

$$\omega_\pm^2 = \frac{1}{2\left(\mathcal{N}_3\mathcal{D}_2 - \mathcal{N}_2\mathcal{D}_3\right)}\Big[\left(\mathcal{N}_1\mathcal{D}_2 + \mathcal{N}_3\mathcal{D}_0 - \mathcal{N}_2\mathcal{D}_1 - \mathcal{N}_0\mathcal{D}_3\right) \pm\sqrt{\left(\mathcal{N}_2\mathcal{D}_1 + \mathcal{N}_0\mathcal{D}_3 - \mathcal{N}_1\mathcal{D}_2 - \mathcal{N}_3\mathcal{D}_0\right)^2 - 4\left(\mathcal{N}_3\mathcal{D}_2 - \mathcal{N}_2\mathcal{D}_3\right)\left(\mathcal{N}_1\mathcal{D}_0 - \mathcal{N}_2\mathcal{D}_3\right)}\Big]. \quad (4.48)$$

Here ω_+^2 (ω_-^2) refers to the oscillation frequency obtained from adding (subtracting) the square root terms in the numerator of Eq. 4.48. For a given set of model parameters $(\mathcal{B}, Ca, \mathcal{D}e, Ga, Le, \chi)$, the presence of two different oscillation frequencies (*i.e.*, ω_+ and ω_-) suggests the possible emergence of two different oscillatory instabilities in the system (namely, oscillatory – I and oscillatory – II as discussed in Section 4.4). Confirming the numerical results, one of the oscillation frequencies vanishes for a non-

deformable surface (must be the one related with the oscillatory – II mode), for which the expressions of the neutral curve and oscillation frequency are given by

$$Ma_{osc.} = \frac{48\left(Bi + k^2 + Le\,k^2\right)}{\left[\left(1 + DeLe\,k^2\right) + \chi\left(1 + Bi\,De + De\,k^2 + DeLe\,k^2\right)\right]k^2}, \tag{4.49}$$

and

$$\omega^2 = \frac{\mathcal{L}_0 k^6 + \mathcal{L}_1 k^4 + \mathcal{L}_2 k^2 + \mathcal{L}_3}{\mathcal{L}_4 k^2 + \mathcal{L}_5}. \tag{4.50}$$

respectively. The coefficients $\mathcal{L}_j$ $(j = 0-5)$ are defined in Appendix C.3. It is worth noting that in the limit $De = 0$, Eq. 4.49 matches with the results for a Newtonian liquid [104].

Given the convoluted form of the neutral curves (4.47) and (4.49), any further analytical progress in estimating their validity bound now becomes a rather intricate task. Thus, we verify the accuracy of this analysis by comparing the results with numerical computations for a wide range of the parameters (De, Le, χ) within the limit $Bi\Sigma < 72$.

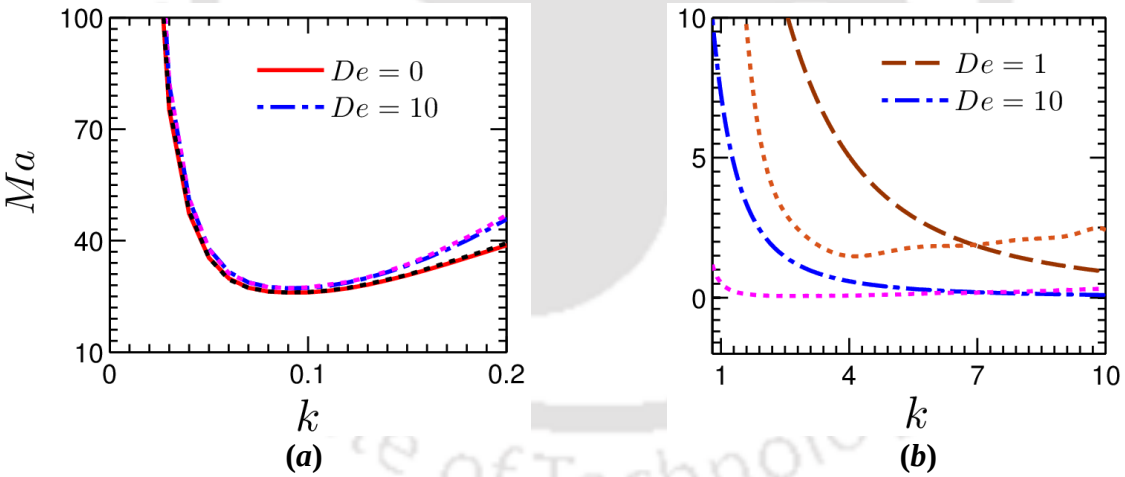

Figure 4.13: Comparison between results of the numerical computation (dotted lines) and the approximate model (solid and dash-dotted lines) for the oscillatory-I mode via neutral stability curve: (*a*) long-wave branch at $Le = 0.1$, $\chi = -0.5$ (*b*) short-wave branch at $Le = 10^{-3}$, $\chi = 0.5$. Other parameters: $Bi = 0.01$, $Ga = 0.1$, $\Sigma = 10^3$.

For the long-wave branch of oscillatory-I mode, Fig. 4.13(*a*) shows that the results obtained from the approximate model agree with the numerical results in an excellent manner for both the Newtonian $(De = 0)$ and highly viscoelastic $(De = 10)$ binary

mixture. Here, the oscillation frequency is given by ω_-. However, this agreement is poor for the short-wave branch, due to the violation of the lubrication approximation (shown in Fig. 4.13*b*). Nevertheless, the scaling adopted for *De* in Eq. 4.28(*b*) helps in achieving a qualitative agreement at higher values of *De*. The oscillation frequency for this branch is given by ω_+.

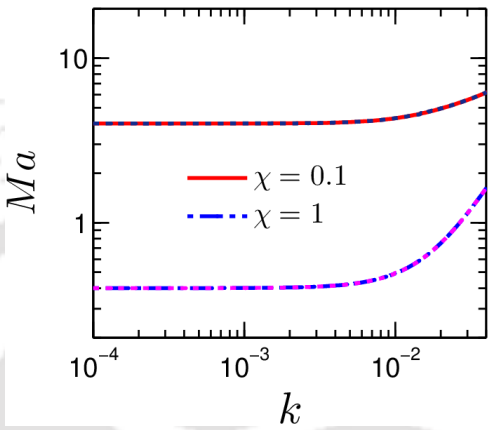

Figure 4.14: Comparison of results obtained from the approximate model (solid and dash-dotted lines) with the numerical results (dotted lines) for the oscillatory-II mode via the neutral stability curve at $Bi = 0.01,\ De = 1,\ Le = 0.1,\ Ga = 0.1,\ \Sigma = 10^3$.

Finally, this approximate model also predicts the emergence of oscillatory-II instability in the system. The oscillation frequency for this mode is given by ω_-. Figure 4.14 shows that the developed model is capable of depicting the stability threshold in a fairly accurate manner for this instability mode as well.

4.6 Phase Diagrams

We have now understood that both the monotonic and oscillatory instabilities can emerge in the present system (either in the long-wave or short-wave mode) depending on the values of model parameters. The purpose of this section is to explore the parameter regions for each instability mode, wherein it becomes dominant in the liquid layer. The phase diagrams displayed in Fig. 4.15 are expected to be helpful for carrying out an experimental investigation of the present problem, especially in situations where one is interested in observing the convective patterns of a particular instability mode. Since we are studying here the stability characteristics of a viscoelastic film incorporating the Soret

effect, the phase diagrams are plotted in the $\chi - De$ plane. In an effort to identifying the region of dominance for each instability mode, the parameter set (Ga, Σ, Le) is varied to take into account the surface deformability with weak/strong solute diffusivity. However, we hold the parameters $Bi(=0.01)$ and $Pr(=10)$ fixed. In panels (*a*-*d*) of Fig. 4.15, region-1 stands for the monotonic mode, region-2 for the long-wave oscillatory-I mode, region 3 for the short-wave oscillatory-I mode, and region-4 for the oscillatory-II mode.

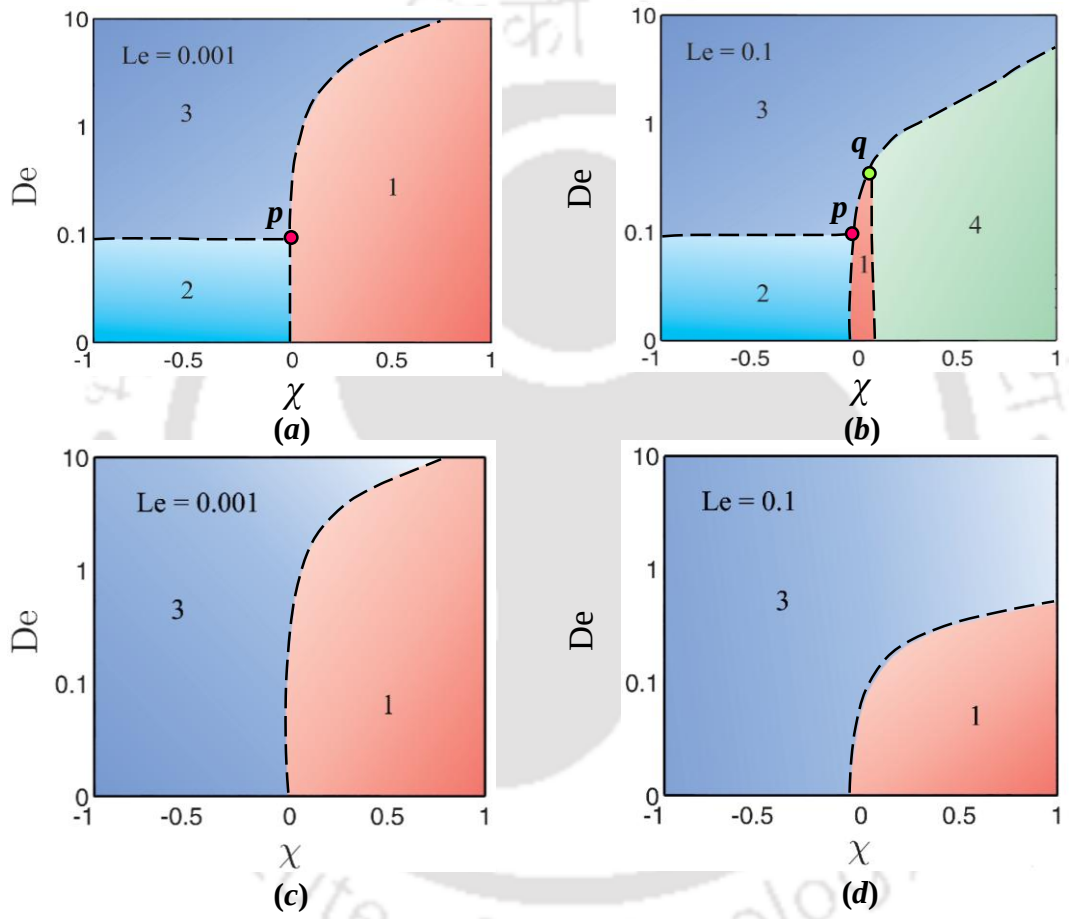

Figure 4.15: Phase diagrams for (χ, De) at different Le enclosing the regimes of dominant instability mode: (*a*,*b*) deformable free surface $(Ga, \Sigma) = (0.1, 10^3)$, and (*c*,*d*) non-deformable free surface $(Ga, \Sigma) \to \infty$ at $Bi = 0.01$, $Pr = 10$. In panels (*a*-*d*), regime-1: monotonic instability, regime-2: long-wave oscillatory–I instability, regime-3: short-wave oscillatory–I instability, regime-4: oscillatory –II instability. At the points marked ***p*** and ***q*** in panels (*a*,*b*), the three adjacent instability modes can coexist.

An important point that needs to be highlighted here is that a dataset in (χ, De) corresponding to the boundary between the adjacent instability modes refers to a

competition between them to become the dominant instability mode in the system. Such interaction between the instability modes may lead to the formation of convective patterns, which will be significantly different from the patterns that appear far from this location.

For a liquid layer with a deformable free surface, panels (*a*,*b*) plot the phase diagrams for two different values of *Le*: $Le = 10^{-3}$ and 0.1, respectively. Panel (*a*) shows that in the weakly viscoelastic regime (*i.e.*, $De \lesssim 0.1$), the long-wave oscillatory-I mode (region 2) becomes dominant for $\chi < 0$. The characteristics of this mode are identical for both the Newtonian and viscoelastic binary mixtures, as we have learned from Section 4.4. However, in the highly elastic regime (*i.e.*, for $De > 0.1$), this long-wave mode is replaced by its short-wave counterpart (region-3). Since the onset of this particular instability mode is triggered by the elasticity of the mixture (but weakly dominated by the solutocapillary force), the short-wave oscillatory-I mode can become dominant even for $\chi > 0$ at higher values of *De*. Except for such larger values of *De*, the monotonic instability (region-1) prevails in the system for $\chi > 0$ as well as for a narrow interval of $\chi < 0$ (as discussed in Section 4.5).

A comparison between panels (*a*) and (*b*) now reveals that for a viscoelastic mixture with higher solute diffusivity $(Le = 0.1)$, the region of dominant monotonic instability shrinks drastically, and the oscillatory-II instability (region-4) emerges in the system for $\chi > 0$. Furthermore, region-1 shifts slightly towards left (due to the widening up of range $\chi \in (0, -Le/Le+1)$, as derived in Section 4.5.1), and region-3 expands towards the right. However, the transition boundary between the long-wave oscillatory-I (region-2) and short-wave oscillatory-I (region-3) mode remains unaltered by the value of *Le*. Another key observation from panels (*a*,*b*) is that, for (χ, De) values corresponding to the points ***p*** and ***q***, three different instability modes, *viz*., monotonic:long-wave oscillatory-I:short-wave oscillatory-I and monotonic:long-wave oscillatory-II:short-wave oscillatory-I respectively, can compete together in the system.

For a non-deformable free surface, panels (*c*,*d*) demonstrate that irrespective of the diffusivity ratio *Le*, the conductive state bifurcates either to the monotonic (region-1) or the short-wave oscillatory-I (region-3) mode depending on the parameter set (χ, De). It

should be noted that the long-wave oscillatory mode (both oscillatory-I and oscillatory-II) cannot become the dominant instability mode here (due to the dampening out of such perturbations by the increased gravitational and surface tension forces).

Thus, panels (*a*-*d*) provide a comprehensive review of the stability picture under the parameter space $(De, \chi, Le, Ga, \Sigma)$. Besides exploring the parameter regions for which a particular instability mode becomes dominant in the system, they also highlight the competition between the various instability modes that may occur based on a few specific parameters set. These phase diagrams are expected to provide valuable guidance in choosing the parameters set for a realistic experimental setup.

4.7 Summary

In this chapter, we have investigated the Marangoni instability problem for a thin viscoelastic film considering the binary aspect of the fluid. Linear stability analysis around a quiescent basic state reveals that thermosolutocapillarity, in the presence of Soret diffusion, shows an entirely different stability picture from the case of purely thermocapillary driven instability studied in chapter 3. For the system subjected to heating from below, it is found that apart from the monotonic instability, two different oscillatory instabilities, namely oscillatory-I and oscillatory-II, can emerge in the system depending on the physical situations governed by the model parameters. The solutocapillary effect plays a crucial role in the case of long-wave disturbances, while the thermocapillary effect leads to the emergence of short-wave disturbances. For $\chi > 0$, solutocapillarity causes the appearance of long-wave monotonic or oscillatory-II instability (depending on the diffusivity ratio *Le*), whereas for $\chi < 0$, it enhances the stability of the system against the long-wave oscillatory-I perturbations. On the other hand, the thermocapillary effect is primarily responsible for the emergence of short-wave oscillatory-I disturbances.

Chapter 5

Marangoni Instability in a Viscoelastic Liquid Film Heated from the Free Surface

In this chapter, the instability problem is investigated for heating a polymeric liquid layer from the free surface. Considering the Soret effect and incorporating the effects of gravity, the stability characteristics of a polymeric film is studied when bounded between its deformable free surface and a poorly conductive rigid substrate. Linear stability analysis around the quiescent base state reveals that under the combined influences of thermo-solutocapillarity and the elasticity of the liquid, apart from the monotonic disturbances, two different oscillatory instabilities can emerge in this system.

5.1 Introduction

In Chapters 3 and 4, the instability problem is studied for a viscoelastic liquid film subjected to heating from below. In the extant literature too [71–74,106], the instability phenomenon is analysed only for the case of heating the system from below. However, previous investigations on the Marangoni instability in a Newtonian binary mixture [104,112] suggest that such a liquid film can get unstable for heating from the free surface. Therefore, an interesting proposition could be to study the effect of elasticity of the mixture on the stability behavior of the system. An attempt is made in this study to explore the Marangoni instability modes in a thin polymeric film confined between its deformable free surface and a rigid substrate. It is found that depending on the deformability of the free surface and the elasticity mixture, both the long-wave and short-wave disturbances can appear in this system. The characteristics of each instability mode are investigated here in detail, and the model parameter regimes are identified wherein it

The contents of this chapter have been published as Sarma, R. and Mondal, P. K. (2020) "Thermosolutal Marangoni instability in a viscoelastic liquid film: effect of heating from the free surface", J. Fluid Mech. vol. 909, A12.

can become dominant. However, the solvent is treated as non-volatile in this investigation.

This chapter is organized in six sections. In Section 5.2, we describe the physical system considered for investigation and present the governing equations and the related boundary conditions. Identifying the base state, a linear stability analysis is then carried out in Section 5.3. The results are presented in Section 5.4. The contributions of the fluid elasticity, and the thermocapillary and solutocapillary forces in producing the monotonic and oscillatory disturbances are also examined in this section. We plot the phase diagrams in Section 5.5 and finally, the main conclusions from this study are summarized in Section 5.6.

5.2 Mathematical Formulation

5.2.1 Governing equations and boundary conditions

Figure 5.1 schematically illustrates the problem under present investigation. We study the Marangoni instability in a thin layer of an incompressible viscoelastic polymer solution, resting initially on a flat rigid substrate (of lower thermal conductivity compared to the liquid) and is, in direct contact with air at higher temperature. A deformable free surface located at $z = h(x,t)$ separates the gas phase from the liquid.

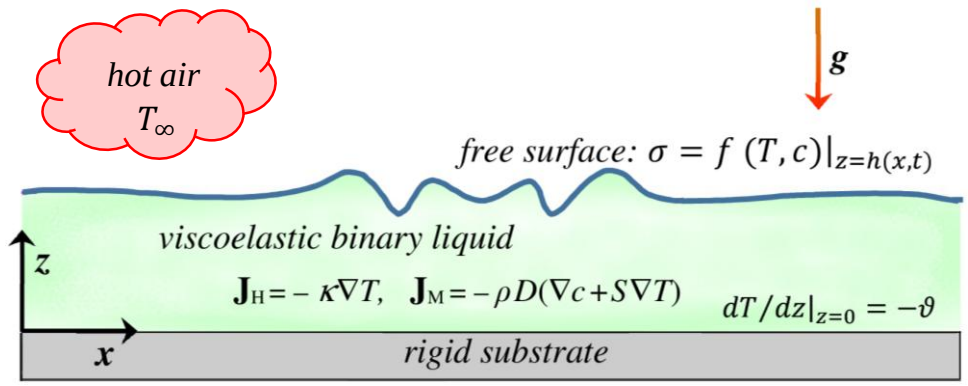

Figure 5.1: Schematic of the physical system under investigation. Marangoni instability is induced in a thin viscoelastic polymer film confined between its deformable free surface (located at $z = h(x,t)$), and a flat substrate (at the $z = 0$ plane) when subjected to heating from above. The polymeric solution is a binary mixture of Newtonian solvent with polymeric solute. The incorporation of Soret effect signifies the combined thermo-solutal instability in the system.

The entire liquid film is subjected to a uniform transverse temperature gradient, specified to be $-\vartheta$ at the $z=0$ plane. Thus, a negative (positive) ϑ indicates the case of heating the film from the air-liquid interface (substrate). Here, we are interested in investigating the instability phenomenon only for the former case (*i.e.*, heating the fluid layer at the air-liquid interface). This applied temperature gradient induces a concentration gradient in the film via the Soret effect. The heat and mass fluxes in the bulk of the liquid layer are thus given by [109]:

$$\mathbf{J}_{\mathrm{H}} = -\kappa \nabla T\,, \tag{5.1}$$

$$\mathbf{J}_{\mathrm{M}} = -\rho D\left(\nabla c + \mathcal{S}\nabla T\right), \tag{5.2}$$

respectively, where T is the temperature, c is the solute concentration and $\mathcal{S}$ is the Soret diffusion coefficient of the mixture. As mentioned in Chapter 4, for a polymeric solution, $\mathcal{S}$ can be either positive or negative depending on the solvent quality, the mole fractions of the components as well as based on the temperature of the mixture.

Now, above a certain critical temperature gradient, the thermocapillary and solutocapillary forces on the free liquid surface induce Marangoni convection in the liquid film. Here, we assume the surface tension to vary monotonically with temperature and concentration of the mixture, dictated by the relationship

$$\sigma = \sigma_o - \sigma_T\left(T - T_r\right) + \sigma_c\left(c - c_r\right), \tag{5.3}$$

where σ_o is the surface tension at the reference temperature T_r and concentration c_r. For most of the polymer blends $\sigma_T\,(=-\partial\sigma/\partial T\big|_{T=T_r}) > 0$, while $\sigma_c\,(=\partial\sigma/\partial c\big|_{c=c_r})$ can be either positive or negative. The effects of buoyancy are neglected in this study considering the small thickness of the film ($H \lesssim O\,(1)$ cm [11]. Furthermore, except σ, all other thermo-physical properties are assumed to remain invariant throughout the analysis. Therefore, the evolution of the film velocity $\boldsymbol{v} \equiv \{u(x,z,t), w(x,z,t)\}$, pressure $p(x,z,t)$, temperature $T(x,z,t)$ and solute concentration $c(x,z,t)$ with time t on the horizontal range $x \in (-\infty, \infty)$ and the vertical range $z \in [0,h]$ is governed by,

$$\nabla \bullet \boldsymbol{v} = \mathbf{0}\,, \tag{5.4}$$

$$\rho\left(\frac{\partial \boldsymbol{v}}{\partial t} + \boldsymbol{v}\bullet\nabla\boldsymbol{v}\right) = -\nabla p + \nabla\bullet\boldsymbol{\tau} - \rho g\,\mathbf{k}\,, \tag{5.5}$$

$$\frac{\partial T}{\partial t} + \boldsymbol{v} \bullet \nabla T = \alpha \, \nabla^2 T \,, \tag{5.6}$$

$$\frac{\partial c}{\partial t} + \boldsymbol{v} \bullet \nabla c = D \nabla^2 c + \mathcal{S} D \, \nabla^2 T \,, \tag{5.7}$$

respectively, where $\boldsymbol{\tau} = \begin{bmatrix} \boldsymbol{\tau}_{xx} & \boldsymbol{\tau}_{xz} \\ \boldsymbol{\tau}_{zx} & \boldsymbol{\tau}_{zz} \end{bmatrix}$ is the deviatoric stress tensor, **k** is the unit vector in the *z*-direction, and $\nabla \equiv \{\partial/\partial x, \partial/\partial z\}$. It is to be noted that the dynamics of gas and liquid phases are decoupled here considering the large ratios between their densities, viscosities, and thermal diffusivities.

The boundary conditions that accompany the set of governing equations 5.4 – 5.7 are as follows: at the rigid substrate, we impose the no-slip, no penetration condition for velocity, a specified heat flux, and the mass impermeability conditions, represented by

$$\boldsymbol{v} = \boldsymbol{0}, \qquad \frac{\partial T}{\partial z} = -\mathcal{G}, \qquad \frac{\partial c}{\partial z} = \mathcal{S}\mathcal{G} \qquad \text{at } z = 0, \tag{5.8$a-c$}$$

respectively.

At the deformable free surface, *i.e.*, at $z = h(x,t)$ the boundary conditions comprise of the kinematic condition

$$w = \frac{\partial h}{\partial t} + u \, \frac{\partial h}{\partial x} \,, \tag{5.9a}$$

which states that the velocity of the free surface is equal to the velocity of the liquid, thus giving its location.

The balance of the tangential and normal stress components at the free surface read

$$\frac{1}{\sqrt{1+(\partial h/\partial x)^2}} \left\{ \tau_{xz} \left[1 - \left(\frac{\partial h}{\partial x} \right)^2 \right] + \tau_{z\,z} \frac{\partial h}{\partial x} - \tau_{xx} \frac{\partial h}{\partial x} \right\} = \frac{\partial \sigma}{\partial x} + \frac{\partial \sigma}{\partial z} \frac{\partial h}{\partial x} \,, \tag{5.9b}$$

$$-p + \frac{1}{1+(\partial h/\partial x)^2} \left[\tau_{z\,z} + \tau_{xx} \left(\frac{\partial h}{\partial x} \right)^2 - 2 \, \tau_{x\,z} \frac{\partial h}{\partial x} \right] = \sigma \mathcal{H} \,, \tag{5.9c}$$

where $\mathcal{H} = \left(\partial^2 h/\partial x^2\right) \left[1 + (\partial h/\partial x)^2 \right]^{-3/2}$ is the mean curvature.

The thermal boundary condition at the free surface includes the balancing of heat flux across the interface. This heat exchange process with the ambient gas phase is approximated in this analysis by the heat transfer coefficient *q* between the liquid and the

gas phase as follows,

$$-\kappa\left(\frac{\partial h}{\partial x}\frac{\partial T}{\partial x}-\frac{\partial T}{\partial z}\right)+q\left(T-T_{\infty}\right)\sqrt{1+\left(\partial h/\partial x\right)^{2}}=0\,, \tag{5.9d}$$

where T_{∞} is the uniform gas temperature.

Finally, for this non-volatile binary mixture, the mass flux vanishes at the free surface. Mathematically, this is expressed by

$$\kappa\left(-\frac{\partial h}{\partial x}\frac{\partial c}{\partial x}+\frac{\partial c}{\partial z}\right)-\mathcal{S}q\left(T-T_{\infty}\right)\sqrt{1+\left(\partial h/\partial x\right)^{2}}=0\,. \tag{5.9e}$$

5.2.2 Non-dimensionalization

Let us now non-dimensionalize the boundary value problem (BVP) formulated by Eqs. 5.4 – 5.9. Considering the unperturbed film thickness *H* as the characteristic length scale, the thermal diffusion time H^{2}/α as the characteristic time scale, and $|\vartheta|H$ as temperature scale; we define the following set of dimensionless variables:

$$\left.\begin{aligned}\left(\bar{x},\bar{z}\right)&=\frac{(x,z)}{H},\quad \bar{h}=\frac{h}{H},\quad \bar{t}=\frac{t}{H^{2}/\alpha},\quad \left(\bar{u},\bar{w}\right)=\frac{u,w}{\left(\alpha/H\right)},\quad \bar{\tau}=\frac{\tau}{\mu\alpha/H^{2}},\\ \bar{p}&=\frac{p}{\mu\alpha/H^{2}},\quad \bar{T}=\frac{T-T_{\infty}}{|\vartheta|H},\quad \bar{c}=\frac{c}{\sigma_{T}|\vartheta|H/\sigma_{c}}.\end{aligned}\right\} \tag{5.10}$$

It may be noted that the characteristic scale adopted in Eq. 5.10 coincides with those used in Chapter 4. Dropping the over-bar sign from the non-dimensional variables for the convenience in presentation, we finally arrive at the following set of dimensionless governing equations:

$$\nabla\bullet\ \boldsymbol{v}=\boldsymbol{0}\,, \tag{5.11}$$

$$Pr^{-1}\left(\frac{\partial\boldsymbol{v}}{\partial t}+\boldsymbol{v}\bullet\nabla\boldsymbol{v}\right)=-\nabla p+\nabla\bullet\boldsymbol{\tau}-Ga\,\boldsymbol{k}\,, \tag{5.12}$$

$$\frac{\partial T}{\partial t}+\boldsymbol{v}\bullet\nabla T=\nabla^{2}T\,, \tag{5.13}$$

$$\frac{\partial c}{\partial t}+\boldsymbol{v}\bullet\nabla c=Le\left(\nabla^{2}c+\chi\nabla^{2}T\right). \tag{5.14}$$

The boundary conditions now take the form

$$\boldsymbol{v}=\boldsymbol{0}, \qquad \frac{\partial T}{\partial z}=-\mathcal{Q}, \qquad \frac{\partial c}{\partial z}=\chi\mathcal{Q} \qquad \text{at } z=0, \qquad (5.15a-c)$$

and

$$w=\frac{\partial h}{\partial t}+u\frac{\partial h}{\partial x}\ , \qquad (5.16a)$$

$$\left(\frac{\partial T}{\partial z}-\frac{\partial h}{\partial x}\frac{\partial T}{\partial x}\right)+Bi\ T\sqrt{1+\left(\partial h/\partial x\right)^2}=0, \qquad (5.16b)$$

$$\left(\frac{\partial c}{\partial z}-\frac{\partial h}{\partial x}\frac{\partial c}{\partial x}\right)-\chi Bi\ T\sqrt{1+\left(\partial h/\partial x\right)^2}=0, \qquad (5.16c)$$

$$-p+\frac{1}{1+\left(\partial h/\partial x\right)^2}\left[\tau_{z\,z}+\tau_{x\,x}\left(\frac{\partial h}{\partial x}\right)^2-2\tau_{x\,z}\frac{\partial h}{\partial x}\right]=\Sigma\frac{\partial^2 h/\partial x^2}{\left[1+\left(\partial h/\partial x\right)^2\right]^{3/2}}, \qquad (5.16d)$$

$$\frac{1}{\sqrt{1+\left(\partial h/\partial x\right)^2}}\left\{\tau_{x\,z}\left[1-\left(\frac{\partial h}{\partial x}\right)^2\right]+\tau_{z\,z}\frac{\partial h}{\partial x}-\tau_{x\,x}\frac{\partial h}{\partial x}\right\}=Ma\left[\frac{\partial c}{\partial x}-\frac{\partial T}{\partial x}+\left(\frac{\partial c}{\partial z}-\frac{\partial T}{\partial z}\right)\frac{\partial h}{\partial x}\right]$$

$$\text{at } z=h\left(x,t\right). \qquad (5.16e)$$

The Maxwell constitutive model is used for depicting the rheological behavior of the fluid in this analysis as well, which in non-dimensional form reads

$$\boldsymbol{\tau}+De\frac{\partial\boldsymbol{\tau}}{\partial t}=\left(\nabla\boldsymbol{v}\right)+\left(\nabla\boldsymbol{v}\right)^T. \qquad (5.17)$$

The non-dimensional parameter $\mathcal{Q}=\vartheta/|\vartheta|$ introduced in Eq. 5.15 indicates the direction of the applied temperature gradient. $\mathcal{Q}=1$ represents the case of heating the fluid layer from below, while $\mathcal{Q}=-1$ stands for heating from above. Besides $\mathcal{Q}$, this BVP is further governed by the following set of dimensionless parameters: the Marangoni number, *Ma*, the Soret number, χ, the Deborah number, *De*, the (inverse) Lewis number, *Le*, the Biot number, *Bi*, the Prandtl number, *Pr*, the Galileo number, *Ga*, and the (inverse) capillary number, Σ:

$$\left.\begin{aligned} &Ma=\frac{\sigma_T|\vartheta|H^2}{\mu_o\alpha}, \quad \chi=\frac{\mathcal{S}\sigma_c}{\sigma_T}, \quad De=\frac{\lambda\alpha}{H^2}, \quad Le=\frac{D}{\alpha},\\ &Bi=\frac{qH}{\kappa}, \quad Pr=\frac{\mu_o}{\rho\alpha}, \quad Ga=\frac{\rho gH^3}{\mu_o\alpha}, \quad \Sigma=\frac{\sigma H}{\mu_o\alpha}. \end{aligned}\right\} \qquad (5.18)$$

These parameters are defined exactly in the same manner as those in Chapter 4.

5.3 Base State and Linear Stability Analysis

In the absence of convection in the liquid film, the BVP (5.11) – (5.17) satisfies a no-flow, laterally uniform base state with constant film thickness. This set of steady solutions is given by

$$\left.\begin{aligned} \boldsymbol{v}^o = \mathbf{0}, \qquad \boldsymbol{\tau}^o = \mathbf{0}, \qquad h^o = 1, \qquad p^o = Ga\left(1-z\right), \\ T^o = \mathcal{Q}\left(1-z+Bi^{-1}\right), \qquad c^o = \mathcal{Q}\,\chi z + const. \end{aligned}\right\} \tag{5.19}$$

In this section, we carry out a linear stability analysis for infinitesimal perturbations around this conductive state of the system. To proceed with, we define the following set of two-dimensional perturbed fields (denoted by a tilde)

$$\left.\begin{aligned} \boldsymbol{v} = \boldsymbol{v}^o + \tilde{\boldsymbol{v}}(x,z,t), \qquad \boldsymbol{\tau} = \boldsymbol{\tau}^o + \tilde{\boldsymbol{\tau}}(x,z,t), \qquad p = p^o + \tilde{p}(x,z,t), \\ T = T^o + \tilde{\theta}(x,z,t), \qquad h = h^o + \tilde{\xi}(x,z,t), \qquad c = c^o + \tilde{c}(x,z,t). \end{aligned}\right\} . \tag{5.20a-f}$$

Substituting the perturbed fields into Eqs. 5.11 – 5.16, and subsequently linearizing about the base state by neglecting the terms non-linear in perturbations, we obtain

$$\nabla \bullet \tilde{\boldsymbol{v}} = \mathbf{0}, \tag{5.21}$$

$$Pr^{-1}\frac{\partial \tilde{\boldsymbol{v}}}{\partial t} = -\nabla\tilde{p} + \nabla \bullet \tilde{\boldsymbol{\tau}}, \tag{5.22}$$

$$\frac{\partial \tilde{\theta}}{\partial t} - \mathcal{Q}\,\tilde{w} = \nabla^2\tilde{\theta}, \tag{5.23}$$

$$\frac{\partial \tilde{c}}{\partial t} + \mathcal{Q}\,\chi\tilde{w} = Le\left(\nabla^2\tilde{c} + \chi\nabla^2\tilde{\theta}\right); \tag{5.24}$$

with the boundary conditions

$$\tilde{\boldsymbol{v}} = \mathbf{0}, \qquad \frac{\partial \tilde{\theta}}{\partial z} = 0, \qquad \frac{\partial \tilde{c}}{\partial z} = 0 \qquad \text{at } z = 0, \tag{5.25a-c}$$

and

$$\left.\begin{aligned} \frac{\partial \tilde{\xi}}{\partial t} = \tilde{w}, \qquad \frac{\partial \tilde{\theta}}{\partial z} = -Bi\left(\tilde{\theta} - \mathcal{Q}\tilde{\xi}\right), \qquad \frac{\partial \tilde{c}}{\partial z} = \chi Bi\left(\tilde{\theta} - \mathcal{Q}\tilde{\xi}\right), \\ \tilde{\tau}_{xz} = Ma\frac{\partial}{\partial x}\left(\tilde{c} - \tilde{\theta} + \mathcal{Q}\tilde{\xi} + \mathcal{Q}\chi\tilde{\xi}\right), \qquad -\tilde{p} + Ga\;\tilde{\xi} + \tilde{\tau}_{zz} = \Sigma\;\frac{\partial^2\tilde{\xi}}{\partial x^2} \quad \text{at } z = 1, \end{aligned}\right\} \tag{5.26a-e}$$

while the constitutive relation (5.17) reads

$$\tilde{\boldsymbol{\tau}} + De\frac{\partial \tilde{\boldsymbol{\tau}}}{\partial t} = \left(\nabla\tilde{\boldsymbol{v}}\right) + \left(\nabla\tilde{\boldsymbol{v}}\right)^T. \tag{5.27}$$

For the sake of convenience, this BVP is now cast in terms of the stream function $\tilde{\psi}(x,z,t)$, such that

$$\tilde{u} = \frac{\partial \tilde{\psi}}{\partial z}, \qquad \tilde{w} = -\frac{\partial \tilde{\psi}}{\partial x}, \tag{5.28a,b}$$

which eliminates $\tilde{p}$ from the system of equations 5.21 – 5.26. Introducing the stream function relationships (5.28) along with the constitutive equation 5.27, we finally arrive at

$$Pr^{-1}\left(\frac{\partial}{\partial t}\nabla^2\tilde{\psi} + De\frac{\partial^2}{\partial t^2}\nabla^2\tilde{\psi}\right) = \nabla^4\tilde{\psi}, \tag{5.29}$$

$$\frac{\partial \tilde{\theta}}{\partial t} + \mathcal{Q}\frac{\partial \tilde{\psi}}{\partial x} = \nabla^2\tilde{\theta}, \tag{5.30}$$

$$\frac{\partial \tilde{c}}{\partial t} - \mathcal{Q}\chi\frac{\partial \tilde{\psi}}{\partial x} = Le\left(\nabla^2\tilde{c} + \chi\nabla^2\tilde{\theta}\right), \tag{5.31}$$

with the boundary conditions,

$$\tilde{\psi} = 0, \qquad \frac{\partial \tilde{\psi}}{\partial z} = 0, \qquad \frac{\partial \tilde{\theta}}{\partial z} = 0, \qquad \frac{\partial \tilde{c}}{\partial z} = 0 \quad \text{at } z = 0, \tag{5.32a–d}$$

$$\frac{\partial \tilde{\xi}}{\partial t} = -\frac{\partial \tilde{\psi}}{\partial x}, \qquad \frac{\partial \tilde{\theta}}{\partial z} = -Bi\left(\tilde{\theta} - \mathcal{Q}\tilde{\xi}\right), \qquad \frac{\partial \tilde{c}}{\partial z} = \chi Bi\left(\tilde{\theta} - \mathcal{Q}\tilde{\xi}\right), \tag{5.33a–c}$$

$$\frac{\partial^2\tilde{\psi}}{\partial z^2} - \frac{\partial^2\tilde{\psi}}{\partial x^2} = Ma\frac{\partial}{\partial x}\left(\tilde{c} - \tilde{\theta} + \mathcal{Q}\tilde{\xi} + \mathcal{Q}\chi\tilde{\xi}\right) + Ma\,De\frac{\partial^2}{\partial t\partial x}\left(\tilde{c} - \tilde{\theta} + \mathcal{Q}\tilde{\xi} + \mathcal{Q}\chi\tilde{\xi}\right), \tag{5.33d}$$

$$\left(1 + De\frac{\partial}{\partial t}\right)\left(\Sigma\frac{\partial^3\tilde{\xi}}{\partial x^3} - Pr^{-1}\frac{\partial^2\tilde{\psi}}{\partial t\partial z} - Ga\frac{\partial\tilde{\xi}}{\partial x}\right) = -\frac{\partial}{\partial z}\left(3\frac{\partial^2\tilde{\psi}}{\partial x^2} + \frac{\partial^2\tilde{\psi}}{\partial z^2}\right)$$

$$\text{at } z = 1. \tag{5.33e}$$

It is important to note that, since the basic state (*i.e.*, Eq. 5.19) is invariant with respect to *x* and *t*; we can employ the Fourier decomposition to separate the *x* and *t* dependency of the perturbed fields $(\tilde{\psi}, \tilde{\theta}, \tilde{c}, \tilde{\xi})$ from that with *z*:

$$\left(\tilde{\psi}(x,z,t),\ \tilde{\theta}(x,z,t),\ \tilde{c}(x,z,t),\ \tilde{\xi}(x,z,t)\right) = \left(\bar{\psi}(z),\ \bar{\theta}(z),\ \bar{c}(z),\ \bar{\xi}(z)\right)\exp\left(i\,k\,x - \lambda\,t\right). \tag{5.34}$$

In Eq. 5.34, $(\bar{\psi}, \bar{\theta}, \bar{c}, \bar{\xi})$ represent the amplitude of perturbations, *k* denotes the dimensionless horizontal wavenumber and $\lambda = \Omega + i\omega$ refers to the decay rate of the

perturbations with ω (a real quantity) as the oscillation frequency. The dynamics of these infinitesimal perturbations is now governed by the following EVP:

$$Pr\frac{d^4\hat{\psi}}{dz^4}-\left(\lambda^2 De-\lambda+2Prk^2\right)\frac{d^2\hat{\psi}}{dz^2}+\left(\lambda^2 De-\lambda+Prk^2\right)k^2\hat{\psi}=0, \qquad (5.35)$$

$$\frac{d^2\hat{\theta}}{dz^2}+\left(\lambda-k^2\right)\hat{\theta}=ik\mathcal{Q}\hat{\psi}, \qquad (5.36)$$

$$Le\frac{d^2\hat{c}}{dz^2}+\left(\lambda-Lek^2\right)\hat{c}=-Le\chi\left(\frac{d^2\hat{\theta}}{dz^2}-k^2\hat{\theta}\right)-ik\mathcal{Q}\chi\hat{\psi}; \qquad (5.37)$$

$$\hat{\psi}=0, \quad \frac{d\hat{\psi}}{dz}=0, \quad \frac{d\hat{\theta}}{dz}=0 \quad , \quad \frac{d\hat{c}}{dz}=0 \qquad \text{at } z=0, \quad (5.38a-d)$$

$$ik\hat{\psi}=\lambda\hat{\xi}, \qquad \frac{d\hat{\theta}}{dz}=-Bi\left(\hat{\theta}-\mathcal{Q}\hat{\xi}\right), \qquad \frac{d\hat{c}}{dz}=Bi\chi\left(\hat{\theta}-\mathcal{Q}\hat{\xi}\right), \quad (5.39a-c)$$

$$\frac{d^2\hat{\psi}}{dz^2}+k^2\hat{\psi}=iMak\left(1-De\lambda\right)\left(\hat{c}-\hat{\theta}+\mathcal{Q}\hat{\xi}+\mathcal{Q}\chi\hat{\xi}\right), \qquad (5.39d)$$

$$Pr\frac{d^3\hat{\psi}}{dz^3}+\left(\lambda-\lambda^2 De-3Prk^2\right)\frac{d\hat{\psi}}{dz}=ikPr\left(1-\lambda De\right)\left(Ga+\Sigma k^2\right)\hat{\xi} \quad \text{at } z=1. \quad (5.39e)$$

The eigenvalues λ and Ma depend on the parameter set (k, Bi, De, Le, χ, Ga, Σ, Pr) and also on $\mathcal{Q}$. Solving the EVP for $\mathcal{Q}=-1$, now one can study the stability characteristics of the system for the case of heating from the free surface. However, the complexity of the solvability conditions here restrains us from taking an analytical approach to finding the eigenvalues λ and Ma. We thus solve Eqs. 5.35 – 5.39 numerically using the fourth-order Runge-Kutta method and employing the shooting technique.

The EVP posed by Eqs. 5.35 – 5.39 suggests the possible emergence of two different instability modes in the system: (*i*) Monotonic mode ($\lambda=0$ at the instability threshold for this mode); and (*ii*) Oscillatory mode (for this mode, λ attains a purely imaginary value ($=i\omega$) at the instability threshold).

5.4 Results

We now proceed to analyse the stability picture for both the long-wave, $k<O(1)$ and short-wave, $k\gtrsim O(1)$ perturbations. Here, we are primarily interested in investigating

how viscoelasticity in the presence of Soret effect deviates the stability of the system from its Newtonian counterpart. Let us first start with the monotonic instability mode.

5.4.1 Monotonic mode

The neutral stability curves $Ma(k)$ for the monotonic instability mode are displayed in Fig. 5.2. The solid line and the symbols ◊ (dotted line and the symbols ☆) refers here to a liquid layer with a deformable (non-deformable) free surface. It can be observed that for the entire range of wavenumbers k, there exists a minimum Marangoni number Ma (denoted by the mark '○') only above which the instability sets in the system. We call this Ma as the critical Marangoni number (Ma_c), and the corresponding k and ω as the critical wave number (k_c) and critical oscillation frequency (ω_c), respectively.

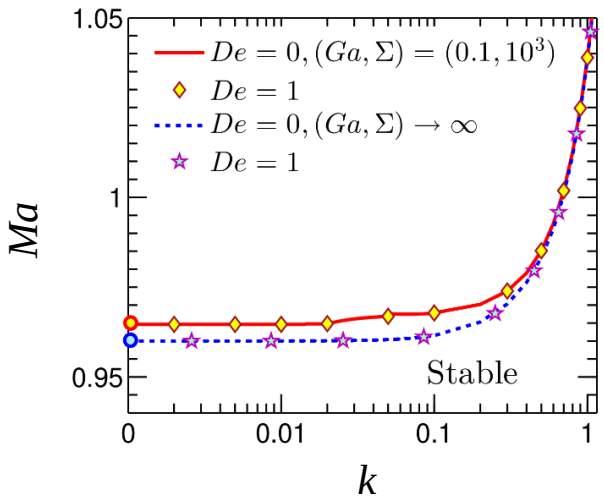

Figure 5.2: Neutral stability curves $Ma(k)$ for the monotonic instability mode at $\chi = -0.5$, $Bi = 0.1$, $Le = 10^{-2}$, $Pr = 10$. The solid line and the symbols ◊ depict the stability boundary for a system with a deformable free surface $(Ga, \Sigma) = (0.1, 10^3)$; the dotted line and the symbols ☆ show the stability threshold for a system possessing non-deformable free surface $(Ga, \Sigma) \to \infty$. The dot (○) mark on each neutral curve represents the critical point of the curve.

Figure 5.2 shows that for the system subjected to heating from the gas-liquid interface, the monotonic disturbances always emerge in the long-wave form $(k_c = 0)$, irrespective of the deformability of free surface. Confirming the results of Podolny *et al.* [104], this study re-establishes the fact that, the increasing deformability of free surface

leads to a mild enhancement in the stability of the system against these long-wavelength perturbations. On the other hand, Ma_c for the onset of stationary convection is found to be independent of the elasticity of the fluid. The indication is that both the Newtonian and viscoelastic binary liquids show identical behavior towards this particular instability mode. This is also apparent from the EVP (5.35) – (5.39), which becomes independent of *De* for $\lambda = 0$.

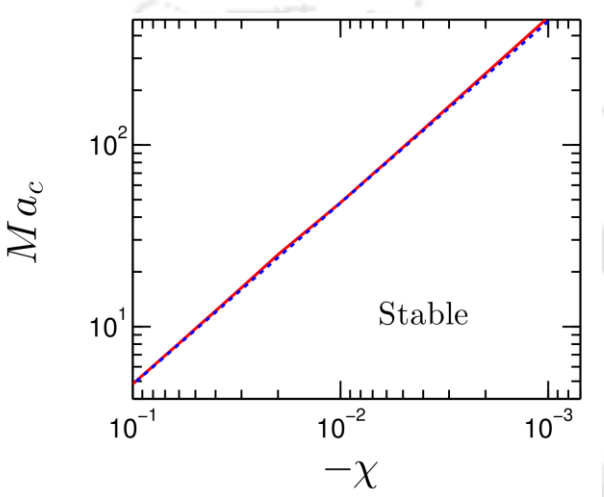

Figure 5.3: Effect of χ on the stability threshold for the monotonic instability mode at $Bi = 10^{-2}$, $Le = 10^{-2}$, $Pr = 10$. The solid and the dotted line demonstrates the stability boundary for a liquid layer with a deformable $(Ga, \Sigma) = (0.1, 10^3)$ and non-deformable $(Ga, \Sigma) \to \infty$ free surface, respectively.

Now, in order to examine the relative contributions of the thermocapillary and solutocapillary forces in producing these stationary disturbances, we plot in Fig. 5.3 the variation of Ma_c with χ for both the cases of the deformable and non-deformable free surface. One can see that irrespective of the surface deformability, the system always remains stable to such disturbances for $\chi \geq 0$, and the instability emerges only when $\chi < 0$. The disappearance of this instability mode for $\chi = 0$, and a reducing Ma_c with $|\chi|$ suggests that the monotonic disturbances are the sole outcome of the solutocapillary effect. The thermocapillarity plays here a stabilizing role. An increasing solutocapillary force corresponding to higher values of $|\chi|$ promotes the onset of instability in the system as can be observed from Fig. 5.3. Interestingly, we will demonstrate later that, for a

shorter mass diffusion time scale (H^2/D), this interplay between the two driving forces can give rise to an oscillatory instability in the system.

5.4.2 Oscillatory mode

Let us now focus our attention on the disturbances that emerge with temporal oscillations. Here, we will demonstrate that thermo-solutocapillarity, together with the elasticity of the fluid, can give rise to two different oscillatory instabilities in the system. We call them as the oscillatory-I and oscillatory-II mode. In what follows, we systematically study the characteristics of both the instability modes by identifying the mechanism behind their origination.

5.4.2.1 *Oscillatory-I mode*

Figure 5.4 plots the neutral stability curves and the corresponding oscillation frequencies for the oscillatory-I mode. The solid and the dashed lines represent the results for a deformable free surface, while their adjacent dotted lines correspond to a non-deformable free surface. It can be clearly seen that each neutral curve consists of two

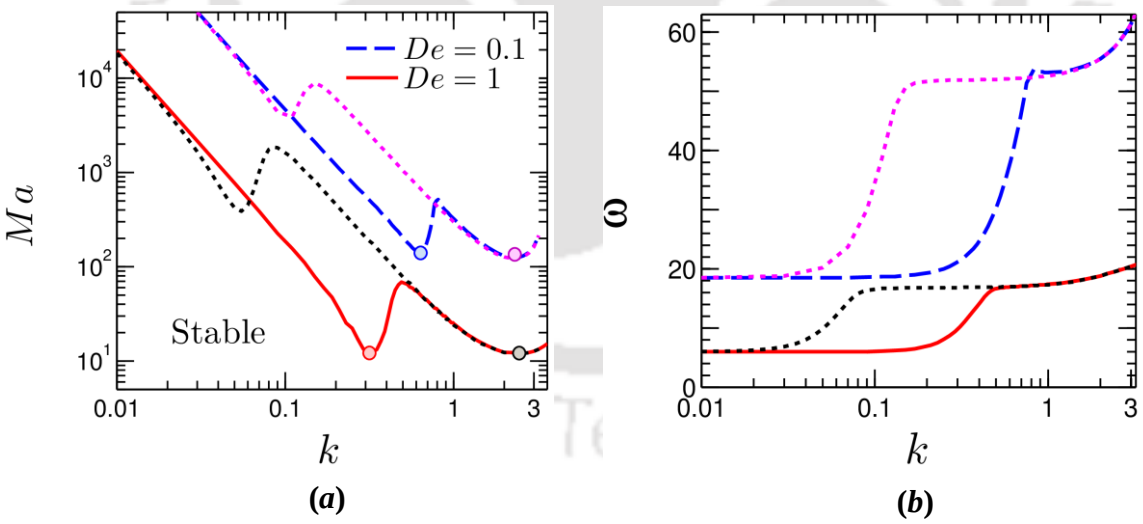

Figure 5.4: (*a*) Neutral stability curves $Ma(k)$ and the corresponding (*b*) oscillation frequency ω for the oscillatory-I mode at $\chi = -0.5$, $Bi = 0.1$, $De = 1$, $Le = 10^{-2}$, $Pr = 10$. The dashed and solid line depicts the stability boundary for a deformable free surface, while their adjacent dotted line demonstrates the stability threshold for a non-deformable free surface (for the same *De*). The dot (o) mark on each neutral curve represents the critical point (the global minimum) of the curve.

branches, both characterized by a distinct local minimum. Of these two local minima, while one lies in the long-wave regime ($k_c < O(1)$), the other one resides in the short-wave regime ($k_c \gtrsim O(1)$). Accordingly, we call these branches as the long-wave and short-wave branch, respectively.

Figure 5.4(a) shows that the reducing deformability of free surface leads to a substantial increment in the Ma_c pertaining to the long-wave branch. Thus, for a non-deformable surface, the oscillatory-I disturbances emerge only in the short-wave form. For a given *De*, the critical parameters (Ma_c, k_c, ω_c) for this short-wave branch remains unaffected by the deformability of free surface. On the other hand, for a liquid layer with a deformable free surface, Ma_c corresponding to the long-wave branch attains the global minimum, resulting in the first bifurcation to occur into the long-wave oscillatory-I mode. It is therefore apparent that depending on the deformability of free surface, a competition between the long-wave and short-wave oscillatory-I disturbances can also take place in the system.

Earlier reported studies on the Marangoni instability in a Newtonian binary mixture [13,111] however suggest that, a liquid layer remains always stable to the oscillatory disturbances for the case of heating from above. We will now demonstrate that for this particular direction of heating, the oscillatory-I instability is experimentally feasible only in case of a highly viscoelastic film and not in the Newtonian or a weakly viscoelastic film.

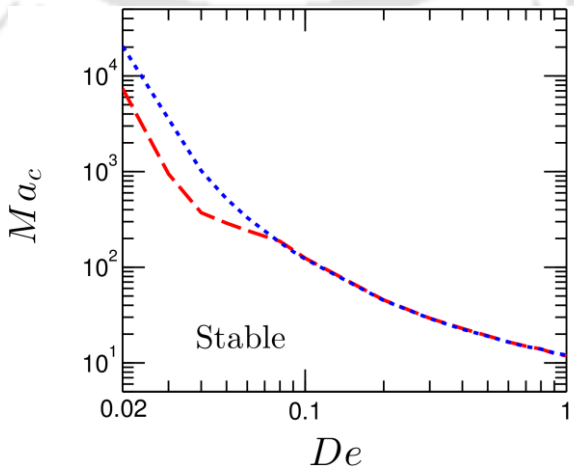

Figure 5.5: Effect of fluid elasticity on the instability threshold for the oscillatory-I mode.

The dashed and dotted line depicts the variation for a liquid layer with deformable $(Ga,\Sigma)=(0.1,10^3)$ and non-deformable free surface $(Ga,\Sigma)\to\infty$ respectively. Ma_c refers to the global minimum of the $Ma(k)$ neutral curve. Other parameters: $Bi=0.1$, $Le=10^{-2}$, $Pr=10$.

From Fig. 5.5, one can find that $Ma_c \approx O(10^4)$ for $De \approx O(10^{-2})$, whereas $Ma_c \approx O(10)$ for $De \approx O(1)$. Thus, for a 0.1 mm thick film with $\sigma_T \approx O(10^{-4})$ N(mK)$^{-1}$, $\mu_o \approx O(10^{-2})$ Pa.s, and $\alpha \approx O(10^{-7})$ m^{2}s^{-1} ; the critical temperature difference $(|\vartheta|H)$ required to maintain across the film for the onset of oscillatory-I convection is 10^3 K for $De \approx O(10^{-2})$; whereas for $De \approx O(1)$, $(|\vartheta|H)\approx 1$K. Since Ma_c follows an inverse correlation with *De*, the necessary temperature difference will be even higher for $De < O(10^{-2})$, which seems to be unrealistic considering the thickness of the film. On the other hand, for $De \gtrsim O(1)$, $(|\vartheta|H)\lesssim 1$K, and is experimentally feasible.

Competition between the thermocapillary and solutocapillary forces

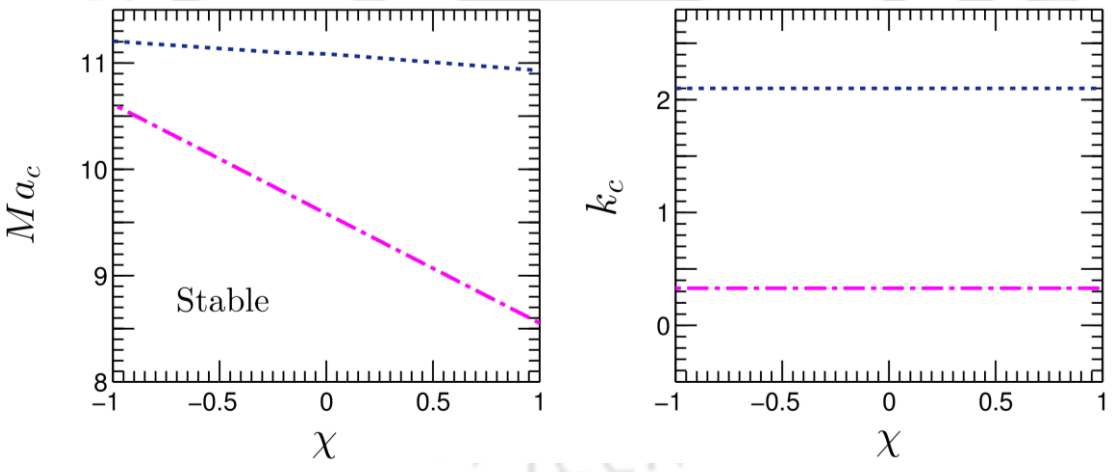

Figure 5.6: Variation of the (*a*) critical Marangoni number Ma_c and the (*b*) critical wave number k_c with χ for the oscillatory-I instability mode at $Bi=10^{-2}$, $De=1$, $Pr=10$, $Le=10^{-3}$. In panels (*a*,*b*), the dash-dotted line represents the results for a deformable free surface $(Ga,\Sigma)=(0.1,10^3)$, while the dotted line depicts the results for a non-deformable free surface $(Ga,\Sigma)\to\infty$.

Continuing our discussion on the oscillatory-I mode, we now plot in Fig. 5.6(*a*) the variation of Ma_c with χ, essentially to understand the relative contributions of the thermocapillary and solutocapillary forces in triggering these disturbances in the system. It is important to note that, Ma_c refers here to the global minimum of the $Ma(k)$ neutral curve. The emergence of oscillatory-I instability even for $\chi = 0$, and a reducing Ma_c with *De* (clear from Fig. 5.5) suggests that thermocapillarity, coupled with the elasticity of the fluid, primarily give rise to these disturbances.[2] The solutocapillarity has only a mild influence in producing this particular instability mode.

From Fig. 5.6(*a*) it is clear that irrespective of the nature of Soret effect (*i.e.*, whether $\mathcal{S}$ is positive or negative), the oscillatory-I instability can appear for any $\chi \in \mathbb{R}$. Nevertheless, it is important to note that for $\chi > 0$, the solutocapillary force promotes the onset of instability in the system, whereas, it weakly enhances the stability of the system for $\chi < 0$. Interestingly, this contribution of the solutocapillarity on the instability threshold varies with the deformability of free surface. Figure 5.6(*b*) shows that for a deformable free surface, the oscillatory-I disturbances emerge in the long-wave form, while, the perturbations appear in the short-wave form in case of a non-deformable surface. Hence, it seems reasonable to infer that compared to the short-wave disturbances, the solutocapillary effect is more dominant for the long-wave perturbations.

5.4.2.2 *Oscillatory-II mode*

In Section 5.4.1, we have pointed out that an oscillatory instability can develop in the present system for $\chi < 0$ at higher values of *Le*. Clearly, this is a different mode of oscillatory instability from the previous one (*i.e.*, the oscillatory-I mode which can develop for any $\chi \in \mathbb{R}$). We call it the oscillatory-II mode. Below, we demonstrate that the characteristics of this mode are quite different from the oscillatory-I mode.

The typical neutral stability curves for the oscillatory-II mode are presented in Fig. 5.7. It is immediately clear that this is a long-wavelength instability with $k_c \approx O(10^{-3})$.

[2]This behavior of the oscillatory-I mode complies with the behavior of oscillatory disturbances detected previously by [71–73] for a *pure* viscoelastic liquid film heated from below. Thus, the oscillatory-I perturbations are essentially the oscillatory disturbances observed therein.

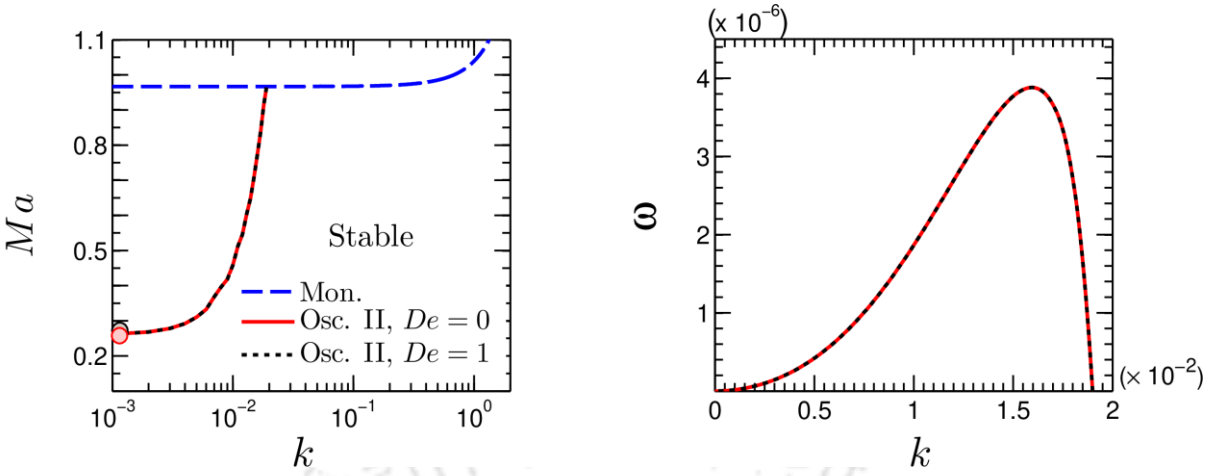

Figure 5.7: (*a*) Neutral stability curves $Ma(k)$ and the corresponding (*b*) oscillation frequency ω for the oscillatory-II mode at $\chi = -0.5$, $Bi = 0.1$, $De = 1$, $Le = 10^{-2}$, $Pr = 10$, $(Ga, \Sigma) = (0.1, 10^3)$. The dot (o) mark on each neutral curve in panel (*a*) represents the critical point of the curve. At higher values of *k*, the neutral curves for the oscillatory-II mode merge with the neutral curve for the monotonic mode.

At higher values of *k*, the neutral curve for the oscillatory-II mode merges with the neutral curve for the monotonic instability mode. This limits the appearance of these disturbances only in the long-wave form. Another key observation from Fig. 5.7(*a*) is that Ma_c for the oscillatory-II mode is independent of the values of *De*. This indicates that the instability threshold of the system for this particular mode is not affected by the elastic behavior of the binary mixture.

Figure 5.7(*b*) plots the corresponding oscillation frequencies of the neutral perturbations. As expected, ω for the oscillatory-II mode is not affected by the viscoelasticity of the fluid. A comparison between Figs. 5 and 8 now reveal that $k_{c,\text{Osc.-II}} << k_{c,\text{Osc.-I}}$ and $\omega_{c,\text{Osc.-II}} << \omega_{c,\text{Osc.-I}}$, even for the long-wave oscillatory-I mode. Thus, compared to the oscillatory-I mode, the oscillatory-II disturbances emerge with much larger sized convection cells possessing higher oscillation periods. This is discussed in more details in Section 5.6.

Competition between the thermocapillary and solutocapillary forces

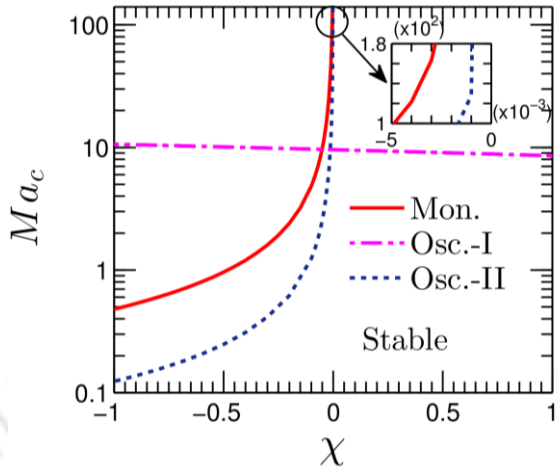

Figure 5.8: Variation of the critical Marangoni number Ma_c with χ for the oscillatory-II mode (dotted line) at $Bi = 10^{-2}$, $De = 1$, $Le = 10^{-2}$, $(Ga, \Sigma) = (0.1, 10^3)$ and $Pr = 10$. $Ma_c - \chi$ variations for the monotonic (solid line) and oscillatory-I (dashed-dotted line) modes are plotted here for reference. Inset shows the zoomed-in view for $\chi \to 0$.

Now, in order to explore the physical mechanism behind the origination of the oscillatory-II instability in the system, we plot in Fig. 5.8 the variation of critical Marangoni number with the Soret number. It is found that similar to the monotonic mode, an increasing $|\chi|$ promotes the onset of oscillatory-II perturbations as well. Notably, this particular instability mode emerges in the system only for $Le \gtrsim O(10^{-2})$, *i.e.*, for a shorter mass diffusion time (H^2/D) compared to the thermal diffusion time (H^2/α). The disappearance of these perturbations for $\chi = 0$ and a reducing Ma_c with $|\chi|$ thus suggests that, at a higher rate of solute diffusivity, the increasing competition between the destabilizing solutocapillary and the stabilizing thermocapillary forces give rises to the oscillatory-II mode. It should be noted that similarly to the solutocapillary dominated monotonic mode, for this mode too, the disturbances always appear in the long-wave form. However, unlike the former one, the oscillatory-II instability can develop only in a deformable free surface. One can see in Fig. 5.9 that on reducing the deformability of free surface, the stability threshold increases and the oscillation frequency decay. Finally, $\omega \approx 0$ in the limit $(Ga, \Sigma) \to \infty$, leading to the disappearance of the oscillatory-II mode in a non-deformable free surface.

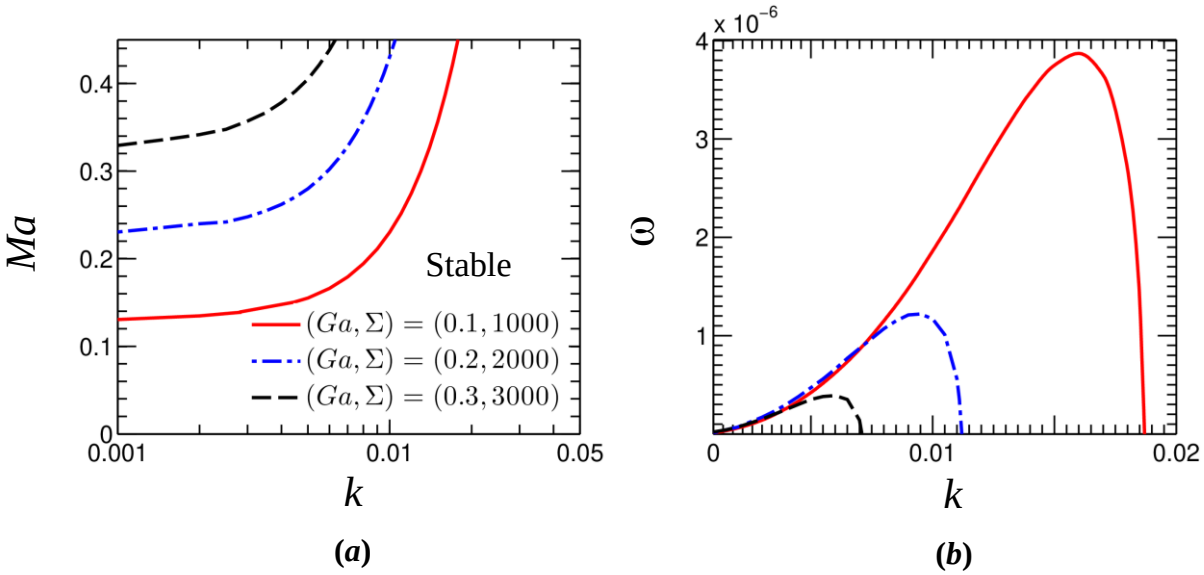

Figure 5.9: Effect of free surface deformability on the (*a*) instability threshold and the (*b*) oscillation frequency of the neutral perturbations for the oscillatory-II mode at $Bi = 0.1,\ De = 1,\ \chi = -0.1,\ Le = 10^{-2},\ Pr = 10$.

5.5 Phase Diagrams

Now, to obtain a clear perception of the stability picture, we plot in this section the phase diagrams. These diagrams are helpful in identifying the regions of model parameters for which a particular instability mode becomes dominant in the system (for bifurcation around the conductive base state). In panels (*a-d*) of Fig. 5.10, regime-1 represents the monotonic mode, regime-2 the long-wave oscillatory-I mode, regime-3 the short-wave oscillatory-I mode, and regime-4 refers to the oscillatory-II mode. Any dataset corresponding to the boundary between the adjacent instability modes (shown by the dotted line) indicates a competition between them to become the dominant instability mode in the system.

Panel (*a*) plots the phase diagram for a liquid layer with a deformable free surface at $Le = 10^{-3}$. For this system, the monotonic disturbances (regime-1) emerge for $\chi < 0$, and the long-wave oscillatory-I instability (regime-2) appears for $\chi \geq 0$. On the other hand, for a higher rate of solute diffusivity (*i.e.*, $Le = O(0.1)$) panel (*b*) shows that for $\chi < 0$, instead of the monotonic mode, the conductive state first bifurcates into the oscillatory-II mode (regime 4). However, for $\chi \geq 0$, the long-wave oscillatory-I instability prevails in the system. It is important to note that a competition between the

long-wave and short-wave oscillatory-I disturbances may also take place in the system for $\chi \geq 0$ depending on the deformability of free surface (cf. Fig. 5.4*a*).

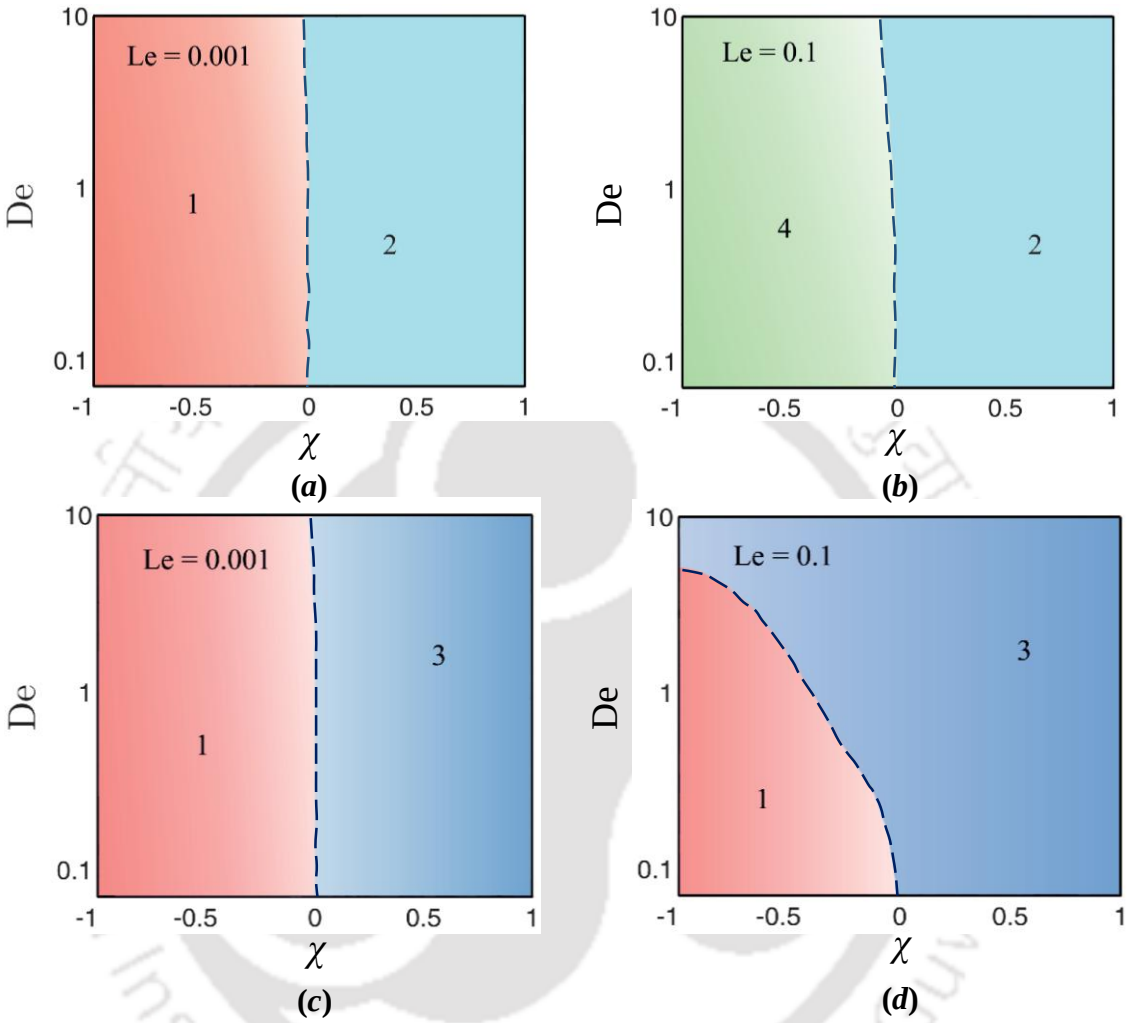

Figure 5.10: Phase diagrams summarising the boundaries between different dominant instability mode in the (De, χ) plane for different values of *Le*: (*a*,*b*) deformable free surface $(Ga, \Sigma) = (0.1, 10^3)$, and (*c*,*d*) non-deformable free surface $(Ga, \Sigma) \to \infty$. Other parameters: $Bi = 10^{-2}$, $Pr = 10$. In panels (*a*-*d*), regime-1: monotonic instability, regime-2: long-wave oscillatory–I instability, regime-3: short-wave oscillatory–I instability, regime-4: oscillatory –II instability.

For a non-deformable free surface, panels (*c*,*d*) show that irrespective of the diffusivity ratio *Le*, the disturbances emerge either in the monotonic or the short-wave oscillatory-I mode. No long-wave oscillatory instability appears here due to the dampening out of such disturbances by the increased gravitational and surface tension forces. However, it should be noted that at a higher rate of the solute diffusivity (panel

d), regime-1 shrinks drastically, for which the conductive state is more likely to lose its stability into the elasticity dominated short-wave oscillatory-I mode.

Thus, together the panels (*a*-*d*) help in identifying the model parameter spaces that give rise to a particular instability mode once the critical temperature difference across the film is attained. Figure 5.10 is expected to be helpful for carrying out an experimental investigation of the present problem, especially in studying the pattern dynamics of any particular instability mode.

5.6 Potential Experimental Settings

Let us now discuss the conditions at which one may experimentally observe the instability modes detected in this study. This will also shed some light on the differences between the oscillatory-I and oscillatory-II instability characteristics. We begin by considering two different physical systems: *i*) a 0.01 mm thick film of water-ethanol mixture, and *ii*) a 0.1 mm thick film of polystyrene-benzene solution. The physical properties of both the binary mixtures are presented in table 5.1.

Table 5.1: Physical properties of water-ethanol mixture [81,113,114] and polystyrene-benzene solution [115–118].

	water-ethanol mixture (10% w/w)	**polystyrene ($M_w = 20.6\times10^6$ g mol^{-1}) benzene solution** (0.7% w/w)
H (mm)	0.01	0.1
$\mathcal{S}$ (K^{-1})	0.005	0.05
$\hat{\lambda}$ (s)	0	0.12
σ (Nm^{-1})	0.02	0.03
σ_T (N(mK)$^{-1}$)	0.6×10^{-4}	10^{-4}
σ_c (Nm^{-1})	-5.1×10^{-3}	10^{-3}
D (m^{2}s^{-1})	0.85×10^{-9}	2×10^{-10}
α (m^{2}s^{-1})	0.82×10^{-7}	10^{-7}
μ_o (Pa.s)	1.4×10^{-3}	0.187
ρ (kgm^{-3})	800	997

Using the properties from table 5.1 for the water-ethanol system in the terrestrial environment, we obtain

$$(De, \chi, Le, Pr, Ga, \Sigma) \approx (0, -0.4, 0.01, 20, 0.1, 10^3) \tag{7.1}$$

whereas for the polystyrene-benzene solution, we get

$$(De, \chi, Le, Pr, Ga, \Sigma) \approx (1,\ 0.5, 2\times10^{-3}, 1.8\times10^{3}, 0.7,\ 176)\,. \tag{7.2}$$

From Section 4.5 we have learned that the oscillatory-II disturbances emerge only in liquid mixtures with $\chi < 0$ and $Le \gtrsim O(10^{-2})$. The critical parameters (Ma_c, k_c, ω_c) for this instability mode remains unaffected by the elastic behavior of the mixture. On the other hand, the critical parameters for the oscillatory-I mode are weakly influenced by the values of (Le, χ) but governed by the elasticity of the fluid.

It is therefore clear from Eqs. $7.1-7.2$ that the monotonic and oscillatory-II disturbances can emerge only in the water-ethanol mixture. For the parameter values in Eq. 7.1, $Ma_{\text{c,Mon.}} = 1$ and $Ma_{\text{c,osc. II}} = 0.3$ (cf. Fig. 5.8). But since $Ma_{\text{c,osc. II}} < Ma_{\text{c,Mon.}}$, the conductive state for the water-ethanol film first bifurcates into the oscillatory II mode. This bifurcation occurs for a temperature difference $(|\vartheta|H)$ of $0.1\,\text{K}$ across the film. Notably, the oscillatory-I instability sets in this liquid film only when $(|\vartheta|H) > 2\times10^{3}\,\text{K}$, which is at least four order higher than the temperature difference required for the onset of oscillatory-II instability. Hence, only the oscillatory-II mode will likely appear for heating the water-ethanol mixture from the free surface. The characteristics wavelength of the convective structure is estimated to be 1 cm with the oscillation period of $10^4\,\text{s}$.

On the other hand, the parameter values in Eq. 7.2 suggest that the oscillatory-I instability emerges in the polystyrene-benzene solution with $(Ma_c, k_c, \omega_c) \approx (0.18, 3.7, 235)$. For a 0.1 mm thick film, this critical Marangoni number is attained at the temperature difference of $0.4\,\text{K}$ across the film. The corresponding size of the convective pattern is calculated to be 0.03 mm with the oscillation period of $4\times10^{-4}\,\text{s}$.

However, an important remark that needs to be added here is that, for a binary mixture, the parameters $(\mu_o, \lambda, \mathcal{S})$ are a strong function of the concentration of the solution. Therefore, the instability characteristics may vary significantly while dealing

with the same fluid at different concentration.

5.7 Summary

To summarize, the Marangoni instability is detected in a viscoelastic liquid film for heating from the free surface. The system considered here for investigation comprised a thin layer of polymeric solution confined between its deformable free surface and a rigid substrate. Performing a linear stability analysis around the quiescent base state of this system, we have numerically studied the stability characteristics of the system for both the long-wave and short-wave perturbations. A detailed investigation of the stability picture under the confluence of thermosolutocapillarity reveals that the instability modes detected in chapter 4 for the case of heating the film from below, can appear in the system for heating from the free surface as well. However, their characteristics and the parameter domains for which they get dominant in the system vary significantly on changing the direction of heating.

Chapter 6

Conclusions and Scope for Further Work

This chapter highlights the significant achievements of the present thesis. The scope for future work that can be taken up from the knowledge gained from this work is also outlined here for any possible further extension.

6.1 Conclusions

This thesis addresses some of the previously unexplored issues on the Marangoni instability in Newtonian and viscoelastic fluids. Considering the classical system configuration of a liquid film confined between its free surface and a flat rigid substrate, the instability problem is investigated here under the framework of linear stability analysis. Such an analysis helps in predicting the type of bifurcation (pitchfork/saddle-node or hopf bifurcation) and hence the ensuing motion (stationary/oscillatory, long-wave/short-wave). Based on the results of linear stability analysis, we can then carry out a nonlinear stability analysis essentially to study the dynamics of the emerging convective patterns. Compared to a numerical approach, such an analysis can provide a broad insight into the stability picture in a more efficient manner. Had this investigation performed numerically, a large number of numerical experimentations would have required, which proportionately increases the computational cost. The linear stability analysis has proven to be much efficient here. Another issue that may arise during numerical computation is the accuracy level of the employed numerical scheme and the problem of computational instability. While following a numerical approach to study a hydrodynamic instability problem, one must have to distinguish the computational instability from the physical instabilities. However, such issues are not faced in the linear stability analysis technique.

Let us now discuss the major findings of this research work. Considering the broadness of the research domain, which includes investigations on both the Newtonian

and viscoelastic fluids, the concluding remarks are categorized into two subsections. In subsection 6.1.1, we draw the inferences from the investigation on Marangoni instability in a Newtonian liquid film. The conclusions drawn from the analyses on Marangoni instability in the viscoelastic fluid are summarized in subsection 6.1.2.

6.1.1 Effect of non-monotonic variation of surface tension on the Marangoni instability in a Newtonian liquid film

The first part of this thesis aimed to understand the Marangoni instability phenomenon for a Newtonian liquid that presents a maximum of surface tension with temperature. To study the instability characteristics of such a liquid film, the Marangoni number is defined in a slightly different manner from the conventional one, *i.e.*, we define a quadratic Marangoni number in contrast to the linear Marangoni number. It is found that when such a liquid film is heated from below by a poorly thermally conducting substrate, both the monotonic and oscillatory disturbances can emerge as the indication of the onset of convection in the initially quiescent system. A comparison of the expressions for neutral stability curve with that for the case of linear surface tension variation with temperature [54] reveals that while accounting the nonlinear variation of surface tension with temperature, '*Bi*' (Biot number) appears as the correction factor in the expression for neutral stability curve. This suggests that for the Marangoni convection induced by non-monotonic variation of surface tension with temperature, the stability threshold of the system is strongly determined by the magnitude of *Bi* (*i.e.*, the heat transfer rate at the free surface).

This investigation further reveals that, while the monotonic disturbances can appear in the system both in the long-wave and short-wave form, the oscillatory disturbances emerge only in the long-wave form. The oscillatory mode becomes dominant only for small values of the parameters (*Bi*, *Ga*, Σ) *i.e.*, for a poorly conducting (but not insulating) and highly deformable free surface. For a liquid with lower surface tension values, these conditions are often satisfied in the microgravity environment. It should be noted that for $Bi = 0$, the long-wave monotonic mode gets dominant in the system. On the other hand, at higher values of *Bi* (*i.e.*, for a conducting free surface) and (*Ga*, Σ) (*i.e.*, for a non-deformable free surface) the long-wave disturbances get damped, and the short-wave monotonic instability prevails in the system. It is, therefore, apparent that certain

combinations of the parameters set (*Bi*, *Ga*, Σ) can lead to a competition between the monotonic and oscillatory disturbances in the system.

6.1.2 Marangoni instability in viscoelastic liquids

In the second part of this thesis, the instability phenomenon is analyzed for viscoelastic fluids. We first started with the problem of pure thermocapillary driven instability in a viscoelastic liquid film. For this liquid film confined between a deformable free surface and a weakly thermally conducting substrate, linear stability analysis around quiescent base state reveals that both long-wave and short-wave disturbances can emerge in the system. Although the appearance of short-wave disturbances in a viscoelastic liquid film has been previously reported in the literature [71-73], the long-wave instability mode was not detected in these investigations. This is because, in these analyses, the fluid layer was considered to be bounded above by a non-deformable (*i.e.*, (*Ga*, Σ)→∞) and insulating free surface (*i.e.*, *Bi* = 0). However, the long-wave disturbances get dominant in the system only for small (but non-zero) values of the parameter space (*Bi*, *Ga*, Σ), *i.e.*, for a deformable and poorly conducting free surface.

It is important to note that these long-wave and short-wave disturbances can be both monotonic and oscillatory. The elastic behavior of the fluid does not influence the monotonic instability threshold, but significantly affects the onset of oscillatory instability in the system. It is found that the long-wave oscillatory disturbances detected in this work for viscoelastic fluids can also appear in a Newtonian fluid (*i.e.*, for *De* = 0); however, the short-wave oscillatory disturbances emerge only in the viscoelastic fluids (*i.e.*, for *De* > 0). The increasing elasticity of the fluid weakly enhances the stability of the system against the long-wave oscillatory disturbances but makes it more vulnerable towards the short-wave mode.

Therefore, depending on the model parameter values (*Bi*, *De*, *Ga*, Σ), the pure thermocapillary driven instability in a viscoelastic film can appear both in the long-wave and short-wave form. Competition among the various instability modes is also possible in such a liquid film for certain combinations of the model parameters. It is found that the long-wave disturbances get dominant only for a deformable free surface with small values of *Bi* and *De*. These conditions can be physically materialized only for viscoelastic liquids with short relaxation time, when the heat transfer rate at the free surface is low

and gravitational field is weak (*i.e.*, microgravity environment). These long-wave perturbations get damped either with reducing the deformability of the free surface or enhancing the heat transfer rate at the same or with increasing the relaxation time of the liquid (*i.e.*, for higher values of the parameters (*Bi*, *De*, *Ga*, Σ)). Under such circumstances, the instability primarily sets in the short-wave form. Therefore, the present system is expected to be more vulnerable towards the short-wave disturbances at normal terrestrial conditions.

Next, in Chapter 4, this analysis is extended for a polymeric liquid film where the Marangoni instability can occur under the combined influences of thermocapillary and solutocapillary effects. The polymer solutions are essentially the binary mixture of polymeric solute in a Newtonian solvent. In such a liquid film with an externally imposed temperature gradient, the solutocapillary effect often results from thermodiffusion (Soret effect). at the free surface. On investigating the stability behavior under the combined actions of thermo-solutocapillarity, it is found that the complete thermosolutal model demonstrates a stability picture which is rather complex compared to the purely thermocapillary driven instability.

Linear stability analysis around the quiescent base state reveals that apart from the monotonic disturbances, two different oscillatory instabilities, namely oscillatory-I and oscillatory-II, can emerge in this system depending on the physical situations governed by the parameter space (*Bi*, *De*, *Le*, χ, *Ga*, Σ). Similarly to the case of purely thermocapillary driven instability in a viscoelastic liquid film, for the present case also, the monotonic instability threshold remains unaffected by the elastic behavior of the mixture. The solutocapillary force enhances (reduces) the stability of the system against these perturbations for $\chi < 0$ ($\chi > 0$). However, irrespective of the deformability of the free surface or the heat transfer rate from this surface, such disturbances always emerges in the long-wave form. On the other hand, the oscillatory-I instability may appear either in the long-wave or short-wavelength form depending on the deformability of free surface and the elasticity level of the liquid. It is found that while the short-wave oscillatory-I mode is more universal, the long-wave oscillatory-I mode can also get dominant in a weakly viscoelastic film ($De \leq 0.1$) with deformable free surface for $\chi < 0$. The oscillatory-II mode is more case-specific and is likely to emerge in a binary liquid film (irrespective of the elasticity of the mixture) having a deformable free surface at higher

solute diffusivity $Le \geq O(10^{-2})$ and for $\chi > 0$. It is a long-wavelength instability that appears with a significantly large oscillation period compared to the oscillatory-I mode.

From this study, we can thus infer that when a thin polymeric film is subjected to heating from below, the solutocapillary effect plays a crucial role in the emergence of long-wave disturbances. For $\chi > 0$ (or equivalently $\mathcal{S} > 0$) it causes the appearance of long-wave monotonic or oscillatory-II instability (depending on the diffusivity ratio *Le*), whereas for $\chi < 0$, it enhances the stability of the system against the long-wave oscillatory-I perturbations. On the other hand, the thermocapillary effect is primarily responsible for the short-wave oscillatory-I disturbances. The solutocapillarity plays here a minor role. Triggered by the elasticity of the mixture, the short-wave oscillatory-I instability can, therefore, appear for any $\chi \in \mathbb{R}$.

Next, in Chapter 5, we study the instability phenomenon for heating this polymeric film from the free surface. Although the Marangoni instability in a viscoelastic film has already been reported in the literature for heating from below, the instability problem was not studied previously for heating from the free surface. Linear stability analysis reveals that the instability modes detected in Chapter 4 can also appear for heating the system from above. However, there are profound differences between their characteristics, the mechanism behind their origination, and the parameter range for which they get dominant in the system.

For heating the film from above, the monotonic instability emerges only for $\chi < 0$ and is solely caused by the solutocapillary force. The thermocapillarity plays here a stabilizing role. Irrespective of free surface deformability, such disturbances always emerge in the long-wave form ($k_c = 0$). For this particular direction of heating, the onset of oscillatory-I disturbances is a direct manifestation of the elastic behavior of the fluid. Therefore, these disturbances can ideally appear for any $\chi \in \mathbb{R}$. Thermocapillarity, combined with the fluid elasticity primarily gives rise to this instability mode. The solutal effect plays here a secondary role. However, the role of surface deformability is crucial in the emergence of these disturbances in the long-wavelength form, which otherwise appear in the short-wave form for a non-deformable free surface. On the other hand, for heating the fluid layer from above, the oscillatory-II instability occurs only for $\chi < 0$ and

exclusively in a liquid layer with a deformable free surface. For a shorter mass diffusion time scale (*i.e.*, $Le \geq O(10^{-2})$), the competition between the destabilizing solutocapillary and the stabilizing thermocapillary forces give rises to these long-wave disturbances. Compared to the oscillatory-I mode, the oscillatory-II disturbances emerge with much larger sized convective patterns possessing a significantly high oscillation period. Furthermore, while the increasing elasticity of the fluid promotes the onset of oscillatory-I disturbances, the oscillatory-II instability threshold remains essentially unaffected by this rheological behavior of the fluid.

Therefore, it can be inferred that when a thin polymeric liquid film subjected to heating either from above or below, the solutocapillary force often can destabilize the system which otherwise remains stable under the action of thermocapillarity. Importantly, for an externally imposed temperature gradient, the nonuniformities in solute concentration in the present system are solely caused by the Soret effect. This necessitates the consideration of a complete thermosolutal model to study the Marangoni instability in a polymeric film.

6.2 Scope for Further Work

The present thesis attempts to shed light on the Marangoni instability phenomenon in both the Newtonian and viscoelastic fluids. The results obtained here sets up the basic foundation based on which further investigations can be carried to get more insight into this instability phenomenon. Some of the potential areas for future research are mentioned below.

- In the present investigations, various monotonic and oscillatory modes are identified in the system by performing linear stability analysis. The linear theory can effectively predict the critical temperature difference across the film for the onset of convection in the system. However, it does not give any information on the final size and shape of the convection cells. A nonlinear analysis can be carried out for this purpose.

- For each instability mode detected in this work, we have subsequently discussed the feasibility of observing them in a realistic experimental setup. The conditions

for the onset of instability are predicted in greater details for both the Newtonian and viscoelastic fluids. Therefore, attempts can be made to study this instability phenomenon experimentally, which will also verify the present theoretical findings.

- Furthermore, the present analysis can also be extended to some more complex systems. For instance, the instability characteristics of a single fluid layer are investigated in this thesis, wherein the heat flux from the free surface is approximated by Newton's law. However, a more realistic representation of this system is the consideration of a two-layer liquid-gas system. Furthermore, the present investigations can also be extended considering a coupled film-substrate model or incorporating the effect of evaporation at the free surface to study the instability characteristics of a more complex system.

References

[1] P. G. Drazin, W. H. Reid, *Hydrodynamic Stability*, Cambridge University Press, Cambridge, 2004.

[2] S. Chandrasekhar, *Hydrodynamic and Hydromagnetic Stability*, Dover Publications, New York, 1981.

[3] S. J. Weinstein, K. J. Ruschak, Coating Flows, *Annu. Rev. Fluid Mech.* 36 (2004) 29–53.

[4] H. A. Stone, A. D. Stroock, A. Ajdari, Engineering Flows in Small Devices, *Annu. Rev. Fluid Mech.* 36 (2004) 381–411.

[5] T. M. Squires, S. R. Quake, Microfluidics: Fluid physics at the nanoliter scale, *Rev. Mod. Phys.* 77 (2005) 977–1026.

[6] J. C. T. Eijkel, A. van den Berg, Nanofluidics: what is it and what can we expect from it?, *Microfluid. Nanofluidics*. 1 (2005) 249–267.

[7] H. E. Huppert, Gravity currents: a personal perspective, *J. Fluid Mech*. 554 (2006) 299.

[8] J. B. Grotberg, Pulmonary Flow and Transport Phenomena, *Annu. Rev. Fluid Mech.* 26 (1994) 529–571.

[9] W. Shyy and, M. Francois, H. Udaykumar, N. N'dri and, R. Tran-Son-Tay, Moving boundaries in micro-scale biofluid dynamics, *Appl. Mech. Rev*. 54 (2001) 405–454.

[10] H. Bénard, Les tourbillons cellulaires dans une nappe de liquide transportant de la chaleur par convection en régime permanent, *Ann. Chem. Phys*. 23 (1901) 62–144.

[11] J. R. A. Pearson, On convection cells induced by surface tension, *J. Fluid Mech*. 4 (1958) 489–500.

[12] P. Colinet, J. C. Legros, M. G. Velarde, *Nonlinear Dynamics of Surface-Tension-Driven Instabilities*, Berlin, 2001.

[13] J. R. L. Skarda, D. Jacqmin, F.E. McCaughan, Exact and approximate solutions to the double-diffusive Marangoni–Bénard problem with cross-diffusive terms, *J. Fluid Mech.* 366 (1998) 109–133.

[14] J. L. Castillo, M. G. Velarde, Thermal diffusion and the Marangoni-Bénard instability of a two-component fluid layer heated from below, *Phys. Lett. A*. 66 (1978) 489–491.

[15] C. L. McTaggart, Convection driven by concentration- and temperature-dependent surface tension, *J. Fluid Mech.* 134 (1983) 301–310.

[16] J. Castillo, M. Velarde, Marangoni convection in liquid films with a deformable open surface, *J. Colloid Interface Sci.* 108 (1985) 264–270.

[17] C. F. Chen, T. F. Su, Effect of surface tension on the onset of convection in a double- diffusive layer, *Phys. Fluids A* 4 (1992) 2360–2367.

[18] J. K. Bhattacharjee, Marangoni convection in binary liquids, *Phys. Rev. E*. 50 (1994) 1198–1205.

[19] A. Bergeon, D. Henry, H. Benhadid, Marangoni-Bénard instability in microgravity conditions with Soret effect, *Int. J. Heat Mass Transf.* 37 (1994) 1545-1562.

[20] A. Bergeon, D. Henry, H. Benhadid, L. S. Tuckerman, Marangoni convection in binary mixtures with Soret effect, *J. Fluid Mech.* 375 (1998) 143–177.

[21] I. Fayzrakhmanova,. S. Shklyaev, A. Nepomnyashchy, Influence of a low frequency vibration on a long-wave Marangoni instability in a binary mixture with the Soret effect, *Phys. Fluids*. 22 (2010) 104101.

[22] I. Fayzrakhmanova, S. Shklyaev, A. Nepomnyashchy, Influence of low-frequency vibration on thermocapillary instability in a binary mixture with the Soret effect: long-wave versus short-wave perturbations, *J. Fluid Mech*. 714 (2013) 190–212.

[23] H. Kawamura, K. Nishino, S. Matsumoto, I. Ueno, Report on Microgravity Experiments of Marangoni Convection Aboard International Space Station, *J. Heat Transfer*. 134 (2012) 031005.

[24] L. G. Napolitano, Materials: Marangoni Convection in Space Microgravity Environments, *Science* 225 (1984) 197–198.

[25] C. H. Chun, Wuest, A micro-gravity simulation of the Marangoni convection, *Acta Astronaut.* 5 (1978) 681–686.

[26] D. Schwabe, The Bénard-Marangoni-Instability in small circular containers under microgravity: Experimental results, *Adv. Sp. Res*. 24 (1999) 1347–1356.

[27] F. J. Zuiderweg, A. Harmens, The influence of surface phenomena on the performance of distillation columns, *Chem. Eng. Sci*. 9 (1958) 89-103.

[28] J. C. Berg, C. R. Morig, Density effects in interfacial convection, *Chem. Eng. Sci*. 24 (1969) 937–946.

[29] J. C. Berg, G. S. Haselberger, Mass transfer during interfacial convection, *Chem. Eng. Sci.* 26 (1971) 481–485.

[30] J. Berg, Interfacial Hydrodynamics: An Over View, *Can. Metall. Q*. 21 (1982) 121–136.

[31] P. L. T. Brian, J. E. Vivian, S. T. Mayr, Cellular Convection in Desorbing Surface Tension-Lowering Solutes from Water, Ind. Eng. Chem. Fundam. 10 (1971) 75–83.

[32] M. A. Mendes-Tatsis, E. S. Perez de Ortiz, Spontaneous interfacial convection in liquid–liquid binary systems under microgravity, *Proc. R. Soc. London. Ser. A Math. Phys. Sci.* 438 (1992) 389–396.

[33] E. Susana Pérez de Ortiz, H. Sawistowski, Interfacial stability of binary liquid—liquid systems—I. Stability analysis, *Chem. Eng. Sci.* 28 (1973) 2051–2061.

[34] L. M. Rabinovich, *Mathematical modelling of chemical process*, CRC Press, Boca Raton, 1992.

[35] J. C. Berg, M. Boudart, A. Acrivos, Natural convection in pools of evaporating liquids, *J. Fluid Mech*. 24 (1966) 721.

[36] J. C. Berg, A. Acrivos, M. Boudart, *Evaporative Convection*, (1966) 61–123.

[37] T. J. Boggon, N. E. Chayen, E. H. Snell, J. Dong, P. Lautenschlager, L. Potthast, D. P. Siddons, V. Stojanoff, E. Gordon, A. W. Thompson, P. F. Zagalsky, R. Bi, J. R. Helliwell, Protein crystal movements and fluid flows during microgravity growth, *Philos. Trans. R. Soc. London. Ser. A Math. Phys. Eng. Sci*. 356 (1998) 1045–1061.

[38] A. Kumar, S. Roy, Effect of three-dimensional melt pool convection on process characteristics during laser cladding, *Comput. Mater. Sci.* 46 (2009) 495–506.

[39] K. C. Mills, B. J. Keene, R. F. Brooks, A. Shirali, Marangoni effects in welding, *Philos. Trans. R. Soc. London. Ser. A Math. Phys. Eng. Sci.* 356 (1998) 911–925.

[40] T. A. Arshad, C. Bin Kim, N. A. Prisco, J. M. Katzenstein, D. W. Janes, R. T. Bonnecaze, C. J. Ellison, Precision Marangoni-driven patterning, *Soft Matter*. 10 (2014) 8043–8050.

[41] S. G. Yiantsios, B. G. Higgins, Marangoni flows during drying of colloidal films, *Phys. Fluids*. 18 (2006) 082103.

[42] C. Marangoni, Ueber die Ausbreitung der Tropfen einer Flüssigkeit auf der Oberfläche einer anderen, *Ann. Phys.* 22 (1871) 337–354.

[43] D. C. Venerus, D. Nieto Simavilla, Tears of wine: new insights on an old phenomenon, *Sci. Rep.* 5 (2015) 16162.

[44] M. J. Block, Surface Tension as the Cause of Bénard Cells and Surface Deformation in a Liquid Film, *Nature*. 178 (1956) 650–651.

[45] M. F. Schatz, G. P. Neitzel, Experiments on Thermocapillary Instabilities, *Annu. Rev. Fluid Mech*. 33 (2001) 93–127.

[46] S. Davis, Thermocapillary Instabilities, *Annu. Rev. Fluid Mech.* 19 (1987) 403–435.

[47] A. Oron, S. H. Davis, S. G. Bankoff, Long-scale evolution of thin liquid films, *Rev. Mod. Phys*. 69 (1997) 931–980.

[48] S. Shklyaev, A. Nepomnyashchy, *Longwave Instabilities and Patterns in Fluids*, Springer New York, 2017.

[49] A. A. Nepomnyashchy, *Interfacial Phenomena and Convection*, Chapman and Hall/CRC, 2001.

[50] L. E. Scriven, C. V. Sternling, On cellular convection driven by surface-tension gradients: effects of mean surface tension and surface viscosity, *J. Fluid Mech*. 19

(1964) 321–340.

[51] S. J. Vanhook, M. F. Schatz, J. B. Swift, W. D. McCormick, H. L. Swinney, Long-wavelength surface-tension-driven Benard convection: experiment and theory, *J. Fluid Mech.* 345 (1997) 45–78.

[52] M. Takashima, Surface Tension Driven Instability in a Horizontal Liquid Layer with a Deformable Free Surface. II. Overstability, *J. Phys. Soc. Japan*. 50 (1981) 2751–2756.

[53] M. Takashima, Surface Tension Driven Instability in a Horizontal Liquid Layer with a Deformable Free Surface. I. Stationary Convection, *J. Phys. Soc. Japan.* 50 (1981) 2745–2750.

[54] S. Shklyaev, M. Khenner, A. A. Alabuzhev, Oscillatory and monotonic modes of long-wave Marangoni convection in a thin film, *Phys. Rev. E.* 82 (2010) 025302.

[55] S. Shklyaev, A. A. Alabuzhev, M. Khenner, Long-wave Marangoni convection in a thin film heated from below, *Phys. Rev. E.* 85 (2012) 016328.

[56] A. E. Samoilova, N. I. Lobov, On the oscillatory Marangoni instability in a thin film heated from below, Phys. Fluids. 26 (2014) 064101.

[57] A. Cloot, G. Lebon, Marangoni convection induced by a nonlinear temperature-dependent surface tension, *J. Phys.* 47 (1986) 23–29.

[58] J. C. Legros, Problems related to non-linear variations of surface tension, *Acta Astronaut*. 13 (1986) 697–703.

[59] D. Villers, J. K. Platten, Temperature dependence of the interfacial tension between water and long-chain alcohols, *J. Phys. Chem*. 92 (1988) 4023–4024.

[60] Y. Abe, Self-rewetting fluids, *Ann. N. Y. Acad. Sci.* 1077 (2006) 650–667.

[61] A. Oron, P. Rosenau, On a nonlinear thermocapillary effect in thin liquid layers, *J. Fluid Mech.* 273 (1994) 361.

[62] R. B. Bird, R. C. Armstrong, O. Hassager, *Dynamics of polymeric liquids.* Vol. 1, : Fluid mechanics, 1987.

[63] J. C. Maxwell, On the dynamical theory of gases, *Philos. Trans. R. Soc. London*. 157 (1867) 49–88.

[64] H. Jeffreys, *The Earth*, Cambridge University Press, 1929.

[65] J. G. Oldroyd, On the Formulation of Rheological Equations of State, *Proc. R. Soc. A Math. Phys. Eng. Sci.* 200 (1950) 523–541.

[66] N. P. Thien, R. I. Tanner, A new constitutive equation derived from network theory, *J. Nonnewton. Fluid Mech.* 2 (1977) 353–365.

[67] G. Toussaint, H. Bodiguel, F. Doumenc, B. Guerrier, C. Allain, Experimental characterization of buoyancy- and surface tension-driven convection during the drying of a polymer solution, *Int. J. Heat Mass Transf*. 51 (2008) 4228–4237.

[68] N. Bassou, Y. Rharbi, Role of Bénard-Marangoni instabilities during solvent evaporation in polymer surface corrugations, *Langmuir* 25 (2009) 624-632.

[69] E. Bormashenko, S. Balter, R. Pogreb, Y. Bormashenko, O. Gendelman, D. Aurbach, On the mechanism of patterning in rapidly evaporated polymer solutions: Is temperature-gradient-driven Marangoni instability responsible for the large-scale patterning?, *J. Colloid Interface Sci*. 343 (2010) 602–607.

[70] S. Y. Heriot, R. A. L. Jones, An interfacial instability in a transient wetting layer leads to lateral phase separation in thin spin-cast polymer-blend films, *Nat. Mater*. 4 (2005) 782–786.

[71] D. Getachew, S. Rosenblat, Thermocapillary instability of a viscoelastic liquid layer, *Acta Mech*. 55 (1985) 137–149.

[72] G. Lebon, P. Parmentier, O. Teller, P. C. Dauby, Bénard-Marangoni instability in a viscoelastic Jeffreys' fluid layer, *Rheol. Acta*. 33 (1994) 257–266.

[73] P. Parmentier, G. Lebon, V. Regnier, Weakly nonlinear analysis of Bénard–Marangoni instability in viscoelastic fluids, *J. Nonnewton. Fluid Mech.* 89 (2000) 63–95.

[74] H. Ramkissoon, G. Ramdath, D. Comissiong, K. Rahaman, On thermal instabilities in a viscoelastic fluid, Int. J. Non. Linear. Mech. 41 (2006) 18–25.

[75] D. D. Joseph, *Fluid Dynamics of Viscoelastic Liquids*, Springer, New York, 1990.

[76] S. Wiegand, Thermal diffusion in liquid mixtures and polymer solutions, *J. Phys. Condens. Matter* 16 (2004) R357–R379.

[77] M. Zhang, F. Müller-Plathe, The Soret effect in dilute polymer solutions: Influence of chain length, chain stiffness, and solvent quality, *J. Chem. Phys*. 125 (2006) 124903.

[78] A. Würger, Thermophoresis in Colloidal Suspensions Driven by Marangoni Forces, *Phys. Rev. Lett*. 98 (2007) 138301.

[79] K. J. Zhang, M. E. Briggs, R. W. Gammon, J. V. Sengers, J. F. Douglas, Thermal and mass diffusion in a semidilute good solvent-polymer solution, *J. Chem. Phys* 111 (1999) 2270–2282.

[80] R. Kita, S. Wiegand, J. Luettmer-Strathmann, Sign change of the Soret coefficient of poly(ethylene oxide) in water/ethanol mixtures observed by thermal diffusion forced Rayleigh scattering, *J. Chem. Phys*. 121 (2004) 3874–3885.

[81] R. Kita, G. Kircher, S. Wiegand, Thermally induced sign change of Soret coefficient for dilute and semidilute solutions of poly(N-isopropylacrylamide) in ethanol, *J. Chem. Phys*. 121 (2004) 9140–9146.

[82] J. Rauch, W. Köhler, Collective and thermal diffusion in dilute, semidilute, and concentrated solutions of polystyrene in toluene, *J. Chem. Phys.* 119 (2003) 11977–11988.

[83] S. G. Yiantsios, S. K. Serpetsi, F. Doumenc, B. Guerrier, Surface deformation and film corrugation during drying of polymer solutions induced by Marangoni phenomena, *Int. J. Heat Mass Transf.* 89 (2015) 1083–1094.

[84] F. Doumenc, E. Chénier, B. Trouette, T. Boeck, C. Delcarte, B. Guerrier, M. Rossi,

Free convection in drying binary mixtures: Solutal versus thermal instabilities, *Int. J. Heat Mass Transf.* 63 (2013) 336–350.

[85] K. A. Smith, On convective instability induced by surface-tension gradients, *J. Fluid Mech.* 24 (1966) 401.

[86] H. J. Palmer, J. C. Berg, Convective instability in liquid pools heated from below, *J. Fluid Mech.* 47 (1971) 779.

[87] K. Eckert, M. Bestehorn, A. Thess, Square cells in surface-tension-driven Bénard convection: Experiment and theory, *J. Fluid Mech.* 356 (1998) 155-197.

[88] M. C. Benguria, R. D. Depassier, On the linear stability theory of Bénard–Marangoni convection, *Phys. Fluids A* 1 (1989) 1123–1127.

[89] A. Oron, P. Rosenau, Evolution of the coupled Bénard-Marangoni convection, *Phys. Rev. A* 39 (1989) 2063–2069.

[90] C. Pérez- García, G. Carneiro, Linear stability analysis of Bénard–Marangoni convection in fluids with a deformable free surface, *Phys. Fluids A* 3 (1991) 292–298.

[91] P. Colinet, J. C. Legros, Y. Kamotani, P. C. Dauby, G. Lebon, Finite-amplitude regimes of the short-wave Marangoni-Benard convective instability, *Phys. Rev. E* 52 (1995) 2603–2616.

[92] L. Y. Yeo, R. V. Craster, O. K. Matar, Marangoni instability of a thin liquid film resting on a locally heated horizontal wall, *Phys. Rev. E* 67 (2003) 056315.

[93] M. Celli, A. Barletta, L. S. de B. Alves, Marangoni instability of a liquid film flow with viscous dissipation, *Phys. Rev. E* 91 (2015) 023006.

[94] F. Doumenc, T. Boeck, B. Guerrier, M. Rossi, Transient Rayleigh–Bénard–Marangoni convection due to evaporation: a linear non-normal stability analysis, *J. Fluid Mech.* 648 (2010) 521.

[95] C. Ruyer-Quil, B. Scheid, S. Kalliadasis, M.G. Velarde, Thermocapillary long waves in a liquid film flow. Part 1. Low-dimensional formulation, *J. Fluid Mech*. 538 (2005) 199.

[96] H. Zhou, Y. Zhu, T. Peng, Y. Song, J. An, X. Leng, Z. Yi, Y. Sun, H. Jia, Systematic study of the effects of novel halogen-free anionic surface active ionic liquid on interfacial tension of water/model oil system, *J. Mol. Liq.* 223 (2016) 516–520.

[97] S. Enders, H. Kahl, Interfacial properties of water + alcohol mixtures, *Fluid Phase Equilib.* 263 (2008) 160–167.

[98] M. Morozov, A. Oron, A. A. Nepomnyashchy, Long-wave Marangoni convection in a layer of surfactant solution, *Phys. Fluids.* 26 (2014) 112101.

[99] S. Shklyaev, A. A. Nepomnyashchy, Longwave Marangoni convection in a surfactant solution between poorly conducting boundaries, *J. Fluid Mech*. 718 (2013) 428–456.

[100] A. Podolny, A. Oron, A. A. Nepomnyashchy, Linear and nonlinear theory of long-

wave Marangoni instability with the Soret effect at finite Biot numbers, *Phys. Fluids*. 18 (2006) 054104.

[101] A. Podolny, A. A. Nepomnyashchy, A. Oron, Long-wave Marangoni instability in a binary liquid layer on a thick solid substrate, *Phys. Rev. E - Stat. Nonlinear, Soft Matter Phys.* 76 (2007) 026309.

[102] P. L. G. Ybarra, J. L. Castillo, M. G. Velarde, Benard--Marangoni convection with a deformable interface and poorly conducting boundaries, *Phys. Fluids.* 30 (1987) 2655–2661.

[103] A. Oron, A. A. Nepomnyashchy, Long-wavelength thermocapillary instability with the Soret effect, *Phys. Rev. E* 69 (2004) 016313.

[104] A. Podolny, A. Oron, A. A. Nepomnyashchy, Long-wave Marangoni instability in a binary-liquid layer with deformable interface in the presence of Soret effect: Linear theory, *Phys. Fluids*. 17 (2005) 104104.

[105] R. V. Craster, O. K. Matar, Dynamics and stability of thin liquid films, *Rev. Mod. Phys*. 81 (2009) 1131–1198.

[106] P. C. Dauby, P. Parmentier, G. Lebon, M. Grmela, Coupled buoyancy and thermocapillary convection in a viscoelastic Maxwell fluid, *J. Phys. Condens. Matter*. 5 (1993) 4343–4352.

[107] S. Saprykin, R. J. Koopmans, S. Kalliadasis, Free-surface thin-film flows over topography: influence of inertia and viscoelasticity, *J. Fluid Mech*. 578 (2007) 271.

[108] H. B. Keller, *Numerical Methods for Two-Point Boundary-Value Problems*, Dover Publications, New York, 2018.

[109] S. R. De Groot, P. Mazur, *Non-equilibrium thermodynamics*, Dover Publications, New York, 2011.

[110] S. Shklyaev, A. A. Nepomnyashchy, A. Oron, Marangoni convection in a binary liquid layer with Soret effect at small Lewis number: Linear stability analysis, *Phys. Fluids.* 21 (2009) 054101.

[111] M. Bestehorn, I. D. Borcia, Thin film lubrication dynamics of a binary mixture: Example of an oscillatory instability, *Phys. Fluids*. 22 (2010) 104102.

[112] S. W. Joo, Marangoni instabilities in liquid mixtures with Soret effects, *J. Fluid Mech*. 293 (1995) 127–145.

[113] I. S. Khattab, F. Bandarkar, M. A. A. Fakhree, A. Jouyban, Density, viscosity, and surface tension of water+ethanol mixtures from 293 to 323K, *Korean J. Chem. Eng*. 29 (2012) 812–817.

[114] J. Wang, M. Fiebig, Measurement of the thermal diffusivity of aqueous solutions of alcohols by a laser-induced thermal grating technique, *Int. J. Thermophys*. 16 (1995) 1353–1361.

[115] M. Adam, M. Delsanti, Viscosity and longest relaxation time of semi-dilute polymer solutions. I. Good solvent, *J. Phys.* 44 (1983) 1185–1193.

[116] M. Hartung, J. Rauch, W. Köhler, Thermal diffusion of dilute polymer solutions:

The role of solvent viscosity, *J. Chem. Phys*. 125 (2006) 214904.

[117] J. E. Mark, Polymer Data Handbook, Oxford University Press, New York. 2009 .

[118] M. Singh, Survismeter unit for surface tension, viscosity, and dipole moment determination for polystyrene interactions in benzene, *J. Dispers. Sci. Technol.* 28 (2007) 1278-1286.

Appendix A

Expressions for the terms $\aleph_0 - \aleph_8$ ***appearing in Eq.*** **2.41**

$$\aleph_0 = \gamma_1/\gamma_2 \tag{A.1}$$

$$\gamma_1 = -\lambda Pr\, k_1^3 \cosh k_1 - 2\lambda Pr\, k_1 k^2 \cosh k + 3\lambda Pr\, k_1 k^2 \cosh k_1 + \lambda^2 k_1 \cosh k - \lambda^2 k_1 \cosh k_1 + Pr\left(Ga + Ca k^2\right)\left(k k_1 \sinh k - k^2 \sinh k_1\right)$$

$$\gamma_2 = 2\lambda Pr\, k^3 \sinh k + \lambda Pr\, k_1^3 \sinh k_1 - 3\lambda Pr\, k_1 k^2 \sinh k_1 - \lambda^2 k \sinh k + \lambda^2 k_1 \sinh k_1 - Pr\, k^2 \left(Ga + Ca\, k^2\right)\left(\cosh k - \cosh k_1\right)$$

$$k_1 = \sqrt{k^2 - \lambda/Pr}$$

$$k_2 = \sqrt{k^2 - \lambda}$$

$$\aleph_1 = \lambda k_2 \sinh k_2 + \lambda Bi \cosh k_2 \tag{A.2}$$

$$\aleph_2 = -k\, k_1 \exp\left(-k_2\right) + \lambda k \exp\left(-k_2\right)/2k_1 + k\, k_1 Bi \exp\left(-k_2\right)/k_2 - \lambda Bi\, k \exp\left(-k_2\right)/2k_1 k_2 + k\, k_1 \cosh k - \lambda k \sinh k_1/2 - \lambda k \cosh k_1/2k_1 + k\, Bi \sinh k_1 - \lambda Bi\, k \cosh k_1/2k_1 \tag{A.3}$$

$$\aleph_3 = -\lambda Bi\, k \sinh k_1/2k_1 - \lambda\, k \cosh k_1/2 - \lambda\, k \sinh k_1/2k_1 + k^2 \sinh k + kBi \sinh k_1 \tag{A.4}$$

$$\aleph_4 = -2Bi\lambda k\, k_1 \sinh k + Bi\lambda k_1^2 \sinh k_1 + Bi\lambda k^2 \sinh k_1 \tag{A.5}$$

$$\aleph_5 = -2Bi\lambda k^2 \cosh k + Bi\lambda k_1^2 \cosh k_1 + Bi\lambda k^2 \cosh k_1 \tag{A.6}$$

$$\aleph_6 = -k^2 k_1 \exp\left(-k_2\right)/k_2 + \lambda k^2 \exp\left(-k_2\right)/2k_1 k_2 + \lambda k^2 \cosh k_1/2k_1 - k^2 \sinh k_1 \tag{A.7}$$

$$\aleph_7 = \lambda k^2 \sinh k_1/2k_1 - k^2 \cosh k_1 \tag{A.8}$$

$$\aleph_8 = \lambda k \cosh k_2 \tag{A.9}$$

Appendix B

Determination of $Ma_{osc.}$, $k_{c,o}$ and $\omega_{c,o}$ for the long-wave oscillatory instability mode

For the long-wave oscillatory mode, the expression governing the stability threshold of the liquid layer is given by Eq. 3.37. Now, to obtain $k_{c,o}$, we differentiate Eq. 3.37 with respect to *k* and set the final result equal to zero. This gives

$$\alpha_1 k^8 + \alpha_2 k^6 + \alpha_3 k^4 + \alpha_4 k^2 + \alpha_5 = 0 \tag{B.1}$$

where

$$\alpha_1 = 108\Sigma De^2 - 3De\Sigma^2 - Bi\Sigma^2 De^2 \tag{B.2}$$

$$\alpha_2 = 42\Sigma De + 72GaDe^2 - 2Ga\Sigma De - 2Ga\Sigma BiDe^2 \tag{B.3}$$

$$\alpha_3 = 24\Sigma - 15\mathrm{Ga}\,\mathrm{De} + 15\Sigma BiDe - 108De - 36GaBiDe^2 - BiGa^2De^2 - DeGa^2 \tag{B.4}$$

$$\alpha_4 = -216BiDe - 6BiGaDe \tag{B.5}$$

$$\alpha_5 = -72Bi \tag{B.6}$$

Solving Eq. B.1 for a particular set of *Bi*, *De*, *Ga* and Σ; we get at least one real *k* within the permissible limit which turns out to be the $k_{c,osc.}$ for the long-wave oscillatory mode. Substitution of this $k_{c,osc.}$ into Eqs. 3.37 and 3.38 yields the corresponding $Ma_{c,osc.}$ and $\omega_{c,osc.}$ for this instability mode.

Appendix C

C.1 *Expressions for the coefficients used in Eq.* 4.39

$$\mathcal{N}_0 = 2\mathcal{B}\mathcal{Q}q^4 + 2\mathcal{Q}q^6, \tag{C.1}$$

$$\mathcal{N}_1 = -2\mathcal{B}\left(3+\mathcal{Q}Le^{-1}\right)q^2 - 2\left[3+\mathcal{Q}\left(1+Le^{-1}+\mathcal{B}\mathcal{D}e\right)\right]q^4 - 2\mathcal{D}e\,\mathcal{Q}q^6, \tag{C.2}$$

$$\mathcal{N}_2 = 6\mathcal{B}Le^{-1} + 2\left[\left(3+\mathcal{Q}+\mathcal{B}\mathcal{D}e\mathcal{Q}\right)Le^{-1}+3\right]q^2 + 2\mathcal{D}e\,\mathcal{Q}\left(1+Le^{-1}\right)q^4, \tag{C.3}$$

$$\mathcal{N}_3 = -6Le^{-1} - 2\mathcal{D}e\,\mathcal{Q}Le^{-1}q^2; \tag{C.4}$$

$$\mathcal{D}_0 = \mathcal{B}\mathcal{Q}\chi Le^{-1}q^2 + \left[\left(1+\chi\right)\left(72+\mathcal{Q}\right)+\mathcal{Q}\chi Le^{-1}\right]q^4, \tag{C.5}$$

$$\mathcal{D}_1 = -\left[\left(1+\chi\right)\left(48+\mathcal{Q}Le^{-1}\right)+2\left(36+24\chi+\mathcal{D}e\chi\mathcal{Q}\right)Le^{-1}\right]q^2 - 2\mathcal{D}e\left[\mathcal{Q}\chi Le^{-1}+\left(1+\chi\right)\left(36+\mathcal{Q}\right)\right]q^4 - 48\mathcal{B}\chi Le^{-1}, \tag{C.6}$$

$$\mathcal{D}_2 = 48\left(1+\chi+\mathcal{B}\mathcal{D}e\chi\right)Le^{-1} + \mathcal{D}e^2\mathcal{Q}\left(1+\chi+\chi Le^{-1}\right)q^4 + \mathcal{D}e\left[2\left(1+\chi\right)\left(24+\mathcal{Q}Le^{-1}\right)+\left(72+48\chi+\mathcal{B}\mathcal{D}e\chi\mathcal{Q}\right)Le^{-1}\right]q^2, \tag{C.7}$$

$$\mathcal{D}_3 = -\mathcal{D}e\left(1+\chi\right)\left(48+\mathcal{D}e\,\mathcal{Q}q^2\right)Le^{-1}. \tag{C.8}$$

C.2 *Expressions for the coefficients utilized in Eq.* 4.45

$$\gamma_0 = \Sigma\left(Le+\chi+Le\chi\right), \tag{C.9}$$

$$\gamma_1 = \chi\left(Ga+Bi\Sigma\right)+Le\left(1+\chi\right)\left(72+Ga\right), \tag{C.10}$$

$$\gamma_2 = BiGa\chi. \tag{C.11}$$

C.3 *Expressions for the coefficients used in Eq.* 4.47

$$\mathcal{L}_0 = DeLe\left(Le+\chi+Le\chi\right), \tag{C.12}$$

$$\mathcal{L}_1 = Le^2\left(1+\chi\right)\left(BiDe-1\right)+2BiDeLe\chi-\chi\left(1+Le\right), \tag{C.13}$$

$$\mathcal{L}_2 = Bi\chi\left(BiDeLe-Le-2\right), \tag{C.14}$$

$$\mathcal{L}_3 = -Bi^2\chi, \tag{C.15}$$

$$\mathcal{L}_4 = -De, \tag{C.16}$$

$$\mathcal{L}_5 = 1+\chi-BiDe. \tag{C.17}$$

List of Publications

From this thesis work

[1] **R. Sarma** and P. K. Mondal, Marangoni instability in a thin film heated from below: Effect of nonmonotonic dependence of surface tension on temperature, *Phys. Rev. E*. 97 (2018) 043105.

[2] **R. Sarma** and P. K. Mondal, Marangoni instability in a heated viscoelastic liquid film: Long-wave versus short-wave perturbations, *Phys. Rev. E.* 100 (2019) 013103.

[3] **R. Sarma** and P. K. Mondal, Marangoni instability in a viscoelastic binary film with cross-diffusive effect, *J. Fluid Mech*. 910 (2021) A30.

[4] **R. Sarma** and P. K. Mondal, Thermosolutal Marangoni instability in a viscoelastic liquid film: effect of heating from the free surface, *J. Fluid Mech*. 909 (2020) A12.

Outside this thesis

[1] **R. Sarma**, H. Gaikwad and P. K. Mondal, Effect of conjugate heat transfer on entropy generation in slip-driven microflow of power law fluids, *Nanoscale Microscale Thermophys. Eng*. 21 (2017) 26–44.

[2] **R. Sarma**, M. Jain and P. K. Mondal, Towards the minimization of thermodynamic irreversibility in an electrically actuated microflow of a viscoelastic fluid under electrical double layer phenomenon, *Phys. Fluids*. 29 (2017) 103102.

[3] **R. Sarma** and P. K. Mondal, Entropy generation minimization in a pressure-driven microflow of viscoelastic fluid with slippage at the wall: Effect of conjugate heat transfer, *J. Heat Transfer*. 140 (2018) 052402.

[4] **R. Sarma**, A. J. Nath, T. Konwar, P. K. Mondal and S. Wongwises, Thermo-hydrodynamics of a viscoelastic fluid under asymmetrical heating, *Int. J. Heat Mass Transf*. 125 (2018) 515–524.

[5] **R. Sarma**, N. Deka, K. Sarma and P. K. Mondal, Electroosmotic flow of Phan-Thien–Tanner fluids at high zeta potentials: An exact analytical solution, *Phys. Fluids*. 30 (2018) 062001.

[6] H. S. Gaikwad, P. Baghel, **R. Sarma** and P. K. Mondal, Transport of neutral solutes in a viscoelastic solvent through a porous microchannel, *Phys. Fluids*. 31 (2019) 022006.

[7] **R. Sarma**, A. Shukla, H. S. Gaikwad, P. K. Mondal and S. Wongwises Effect of conjugate heat transfer on the thermo-electro-hydrodynamics of nanofluids: entropy optimization analysis, *J. Therm. Anal. Calorim*. (Accepted for publication, DOI: 10.1007/s10973-020-10341-6).